Ballon pathfinders for ultra-high energy cosmic ray detection from space : optics performance and search for air showers

Abraham Neftali Diaz Damian

THÈSE

En vue de l'obtention du

DOCTORAT DE L'UNIVERSITÉ DE TOULOUSE

Délivré par : *l'Université Toulouse 3 Paul Sabatier (UT3 Paul Sabatier)*

Présentée et soutenue le *14/01/2020* **par :**

ABRAHAM NEFTALI DIAZ DAMIAN

Démonstrateurs Ballon pour la Détection de Rayons Cosmiques d'Ultra Haute Énergie depuis l'Espace: Performance Optique et Recherche de Gerbes Atmosphériques

---

JURY

MARIO E. BERTAINA	Professeur d'Université	Rapporteur
JEAN EVRARD	Ingenieur CNES	Examinateur
PIERRE JEAN	Professeur d'Université	Président du Jury
ISABELLE LHENRY-YVON	Professeure d'Université	Rapportrice
NICOLAS SORDELLO	Ingenieur Mecano I&D	Examinateur
PETER VON BALLMOOS	Proffeseur d'Université	Directeur de thèse

---

École doctorale et spécialité :
SDU2E : Astrophysique, Sciences de l'Espace, Planétologie
Unité de Recherche :
Institut de Recherche en Astrophysique et Planetologie (UMR 5277)
Directeur de Thèse :
Peter VON BALLMOOS
Rapporteurs :
Mario E. BERTAINA et *Isabelle LHENRY-YVON*

Acknowledgements

This three year adventure wouldn't have been possible without the contribution of many people and institutions who helped me to make this dream a reality. I would like to express my great appreciation for everyone who accompanied and supported my PhD.

First of all I would like to thank CNES and Mecano I&D. Without their funding none of this work would have been possible. From CNES I would like to thank Olivier la Marle and Philippe Laudet for keeping track of my work as well as Jean Evrard for his collaboration with our project. I would like to thank the Mecano I&D society for co-funding this PhD research grant and more specifically Nicolas Sordello and Didier Zely for keeping track of my work during these 3 years.

I want to thank Peter who was been not only a great advisor but also a good friend and has given me a lot of support before, during and probably after my PhD. I hope this friendship can continue for a long time and that we can keep drinking those coronas while having a nice chat. I would like to thank my thesis committee: Natalie, Jean-François and Gustavo as well as the director of my doctoral school Genevieve. Their follow-up of my project and positive feedback was a great motivation to continue this work at difficult moments.

I would like to thank all the JEM-EUSO members who helped me in some way or just shared a nice time during the incredible missions all over the world. Lawrence and Johannes for their warm welcome in Golden, for letting us to work with them on the SPB1 optics and those fun afterworks. Etienne, Guillaume and Jörg for helping me understand better our detector and for those amazing barbecues in New Zealand. Lech for his support in helping me understand the EUSO data. Takky and Naoto for helping me to understand better the Fresnel optics of our Telescopes. Mario, Kenji and Šimon for taking care of the analysis meetings and the balloon sessions. Matteo for that awesome Kobe beef, Francesca for presenting my poster in ICRC2019 and Michal for the simulated EUSO-SPB1 data. I also express my gratitude to all the people who organized the collaboration meetings and those incredible dinners.

I would like to thank all the people who made my stay in IRAP a very pleasant one. Tiziana for her support, comprehension and advice. My friends from the normal and Mediterranean front: Alessio, Andres, Gabi, Sacha, Sid and Sujay for all those fun evenings, dinners, picnics, hikes and many more things. The crazy generation of J014: Mathias, Paul and Edo for the fun office environment and the interns who directly helped with this work: Bakhao, Baptiste and Heeral.

Lastly, I would like to thank my family. My mother for her unconditional support, motivation which kept me strong during difficult times. Without her this dream wouldn't have become a reality. My little sister Odette for her calls and visiting me twice in Toulouse and my grandmother for her love and motivation.

Abstract

Ultra High Energy Cosmic Rays (UHECR) are charged particles coming from outer space with energies $>10^{18}$ eV up to a record measured energy of 3×10^{20} eV. They are the most energetic cosmic messengers coming to earth, however their origin and acceleration mechanisms remain a mystery. Their observation is characterized by their low flux (one particle per steradian per km^2 per century) requiring indirect detection techniques using the atmosphere as a calorimeter. The JEM-EUSO framework aims at developing a space-borne telescope to observe the UHECR induced atmospheric particle cascades (air showers) through their UV fluorescence emission (300 - 400 nm). To validate JEM-EUSO's technology and methods, two balloon-borne pathfinders have been developed: EUSO-Balloon and EUSO-SPB1, they were flown in 2014 and 2017 respectively.

One of the key technologies of these pathfinders is their refractive optical system consisting of two large aspherical Fresnel lenses ($\approx$ 1 m^2). EUSO-Balloon flew during one night and it's Fresnel optics contributed to the observation of laser tracks in the atmosphere and the measurement of the UV night-time emission. However, the performance of the optics remained misunderstood i.e. the efficiency and the point spread function. This work describes the method used to characterize the optics performance and global efficiency of the Fresnel lenses of EUSO-Balloon. The measured performance of the optics can be understood as the combination of a semi-empirical diffusion model with a classic ray tracing simulation.

EUSO-SPB1 took data during 12 nights until the termination of the mission. We present an analysis of events found in triggered data while searching for air showers. We classify these events into different populations whose characteristics and origins we discuss. We show that the majority of our triggered events are direct cosmic ray interactions on the detector as well as instrumental features of the photo-multipliers. No air shower candidate was found in the analysis.

Keywords: Ultra High Energy Cosmic Rays, Extensive Air Showers, Fresnel Optics, Data Analysis

Résumé

Les Rayons Cosmiques d'Ultra Haute Énergie (RCUHE) sont des particules chargées venant de l'espace avec des énergies $>10^{18}$ eV jusqu'à une énergie mesurée de 3×10^{20} eV. Ils sont les messagers cosmiques les plus énergétiques, cependant leur origine et les mécanismes permettant leur accélération restent inconnus. Leur observation est difficile à cause de leur très faible flux (1 particule par stéradian par km^2 par siècle) et nécessite des techniques de détection indirectes, utilisant l'atmosphère comme un calorimètre. Le projet JEM-EUSO a pour but le développement d'un télescope spatial capable d'observer les gerbes atmosphériques produites par les RCUHE par le biais de leur émission de fluorescence en UV (300 - 400 nm). Pour atteindre ces objectifs, deux projets ballons démonstrateurs ont été développés afin de tester la technologie et les méthodes requises: EUSO-Balloon et EUSO-SPB1, qui ont volé en 2014 et 2017 respectivement.

Une technologie clé de ces démonstrateurs est leur système d'optique réfractive composé de deux larges lentilles de Fresnel (≈ 1 m^2). EUSO-Balloon a volé pendant une nuit et son système optique a contribué à l'observation de traces de laser et la mesure du bruit de fond UV. Néanmoins, la performance des optiques est restée mal comprise, i.e. l'efficacité et sa fonction d'étalement du point (PSF). Ce travail explique la méthode utilisée pour caractériser la performance de l'optique et l'efficacité globale des lentilles de Fresnel. La performance mesurée peut être comprise par la combinaison d'un modèle de diffusion semi-empirique avec une simulation classique de tracé de rayon.

EUSO-SPB1 a collecté des données pendant 12 nuits. On présente l'analyse des événements enregistrés suite au déclenchement de l'algorithme de "trigger". On classifie ces événements en différentes catégories et on discute leurs caractéristiques. On montre que la majorité des événements enregistrés sont des rayons cosmiques qui interagissent directement avec le détecteur ainsi que des défauts instrumentaux sur les tubes photomultiplicateurs du détecteur. Aucune gerbe atmosphérique n'a été trouvé dans cette analyse.

Mots clés: Rayons Cosmiques D'Ultra Haute énergie, Gerbes Atmosphériques, Optique de Fresnel, Analyse des données

Contents

List of Figures

List of Tables

Table of acronyms

CCB	Cluster Control Board
CR	Cosmic Ray
CNES	Centre National d'Etudes Spatiales
CSU	Colorado School of Mines
DP	Data Processor
EAS	Extensive Air Shower
EC	Elementary Cell
EUSO	Extreme Universe Space Observatory
FLT	First Level Trigger
FoV	Field of View
GLS	Global Light System
GM	Geiger-Müller
GZK	Greisen–Zatsepin–Kuz'min
IRAP	Institut de Recherche en Astrophysique et Planetologie
ISS	International Space Station
JEM	Japanese Experiment Module
MAPMT	Multi-Anode Photo-Multiplier Tube
PD	Photo-Diode
PDM	Photo Detector Module
PMT	Photo-Multiplier Tube
PSF	Point Spread Function
SLT	Second Level Trigger
SPB	Super Pressure Balloon
UHECR	Ultra High Energy Cosmic Ray

Chapter 1

The Search for Ultra High Energy Cosmic Rays

The earth is constantly bombarded by highly energetic charged particles originating from outer space that interact with the atmosphere creating cascades of secondary particles. These particles are called cosmic rays (CR) and their energy spectrum span multiple orders of magnitude: from 10^6 to above 10^{20} eV. Of particular interest for this work are the CRs with energies above 10^{18} eV, the so called Ultra High Energy Cosmic Rays (UHECR). Ever since their discovery, over a century ago, the CR spectrum has been through decades of intense experimental effort. Today we know the CR spectrum mostly proton dominated up to about 10^{15} eV and that a extremely small fraction of them have energies above 10^{20} eV with a record measured energy of 3×10^{20}. This tremendous energy is beyond comparison with everything known to humankind and despite great technological advances in CR detection techniques, several fundamental aspects about their nature are still puzzling scientists today. This can be resumed in three main questions:

- What are the astrophysical sources of UHECR?
- What are the physical mechanisms that accelerate UHECR to such energies?
- What is the composition of UHECR?

To answer these questions, the objective is to accumulate enough observations of these high energy particles. The current problematic is that their low flux makes the observational goal a non-trivial task: about 1 particle km^{-2} sr century for E $> 10^{20}$ eV. Moreover, the direct detection of UHECRs is impractical so we resort to the observation of the atmospheric particle cascades produced by their interaction in the atmosphere. These cascades are known as Extensive Air Showers (EAS). The current experimental efforts are focused on maximizing the observational exposure acceptance to increase the chances of detecting such rare events.

In this chapter we will review the historical development of the CR field, the CR spectrum and it's astrophysical implications. A simple Heitler model that describes the main features of EAS as well as the current detection techniques employed to observe UHECRs.

1.1 A brief history of Cosmic Ray research

We will review the history of cosmic ray science by focusing on the experimental efforts that led to three main events: the discovery of cosmic rays and determination of their particle nature, the discovery of extensive air showers and the discovery of the first event with an energy above 10^{20} eV.

1.1.1 Discovery of cosmic rays

At the end of the 19^{th} century the phenomenon of radioactivity was discovered by Henri Becquerel. Soon afterwards it was recognized that electroscopes, an instrument classically used to detect the presence of electric charge, became spontaneously discharged in close proximity of radioactive material. Thus, electroscopes became the standard instrument for the study of ionizing radiation.

One of the first conundrums faced by scientists in the field was the slow discharge of electro-meters in the absence of radioactive material. Even with shielding, the discharge rate was reduced but remained constant, so there appeared to be some form of background radiation. It was proposed by some authors that this background radiation was due to γ rays emanated by radium on the earth's crust and smaller radium emanations in the atmosphere. Thus it was proposed that the ionization rate would decrease as a function of the distance from the earth's surface [1].

In 1912 Victor Hess performed seven balloon flights to test this background radiation [2]. He measured the ionization rate in the atmosphere equipped with Wulf electroscopes, the state of the art detector. Different altitude incursions during his campaign showed that the ionization rate increased with higher altitude. He performed flights during night and a partial eclipse but this had no effect on the ionization rate. From his experiment Hess concluded that this mysterious radiation came from outer space and called it "*Höhenstrhalung*" (high radiation). Figure 1.1 shows Victor Hess preparing for one of his iconic balloon flights.

The discovery of "*Höhenstrhalung*" went mostly unnoticed and World War I put a hold on most research activities. It was until 1925 when the phenomenon regained attention due to its "re-discovery" by Robert Millikan. It was Millikan who coined the term "Cosmic Rays" believing them to be electromagnetic radiation[1]. For a while the radiation was named Millikan Rays" by media and other scientists. Fortunately, it was quickly pointed out that this was the same phenomenon discovered by Hess in 1912 and he was justly awarded the Nobel Prize in 1936.

[1]The term normally used for electromagnetic radiation was rays. Despite CRs not being electromagnetic radiation, the name stuck.

Figure 1.1: Victor Hess during one of his iconic balloon flights

1.1.1.1 The particle nature of cosmic rays

At the time of Cosmic rays discovery the only known forms of penetrating radiation were α, β and γ rays. Consequently CRs were believed to be γ rays up until the 1930s. However, the high penetration power of CRs led to speculations that there could be other forms of radiation. These opposing views created a heated debated about the nature of CRs. The development of Geiger-Muller counters, the coincidence technique and cloud chambers made possible major progress in the field.

The coincidence counting method developed by Walter Bothe [3] and the Geiger-Müller (GM) counter developed by Hans Geiger and Walther Müller in 1928 [4] were crucial for experimental advances in the field. In 1929 Walther Bothe and Werner Kolhörster designed a major experiment to determine if CRs were γ rays or charged particles [5]. From the results of their experiment, Bothe and Kolhörster concluded that cosmic rays were highly penetrating charged particles. The final blow was given when Arthur Compton demonstrated the geomagnetic latitude dependence of CRs [6], firmly establishing the particle nature of CRs. This new view on the nature of CRs opened a new panorama regarding their origin and cosmological implications, effectively establishing CR research as another major branch of physics.

Cloud chambers were developed in 1911 by Charles Wilson and allowed him to produce

photographs of $\alpha-\beta-$ and X-rays [7]. The devices consist in a sealed volume containing moist air that reaches a supersaturated state by fast expansion. The passage of a ionizing particles results in a trail of gas ions which act as condensation nuclei. Tiny water droplets condensate forming a cloud track that allows to visualize the passage of the particle. A constraint of the cloud chamber is that the supersaturation condition lasted only a few seconds so a periodic expansion of the air was necessary. This operational constraint resulted in setups that randomly "triggered" the chamber by expanding the air and taking photographs. Cloud chambers were used to detect first subatomic particles in the 1930s: the Positron, Muon and Kaon. All using CRs as the source of ionizing radiation.

1.1.2 Discovery of Extensive Air Showers

Shortly after the publication of the Bothe and Kolhörster results, the coincidence method was further refined by Bruno Rossi [8]. He developed a vacuum-tube device capable of registering the coincidences from any number of counters with a tenfold improvement in time resolution. With his improvement he established three-fold coincidences. This reduced the accidental coincidences and improved the detection of rare cosmic ray events.

In 1932 Blackett and Occhialini placed GM counters above and below a vertical cloud chamber. This way particles passing through the counters would also pass through the cloud chamber and trigger its expansion with the coincidence signal [9]. This marked the birth of "rare event triggering" another essential technique in cosmic ray and high energy physics research ever since. The improvement allowed to enhance the number of CRs photographed.

In 1933 Rossi reported crucial observation with his improved detector. He noticed that the coincidence rate between three adjacent GM counters increased when he placed an absorber plate between the counters and the coincidence rate only decreased until the absorber reached a certain thickness. These plots describing the coincidence rate as a function of the material thickness became known as the Rossi's transition curves. From this observation he correctly concluded that secondary particles were produced by the cosmic rays entering the material and they were increasingly absorbed as a function of the material thickness [10]. Figure 1.2 show the experimental arrangement Rossi's transition curves.

An observation similar to Rossi's was reported in 1935 by Regener and Pfotzer. They studied vertical intensity of cosmic rays up to a height of 28 km by measuring the rate of three-fold coincidences on a stratospheric balloon flight. They observed an unexpected maximum in the coincidence rate at about 14 km above sea level [11], this effect became known as the "Pfotzer maximum". Later, Regener correctly interpreted the results were due to the multiplication of electrons in the atmosphere which he called "shower".

In 1934 Rossi observed that there was a correlation in the arrival time of particles at detectors that were widely separated. He named this phenomenon Sciami". In 1938, Schmeiser and Bothe (unaware of Rossi's 1934 results) reported that particles in air showers were separated

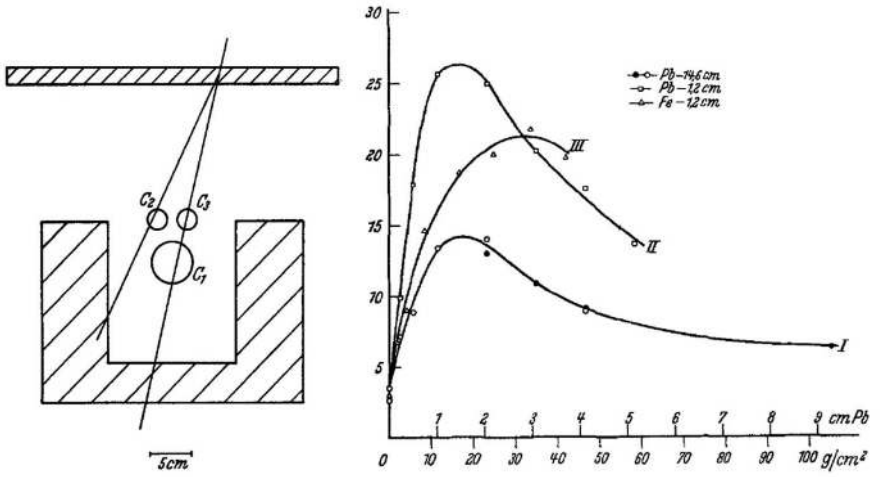

Figure 1.2: *Left:* Rossi's setup consisting of a triangular array of Geiger-Müller counters inside a lead box. The top lid could be removed and replaced by a lid of different material, thickness and distance from the detector *Right:* The coincidence rate shown as a function of the lead or iron lid placed above the detectors. From [10]

up to 40 cm. Furthermore, they pointed that Rossi's transition curves implied that "showers" were produced in air and named them "air showers". Independently at the same time, Kolhörster and his group reported similar data by showing the rate at which coincidences between pairs of GM-counters decreased as a function of separation [12].

Ultimately, despite the work of Rossi, Schmeiser and Bothe, and Kolhörster, the credit for the discovery of Extensive Air Showers (EAS) was given to Pierre Auger and his team. In 1939 they performed an experiment in the swiss alps. They separated their GM counter triggered cloud chambers by 300 m and measured coincident events. The highlight of their discovery was the estimation the primary energy of an event to be around 10^{15} eV, a five orders of magnitude leap to what was previously know in the 1930s. This formalized the discovery of EAS and for a while the phenomenon was called Auger Showers. Shortly after the discovery many features of EAS were quickly understood from the work of Auger. However, experimental work was halted for almost a decade, once again due to war.

1.1.3 The first event above 10^{20} eV

New advances in the field became possible due to the increasing availability of photomultiplier tubes (PMTs) and the use of liquid scintillators. Despite PMTs being available since the 1930s, their use on cosmic rays studies started until the 50s mainly focused on the study of Cherenkov light produced by EAS. PMTs are capable of detecting very faint light, even single photons, and yet produce detectable signals. Coupled with scintillators, PMTs started to replace GM counters as the detectors for cosmic ray studies.

Rossi realized that the inexpensiveness and fast decay time of scintillators would allow him to build a large area detector using PMTs to detect the scintillation light. To test this, his team build an array of three detectors consisting of 20 liter drums of 600 cm^2 arranged in various configurations. Bassi, Clark and Rossi [13] showed that the direction of air showers could be determined without the use of cloud chambers by measuring electronically the arrival time of the shower particles. This is because the secondary particles are highly relativistic and form a think disk region around the shower core.

This pioneering experiment led to the development of a larger array at the Agassiz site in Harvard university which started operations in 1954. The Agassiz array consisted in 15 0.9 m^2 scintillators. In 1955 a lightning set on fire the inflammable liquid scintillators briefly stopping the work. This prompted the team to develop plastic scintillators and then the work was resumed and continued until 1957. The major achievements of the Agassiz array included being the first experiment capable of measuring the energy and direction of cosmic rays greater than 10^{15} eV. It measured the spectrum from 10^{16} up to about 10^{18} eV [14]. The group also developed analysis methods that were useful in the analysis of data from future arrays.

The Agassiz array proved that the method was so economical that other arrays were soon developed using Agassiz' technology. In 1957, Rossi put John Linsley in charge of designing a larger array to study higher energy events. The new array was located at Volcano Ranch, New Mexico. It was built by Linsley and his colleague Livio Scarsi and became operational in 1957. The array consisted in nineteen 3.3 m^2 detectors arranged in a hexagonal pattern with an initial spacing between detectors of 442 m. Later the distance was expanded to 884 m becoming the first array to cover more than 1 km^2. Observations from Volcano ranch extended the known cosmic ray spectrum, improved the understanding of the structure of EAS, provided the first experimental results on UHECR composition and the first evidence of anisotropy from the arrival direction of CRs [15]. Most notably the Volcano Ranch array was the first experiment to detect an UHECR with an energy higher than 10^{20} eV [16], still one of the most energetic events detected to date.

For the next decades and up to this day, array experiments continue dominate the cosmic ray field. A particular trend is that these experiments have become larger in order to increase their observational exposure and detect more events. These experiments have proven important in understanding particular features of the CR energy spectrum (see sec. 1.2), in the development of models of EAS development and computational methods. Also other techniques were developed almost in parallel to arrays. These techniques rely on optical observations to detect the fluorescence (see sec. 1.4.2) and Cherenkov light (see sec. 1.4.3) produced by EAS. Newer arrays have incorporated a hybrid observation approach to complement both type of measurements to improve their performance.

1.2 Cosmic ray energy spectrum

As we have seen, the study of the cosmic ray spectrum has taken many decades. It spans over 8 and 24 orders of magnitude in energy and flux respectively. A feature of the CR spectrum is that it can be described over large energy regions by an broken power law E^s with an spectral index s which varies according to the region. The spectrum is divided mainly in four regions: from 10^9 to 10^{15} eV the spectral index is $s \approx -2.7$, at $\approx 3 \times 10^{15}$ eV the spectrum steepens to $s \approx -3.1$, at $\approx 4 \times 10^{17}$ eV there is a second steepening to $s \approx -3.3$, at $\approx 4 \times 10^{19}$ eV the spectrum flattens to $s \approx -2.6$ and around 10^{20} eV there is an apparent cutoff in the spectrum. The spectral index transition regions are respectively called the "knee", the "second knee" and the "ankle" of the CR spectrum. Figure 1.3 shows the all particle cosmic ray spectrum as measured by various experiments developed through several decades, one can clearly see the spectral index transitions which give the knee and ankle their respective names.

The knee region is typically assumed to represent the end of the galactic cosmic accelerators spectrum whereas the ankle is assumed to represent the emergence of extragalactic ones [18]. This is assumed because the Larmor radius of a particle with an energy of about 10^{20} eV will be larger than the size of the galactic disc. Therefore, the conditions to confine UHECRs make it reasonable to assume that they are of extragalactic origin and motivates the search for sources outside of the Milky Way.

Candidate acceleration sources must meet certain size and magnetic field strength conditions to accelerate particles to extreme energies. These conditions were summarized by Hillas [19] and represented graphically in the so called Hillas plot shown in figure 1.4. The plot marks the magnetic field strength and radius necessary to accelerate and confine UHECR proton and iron nuclei with an energy of 10^{20} eV, denoted by the diagonal lines. Anything below the line is not a viable source.

In the next section we will review two significant effects that affect the propagation of CR in the galactic and extragalactic medium and review potential acceleration mechanisms and sources proposed in the literature.

1.2.1 UHECR Propagation

The question of the origin of CR is tightly connected with the propagation of cosmic rays in the galactic and intergalactic medium. Upon their arrival on earth, CRs have already traveled vast distances, suffering energy losses and deviations due to the interaction with the interstellar/intergalactic medium. This affects the observations and limit the ability to trace back the CR to a particular source.

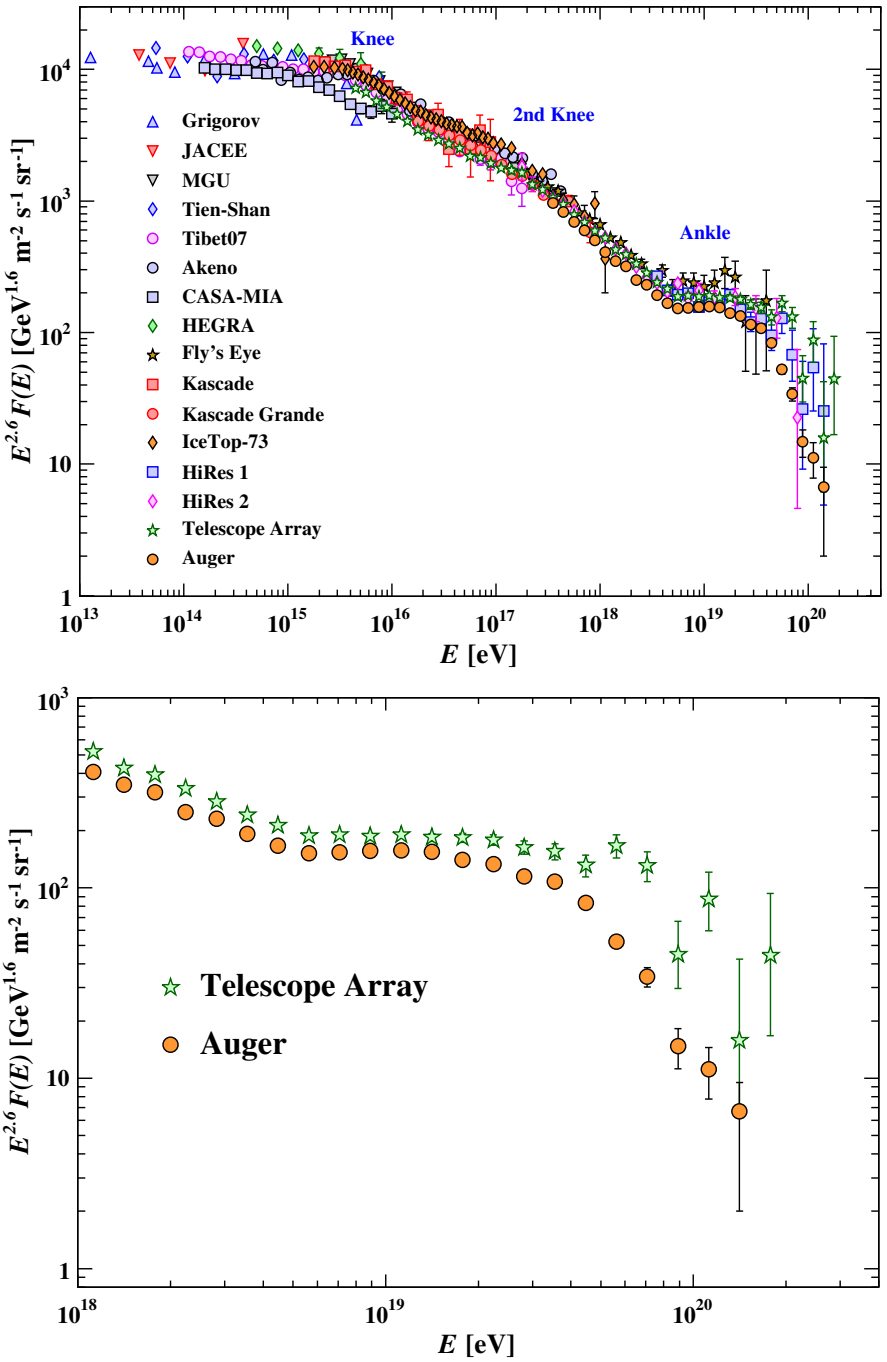

Figure 1.3: *Top:* All particle cosmic ray spectrum as a function of E (energy per nucleus) measured by multiple experiments. *Bottom:* Zoom into the high energy portion of the spectrum with data from the Telescope Array and Pierre Auger observatory. Plot from [17]

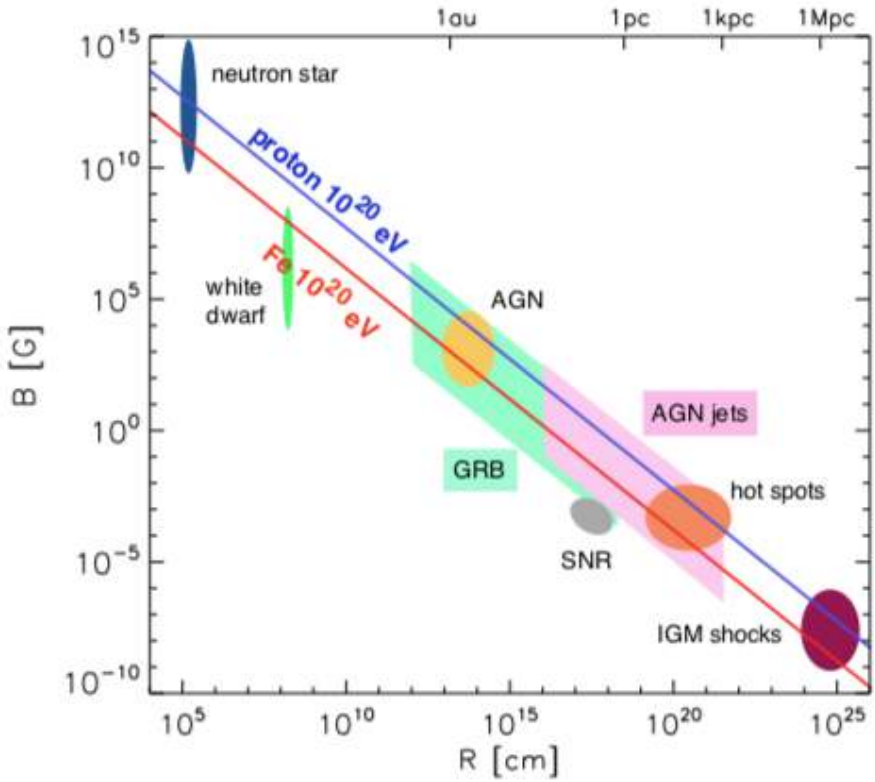

Figure 1.4: Updated Hillas diagram showing the proton and iron confinement lines. Possible sources are: neutron stars, active galactic nuclei (AGN), gamma ray bursts (GRB), inter galactic medium (IGM) shocks. Plot from [20]

1.2.1.1 The GZK cutoff

In 1966 K. Greisen [21], G. Zatsepin V and Kuz'min [22] independently realized that the photons of the cosmic microwave background (CMB) made the universe opaque to protons and nuclei of ultra high energies and predicted an upper limit on the energy of cosmic rays due to the interaction of UHECR with the primordial photons. This effect is named the "GZK cutoff" after the authors and occurs for protons with energies above the photo-pion production threshold, at about 3×10^{19}

$$E_{th} = \frac{m_\pi(2m_p + m_\pi)}{4\epsilon} \approx 3.4 \times 10^{10} \left(\frac{\epsilon}{10^{-3}\text{eV}} \right)^{-1} \text{GeV} \tag{1.1}$$

$$\gamma_{CMB} + p \rightarrow \delta^+ \rightarrow p + \pi^0 \tag{1.2}$$

$$\gamma_{CMB} + p \rightarrow \delta^+ \rightarrow n + \pi^+ \tag{1.3}$$

The GZK cut-off implies that UHECR are cosmologically young and should come from relatively close sources.

1.2.1.2 Effect of magnetic fields

Being charged particles, the rigidity[2] of a CR plays an important role in it's propagation through the galactic and extragalactic medium magnetic fields. Depending on the strength of the magnetic fields and energy of the CR, its trajectory can be significantly deviated, affecting the accurate determination of the source location. For instance, by means of simulations shown in figure 1.5, we can see that a turbulent magnetic field of about 10 nG significantly affects the propagation of CRs with E $< 10^{20}$ eV and the source direction is totally lost. Only a CR above this energy can maintain an almost ballistic trajectory [23].

1.3 Extensive Air Showers

When a cosmic ray or high energy photon arrives to earth, it interacts with the nuclei of air molecules, producing a flux of secondary, tertiary and ensuing generations of particles. This event forms a particle cascade called Extensive Air Shower (EAS) which develops longitudinally along the arrival direction of the primary particle. As the shower develops, the newly produced secondaries become less energetic since the energy of the primary particle is distributed among newly generated particles. Figure 1.6

[2]The rigidity is a measure of a charged particle's momentum and refers to the resistance of a particle to be deflected by a magnetic field.

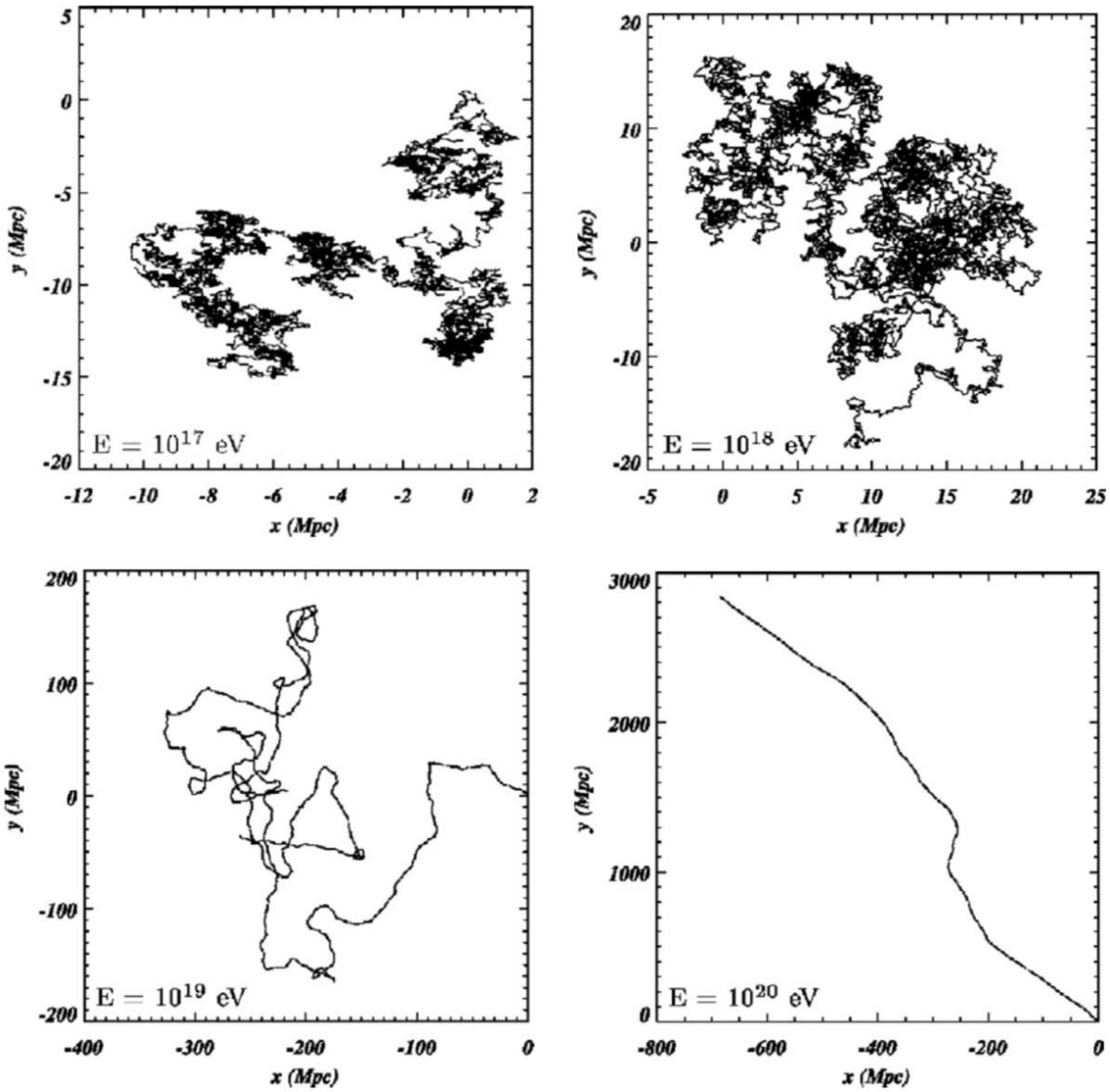

Figure 1.5: Propagation of UHECR protons of different energies in a magnetic field of 10 nG. The panels from top left to bottom right show simulations of protons with an energy of: 10^{17}, 10^{18}, 10^{19} and 10^{20} eV. Only the 10^{20} eV can be traced back to the source.

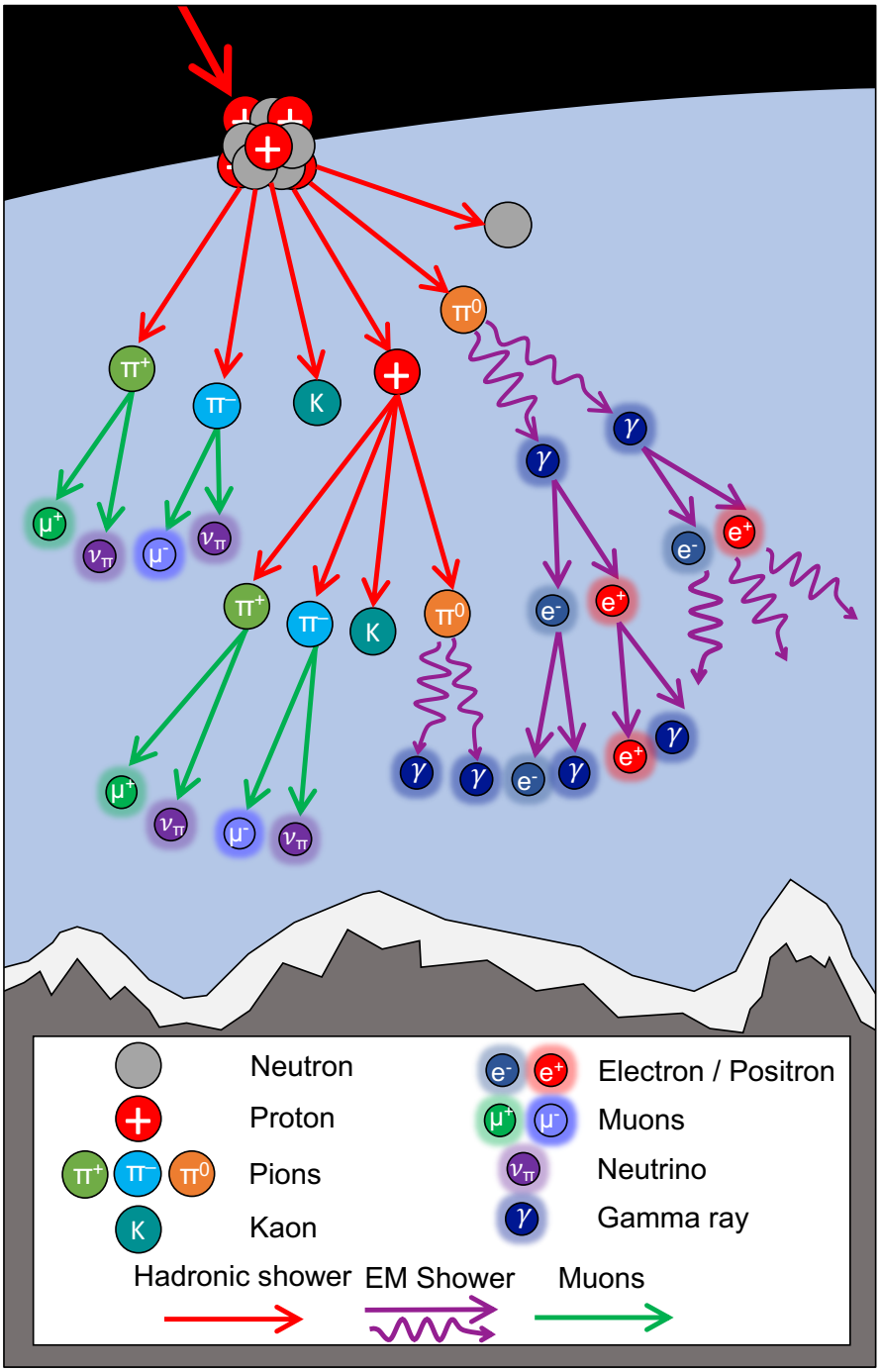

Figure 1.6: Schematic of an EAS showing it's hadronic, electromagnetic and muonic component.

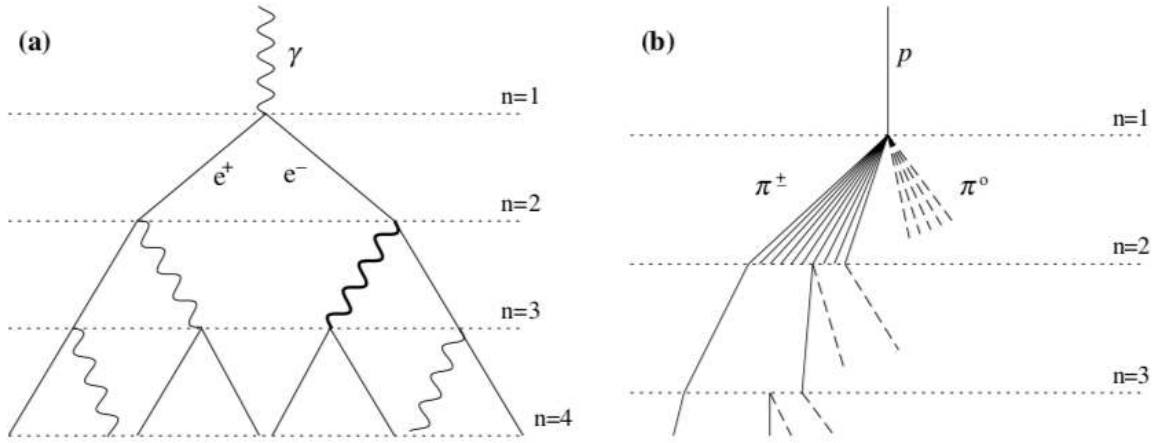

Figure 1.7: Heitler's Model of electromagnetic shower development.[24]

Depending on the primary of the event (particle or photon) the shower development has different characteristics, e.g. proton initiated showers are wider than γ ray ones. A good starting point for understanding EAS is Heitler's model. This model was initially developed for electromagnetic (EM) showers and has been extended to the case of hadronic showers by Matthews [24]. Although the model is simple and does not take into account all details of an EM shower it is good to show the physics involved and manages to predict accurately the most important characteristics of EM shower development.

1.3.0.1 Electromagnetic showers

In Heitler's model (see fig 1.7a), an EM shower involves electrons (e^-), positrons (e^+) and photons (γ) which experience a repeated two particle ($e^\pm$ and γ) multiplication after they travel a fixed distance (d) related to the radiation length in the medium (λ_r) by $d = \lambda_r \ln 2$. The multiplication is done by two main processes: one-photon Bremsstrahlung and e^-e^+ pair production. After n splitting lengths, with a distance of $x = n\lambda_r \ln 2$, the number of particles in the shower ((e^- and γ) is $N = 2^n = e^{x/\lambda_r}$. The multiplication process is halted when the individual e^-e^+ energies fall below the critical energy (ξ_c^e) threshold. At this point the particle energy is too low for pair production and bremsstrahlung due to the radiative losses being lower than the collision energy losses. In air the critical energy is 85 MeV.

If we consider a shower started by a photon of energy E_0. The cascade reaches its maximum size $N = N_{max}$ when all particles have the critical energy ξ_c^e so that

$$E_0 = \xi_c^e N_{max} \tag{1.4}$$

The EM shower reaches it's maximum size at the penetration depth X_{max}, this is obtained by calculating the number of splitting lengths n_c required so the energy per particle is reduced

to ξ_c^e. Since $N_{max} = 2^{n_c}$ from eq. 1.4 we obtain that $n_c = \ln[E_0/\xi_c^e]/\ln 2$ which gives

$$X_{max} = n_c \lambda_r \ln 2 = \lambda_r \ln[E_0/\xi_c^e] \tag{1.5}$$

The elongation rate Λ, defined as the rate of X_{max} change per decade of primary energy, is given by:

$$\Lambda \equiv \frac{dX_{max}}{d \log_{10} E_0} \tag{1.6}$$

Using the X_{max} from eq. 1.5 yields an elongation rate $\Lambda = 2.3\lambda_r = 85$ g/cm^2 for EM showers in air.

The model overestimates the number of particles at the shower maximum by a factor of two to three. This happens because multiple photons are radiated during bremsstrahlung which leave the electron with less energy to maintain the multiplication process and also because the model does not treat the loss of particles as ionization ceases to occur.

Taking these effects into account in simulations show that there is a photon to electron-positron number ratio of about six. This is one order of magnitude less electrons than what is predicted by Heitler's model N_{max} and holds true for higher energies and other type of media. If we wish to extract the number of electrons N_e from Heitler's shower size N we can adopt the correction factor:

$$N_e = N/g \tag{1.7}$$

Where g = 10 and is a simple order of magnitude estimate. Overall, despite the shortcomings of the model it helps to understand the EM shower development and predicts two important features:

1. The maximum size of the shower is proportional to the primary energy E_0
2. The depth of shower maximum X_{max} increases logarithmically at a rate of 85 g/cm^2 per decade of primary energy.

1.3.0.2 Hadronic showers

In the hadronic shower model, the atmosphere is assumed to consist of fixed thickness layers $\lambda_I \ln 2$. λ_I is the interaction length of strongly interacting particles and it is assumed to be constant. For pions in air $\lambda_I \approx 1120$g/cm^2. After traversing one layer, the Hadrons interact producing N_{ch} charged pions ($\pi^{\pm}$) and $\frac{1}{2}N_{ch}$ neutral pions (π^0). Neutral pions decay into

photons, initiating splinter EM showers whereas charged pions continue interacting through subsequent layers. This process is repeated until the charged pions are below the critical energy (ξ_c^π) where they are assumed to decay into muons.

If we consider a primary cosmic ray proton that enters the atmosphere with an energy E_0, then after traversing n layers of atmosphere there are $N_\pi = (N_{ch})^n$ charged pions. If we assume an equitable distribution of energy in the particle production process then these pions will carry a total energy of $(\frac{2}{3})^n$, with the remainder energy gone into splinter EM showers from neutral pion decay. Thus the energy per charged pion in the atmospheric layer is:

$$E_\pi = \frac{E_0}{(\frac{3}{2}N_{ch})^n} \tag{1.8}$$

knowing that one third of the primary energy is lost at each interaction stage due to neutral pion decay which then initiates splinter EM showers. Then, to calculate the primary energy we have to include the hadronic and EM shower component. This is done by using the total number of pions N_π and EM particles N_{max} from the splinter showers. Similar to eq. 1.4 the total energy is:

$$E_0 = \xi_c^e N_{max} + \xi_c^\pi N_\mu$$

Scaling to the electron size $N_e = N_{max}/g$, then

$$\begin{aligned} E_0 &= g\xi_c^e\left[N_e + \frac{\xi_c^\pi}{g\xi_c^e}N_\mu\right] \\ &\approx 0.85GeV(N_e + 24N_\mu) \end{aligned} \tag{1.9}$$

1.4 UHECR detection Methods

Since their discovery and through most of their observational history, cosmic rays have been detected in an indirect manner. Nowadays, thanks to space technology we can directly detect primary particles above the atmosphere. One example is the AMS-02 (Alpha Magnetic Spectrometer) instrument placed in the International Space Station since 2011, which has detected almost 150 billion CR events as of 2019 [25][3]. However, the flux above 10^{15} eV becomes too low for direct detection. Therefore, we still resort to the indirect observation UHECRs through EAS and its constituents. The following techniques are the most important methods for indirect observation of UHECRs.

[3]The AMS-02 website includes a counter of the detected CR events. https://ams02.space/

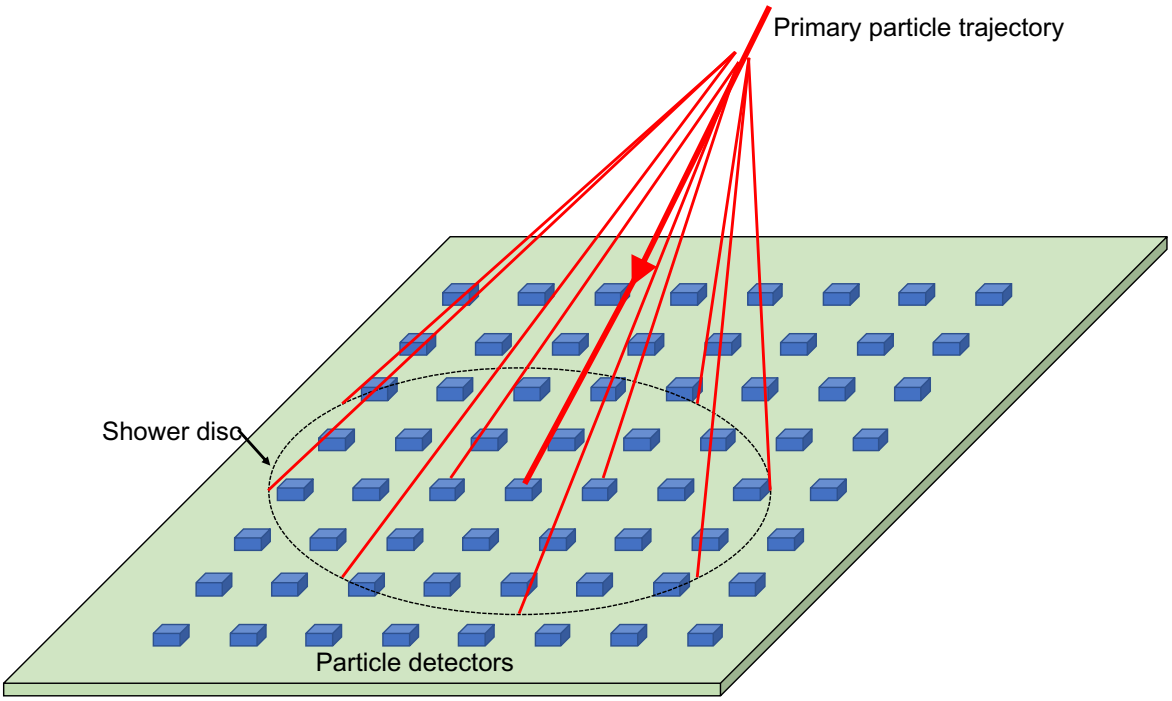

Figure 1.8: Depiction of a surface array experiment. The array is formed by individual detectors that can be equally or unequally spaced from each other. The thick red line denotes a shower core

1.4.1 Surface detector arrays

As we have seen, surface detector arrays are the oldest and still the most common method for EAS study. The arrays consist in a large number of particle detectors typically arranged in a grid. The spacing of each element in the array varies as a function of the energy range that the experiment is optimized for. Today each element in the array consists in a self-sufficient station that includes the detector, a power station and telemetry systems. An example of a surface array experiment is schematically depicted in figure 1.8

There are two main types of surface detectors used in current observatories: scintillation detectors and tanks filled with water that detect the Cherenkov light produced by the relativistic particles propagating in the water. Both types use photomultiplier tubes to detect the scintillation and Cherenkov light. Figure 1.9 shows an example of each type of array unit used in the Telescope Array [26] and Pierre Auger [27] observatories.

The EAS are detected by monitoring and triggering on coincident signals in multiple detectors. The shower size is determined by sampling the energy deposits in the detectors struck by the event. From the sampled data the shower size is computed by integrating a particle lateral distribution function (LDF) over the entire area impacted by the shower [28]. The LDF is experiment dependent, since the detector spacing and altitude varies between experiments. The arrival direction of the primary is determined by the time delay of the shower particles

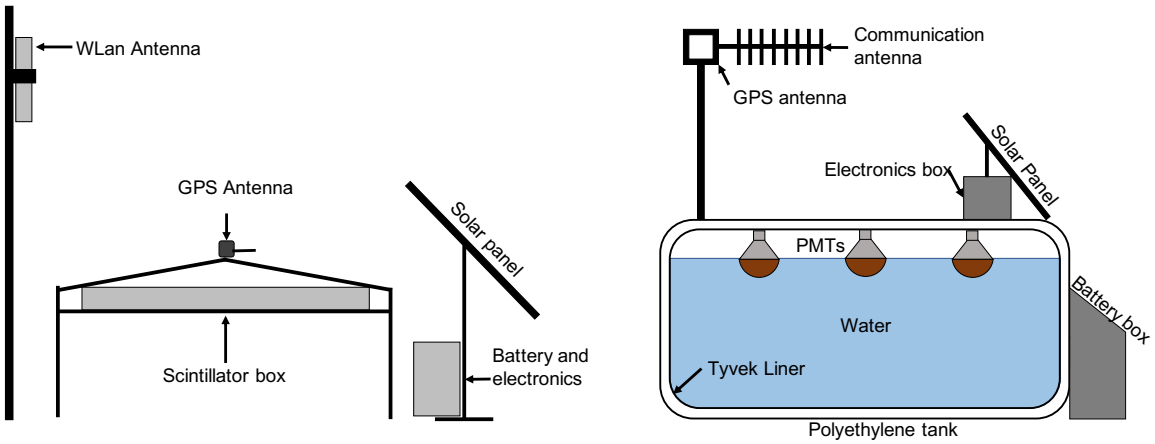

Figure 1.9: Surface arrays used for the detection of EAS. *Left:* Scintillation surface array of the Telescope Array observatory, adapted from [26]. *Right:* Cherenkov water tanks surface arrays of the Pierre Auger observatory, adapted from [27]

arriving in each detector. The angular resolution of the reconstructed trajectory depends on the distance and precision of the time synchronization between each station and the number of particles detected per station. The detector arrays can achieve an angular resolution of $\approx$1 to 2° for low energy showers and $\lesssim 0.5°$ for larger high energy showers [18]. Figure 1.10 shows one EAS event detected by the KASCADE experiment [29] where the shower core and arrival direction can be clearly observed.

1.4.2 Atmospheric air fluorescence

Fluorescence is the process in which atoms are excited by absorbing energy from a photon or charged particle and then relax, resulting in the emission of a photon of lower energy. The passage of the EAS charged particles through the atmosphere results in the excitation of the air molecules, mainly nitrogen. Some of the excitation energy is then re-emitted in the form of ultra violet and visible light in the 300-430 nm band. This wavelength band is of interest for the detection and reconstruction of EAS and is observed by UV telescopes. For the scope of this work we're interested in the fluorescence detection technique. Figure 1.11 shows the air fluorescence emission spectra [30].

The fluorescence emission is isotropic so the EAS development can be observed from any direction with a telescope offering the possibility of monitoring large volumes of air and observing the longitudinal profile of a shower development. In fluorescence telescopes the size of a shower can be determined as a function of it's longitudinal profile. From there the main shower parameters can be derived directly, such as the primary energy, E_0, and X_{max}. From the latter the mass of the primary M_0 can be determined. The reconstruction techniques for air fluorescence telescopes are detailed in [31]. Figure 1.12 shows the observation principle of a fluorescence telescope.

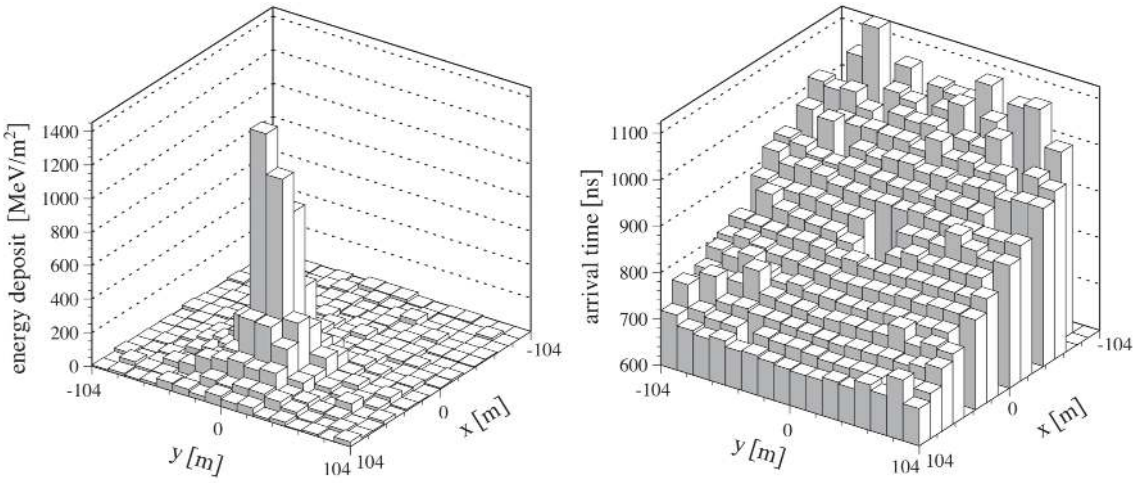

Figure 1.10: EAS event detected by the e/γ detectors of the KASCADE experiment. *Left:* The energy deposits, clearly showing the location of the shower core. *Right:* Arrival time of the shower particles. The difference in arrival time shows the curvature of the shower. Plot from [29]

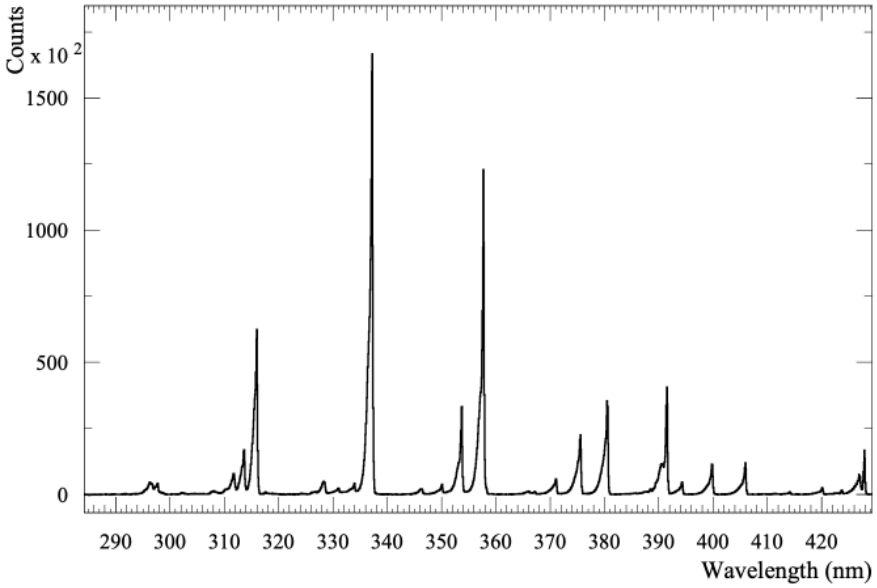

Figure 1.11: Air fluorescence emission spectra measured by the AIRFLY collaboration [30].

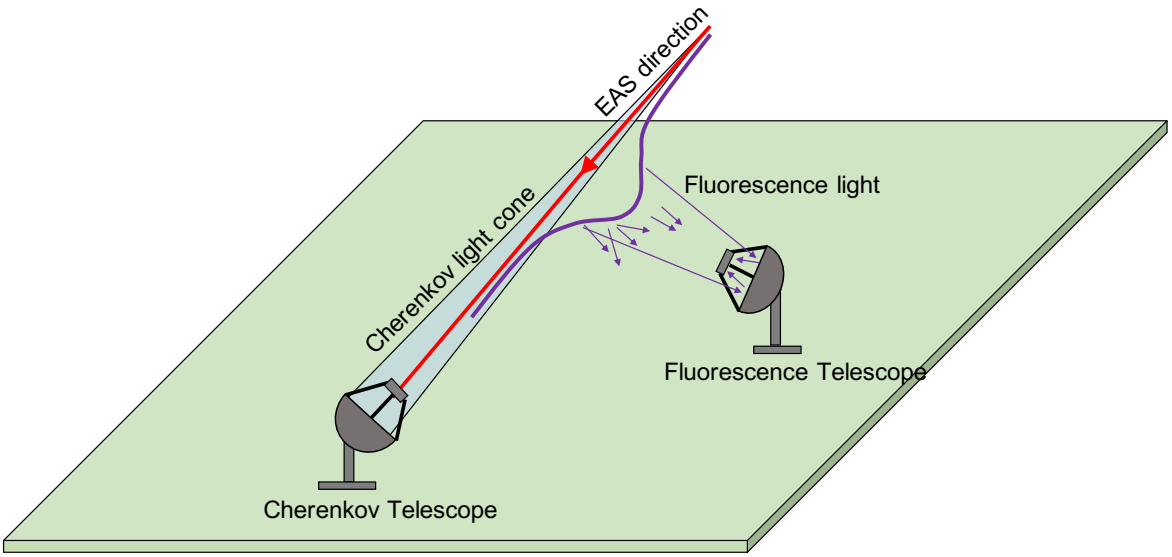

Figure 1.12: Schematic depicting the observation principle of an air fluorescence telescope and air Cherenkov imaging telescope. The isotropic fluorescence light can be observed sideways by the fluorescence telescope. The Cherenkov telescope requires to have it's FoV within the Cherenkov light cone.

One of the first efforts in air fluorescence detection was done by K. Greisen and A.N Bunner in the 1960s [32]. This experiment is interesting for our work because it's most likely the first time Fresnel lenses were proposed for fluorescence light collection. Figure 1.13 shows a schematic of the fluorescence detector used in this experiment. The detector featured an optical filter to reduce noise from the night-sky background and artificial light sources, a 0.1 m^2 Fresnel lens and a spherical focal surface of Photomultiplier tubes. It was triggered by requiring a coincidence between two adjacent pixels. This experiment was run for several years but it wasn't sensitive to UHECR because the lenses were too small to collect sufficient light. Also the atmospheric conditions of Ithaca, New York weren't the most adequate to observe such a faint light.

In 1976 a group from the University of Utah constructed three prototype fluorescence detector modules. They consisted of a 1.8 m diameter mirror and 14 PMTs at the focal plane. The prototypes were tested at the legendary Volcano Ranch site and were the first to detect fluorescence light from air showers in coincidence with the ground array, successfully establishing the technique. This led the group to the construction of a full-scale observatory in Dughill, Utah, which became the Fly's eye experiment[4] [33]. A second similar site named Fly's Eye II with the same characteristics was built to perform stereo observations. The science output of the observatory reached it's climax with the observation of an event of $3.2 \pm 0.9 \times 10^{20}$ eV. This is still the highest energy event observed to date.

[4]It was named so because each it's pixels subtended a FoV of about 5×5°covering the full sky in hexagonal segments, reminiscent of a fly's eye

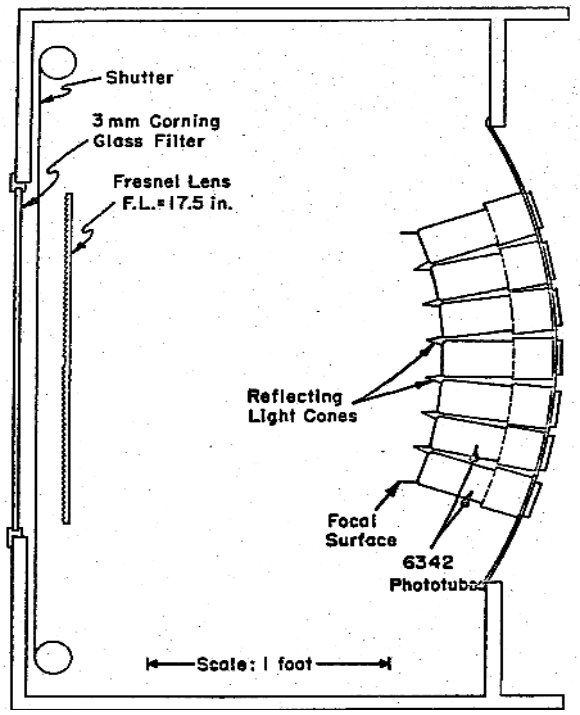

Figure 1.13: Schematic of the Cornell University fluorescence detector. The design consisted of an optical filter window, a 0.1 m^2 Fresnel lens and a focal surface formed by an array of PMTs. Schematic from [32]

1.4.3 Air Cherenkov arrays

When an EAS propagates through the atmosphere, the relativistic particles generated in the shower produce Cherenkov light since they travel faster in air than light. Cherenkov light is emitted primarily in the UV and blue wavelengths and propagates in a small cone centered around the propagation axis of the primary. The light can then be detected by an array of sensitive UV telescopes. Nowadays air Cherenkov arrays are mostly focused on γ ray astronomy through the observation of gamma ray initiated EAS. The telescopes are characterized by a large aperture, narrow field of view ($< 2°$) and high angular resolution. One example is the HESS experiment [34].

The event reconstruction is in principle similar as particle detector arrays. However, the LDF of the photons is different from that of charged particles. An advantage of the air Cherenkov method is that the light collected by the array contains photons from all the development stages of the shower. The optical component travels mostly unimpeded through the transparent atmosphere. Therefore, it provides a history of the shower development. However, the telescopes require clear night conditions to operate [35].

1.4.4 Radio Detection

In the 1960s it was discovered that EAS produce short radio bursts at frequencies around 40 MHz [36]. This sparked interest in the technique and further experiments confirmed the presence of EAS radio emissions in a frequency range of 10^1 to 10^2 MHz. Initially this proved to be a promising technique for the detection of EAS but by the 1970s technical difficulties and ambiguous results in radio measurements led to the loss of interest in the method and it was phased out in favor of the surface array and fluorescence techniques which showed more promising results. Nowadays, with the advent of the digital era and the ability to construct sophisticated digital antennas, the interest in the method has been renewed. New experimental initiatives in the technique include LOFAR (Low Frequency Array) [37] and the balloon experiment ANITA (Antarctic Impulsive Transient Antenna) [38].

The overall radio emission is composed by various mechanisms but the dominant one is the geo-synchrotron emission. During the development of the EM component of an EAS, e^+e^- pairs are produced with a pair number proportional to the energy of the primary. These charges will be subjected to a Lorentz force due to their passage through the Earth's magnetic field. The resulting forces on the e^+e^- pair are equal and opposite, leading to the separation and gyration of the charges and producing synchrotron radiation in the process. This geosynchrotron emission will show coherence over wavelengths longer than the transverse shower size. For UHECR induced EAS the emission will be fully coherent below about 100 MHz and partially coherent at higher frequencies [38].

1.4.5 Current UHECR Observatories

As of the writing of this thesis, there are two main observatories for the observation of UHECR: the Pierre Auger Observatory (PAO) and the Telescope Array (TA).

1.4.5.1 Pierre Auger Observatory

The PAO [39] is the largest air shower detector ever built, it is located in the high plains of Malargüe, Argentina. It consists of an array of 1660 Water Cherenkov Detectors (WCD) covering an area of about 3000 km^2 which is overlooked by 24 fluorescence telescopes equally distributed in four enclosure sites. Each fluorescence telescope has a field of view of 30°×30°which overlaps with other telescopes to make stereoscopic detections of an EAS event. Figure 1.14 shows a map of the PAO indicating the location of the particle detectors and the fluorescence detector enclosures. One of the sites named "Colhueco" also has other improvements close to it, including three high elevation telescopes (HEAT) overlooking a secondary detector array with a spacing of 750 m and a detector for radio and microwave (AERA) emissions of EAS.

Some of the main scientific results of the PAO include: establishing unambiguously the

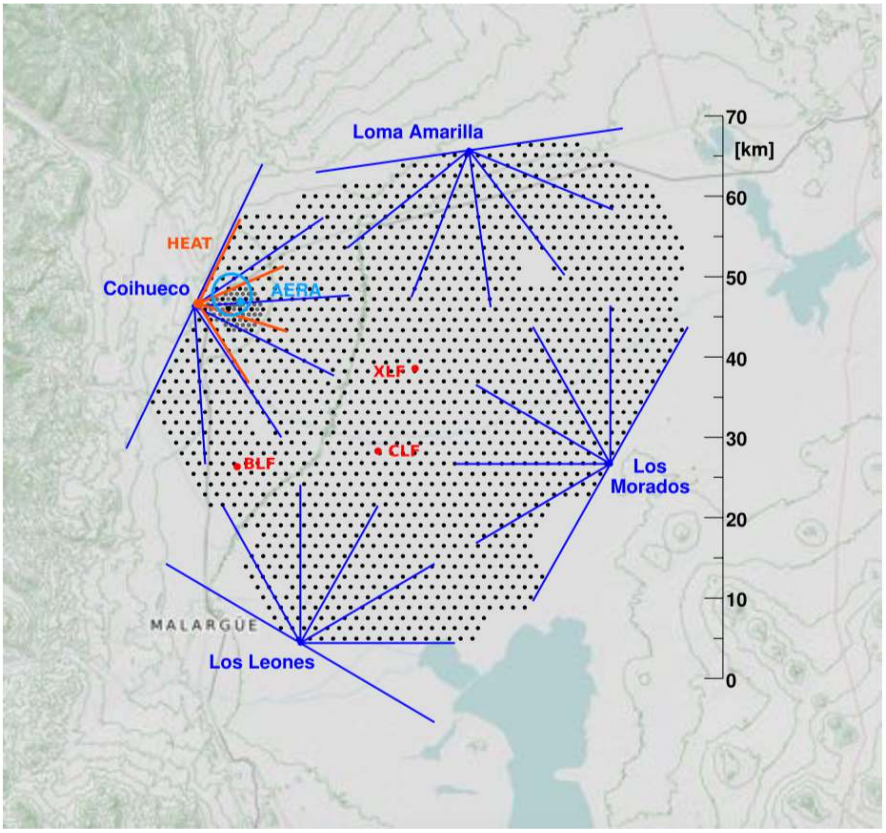

Figure 1.14: Map of the Pierre observatory indicating the location of the Water Cherenkov Detectors (black dots), the fluorescence detector enclosures (blue dots) and the field of view subtended by each fluorescence telescope (blue lines). Figure taken from [39]

suppression of the CR flux above $4{\times}10^{19}$ eV [39] and more recently the determination of anisotropy in the arrival direction of UHECRs with $E > 8 \times 10^{18}$ eV [40]; pointing towards an extragalactic origin for these particles. The success of the PAO has given motivation to perform a series of upgrades known as "AugerPrime" [39]. The upgrade includes adding 4 m^2 plastic scintillator detectors on top of all the WCD, updated surface detector electronics, a large array of buried muon detectors, and an improved duty cycle for the operations of the fluorescence detectors.

1.4.5.2 Telescope Array

The TA project [41] is also a hybrid UHECR observatory located in the high desert of Millard County, USA. It observes UHECRs with energies greater than 10^{18} eV. TA consists of 507 scintillation detectors with a spacing of 1.2 km covering an area of about 700 km^2 overlooked by 38 telescopes distributed in three fluorescence detector stations containing 12 to 14 telescopes each. The site includes a central laser facility (CLF) used to test and calibrate the fluorescence telescopes. TA was upgraded with the Telescope Array Low Energy (TALE)

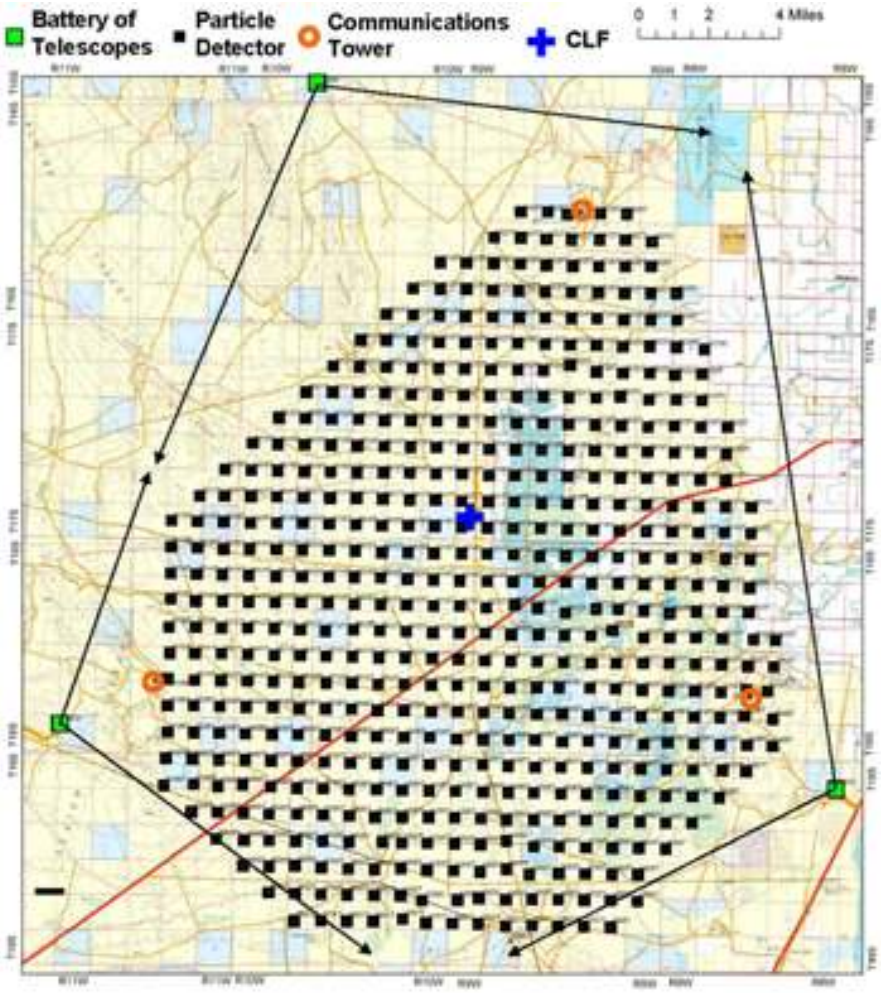

Figure 1.15: Map of the Telescope Array project indicating the location of the surface detectors (black squares), telescope enclosures (blue squares), communication towers (red circles) and their Central Laser Facility (CLF). Figure taken from [42]

extension [42] which reduces it's energy threshold to 3×10^{18} eV. The upgrade added 10 new telescopes to the TA site with improved electronics and a denser array of 103 new surface detectors. Figure

Chapter 2

Towards Space Detectors of UHECR: The JEM-EUSO Framework

The largest constraint in UHECR observations is the exposure needed to accumulate the statistics that will give us the confidence to solve the main questions regarding their origin. As an example, the Pierre Auger observatory, in almost 12 years[1] of operation and with its total exposure of 76,800 km^2 sr yr detected about 32,000 events with $E > 8 \times 10^{18}$ [40]. These observations led to a major announcement in 2017: the determination of anisotropy in the arrival direction of UHECRs, pointing towards an extragalactic origin for these particles. Nevertheless, a conclusive answer to the UHECR origin is still pending. Technically, with the overall capabilities of the current observatories it's likely a matter of time to get the answer. However, the desire to accumulate the exposure in a shorter time frame has encouraged the proposition and development of another approach towards UHECR observations: detection from space.

The observation of UHECR from space was first proposed by Benson and Linsley in 1981 [43]. They suggested a nadir pointing satellite flying on a circular orbit at an altitude of 500-600 km. The instrument would feature a 36 m telescope, a focal surface with 5000 photo-multipliers (about 5 cm diameter) and posses a circular view of about 100 km in diameter. Such an instrument would cover an area roughly three times larger than Auger. The idea was revolutionary for it's time but unfortunately it was unfeasible, mainly due to the huge optics, too large even by today standards and the limited imaging technology available in the 80s. But also by the technical and scientific challenges required for putting in orbit a project of this magnitude and detecting the faint photon flux buried in a myriad of artificial lights for a significant portion of the orbit duration.

Two decades later the idea was taken by Y. Takahasi who developed the concept of MASS: the Maximum energy Auger air Shower Satellite [44]. Takahashi contacted Linsley to discuss this idea and in turn Linsley discussed it with his old colleague Livio Scarsi. Eventually the concept evolved into MASS/Airwatch to improve it's appeal for space agencies. This became the turning point in the development of space missions for UHECR observation. In 1996, in

[1] From January 1st, 2004 to August 31st, 2016.

the USA the MASS concept evolved into OWL, the Orbiting Wide-angle Light concentrator, a dual satellite mission design to perform stereo observations of Air showers. In Europe the Airwatch concept evolved into EUSO, the Extreme Universe Space Observatory and was proposed to the European Space Agency (ESA) in 2000 with initial success. At first it was conceived as a satellite mission but then reoriented as a payload for the European Columbus module of the International Space Station (ISS) becoming ESA-EUSO. Several constraints led to the discontinuation of the program but it was rescued and redefined by Takahashi as an observatory attached to KIBO, the Japanese Experiment Module (JEM) of the ISS. The mission was now under JAXA funding, the Japanese space agency and the JEM-EUSO collaboration was born [45].

2.1 The JEM-EUSO Mission

The JEM-EUSO collaboration was formed with the aim of developing an Ultraviolet (UV) space telescope to observe EAS from space via the air fluorescence technique. The flagship instrument, the JEM-EUSO telescope, was planned to be installed on board the JEM of the ISS under the management and funding of JAXA. Unfortunately, JAXA withdrew it's offer to launch and operate the telescope, effectively canceling the mission. Before this event, extensive research had already been conducted to determine the feasibility and technical requirements for JEM-EUSO and preliminary technology was developed for its preparation. These efforts lead to the development of two balloon-borne prototypes which are central to this work: EUSO-Balloon and EUSO-SPB1 (Super Pressure Balloon). These two achievements are still driving other projects which will inherit the accumulated experience as Technological Readiness Level (TRL). We will review the motivation, legacy and highlight the major aspects of the mission which are relevant to this work: the optics and data acquisition.

Although the fluorescence technique is firmly established, doing so from space had never been done when the project was kicked-off. Moreover, the technological hurdles associated with spaceflight put large constraints and challenges on the development of such a project. For instance, the cost of putting a kg of mass in orbit plus the need to fit the instrument in the launch vehicle and the designated ISS location, compel the project towards a reduction in dimension and mass while trying to maintain a large FoV and fine angular resolution. Besides, the conditions experienced during launch and in orbit plus the lack of regular maintenance also require the instrument to be fully reliable during its operational lifetime. Sure, there are astronauts, but servicing an instrument in space would be prohibitively expensive. This need towards maxing out the instrumental capabilities in the available volume and a high reliability is what sets apart a space observatory from the relative commodity that ground observatories posses and is where JEM-EUSO was visionary.

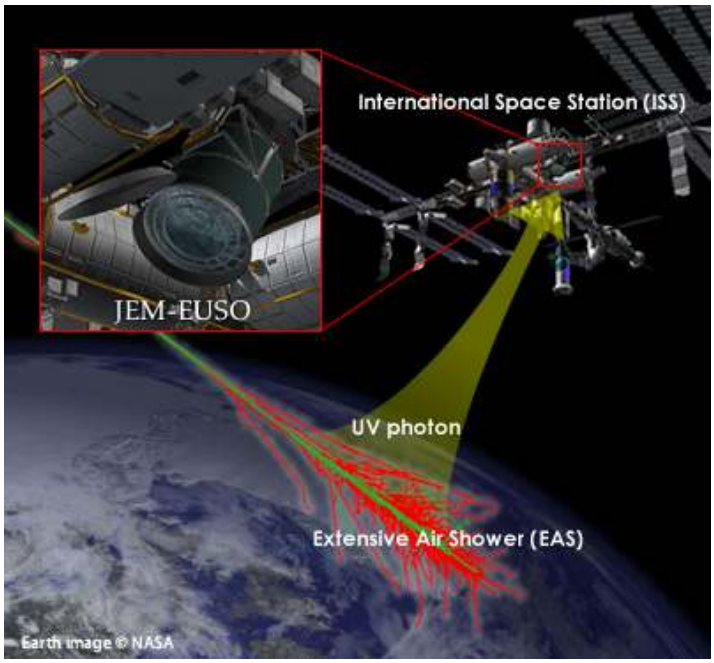

Figure 2.1: JEM-EUSO artist concept to observe UHECR induced EAS from the ISS.

2.1.1 Mission objectives

The JEM-EUSO telescope [46] was conceived as a space observatory dedicated to the study of UHECR with $E > 3 \times 10^{19}$ eV, the region of higher uncertainty in the cosmic ray spectrum. Figure 2.1 shows an artist concept of JEM-EUSO and table are shown in table 2.1 shows main parameters of the instrument. Through the development of the technology necessary for the observation of EAS from space, the instrument was envisioned to increase by an order of magnitude the existing annual exposure and perform observations to measure with unprecedented accuracy the primary energy, arrival direction and composition of UHECRs. The recorded data would allow to fulfill the primary objectives of the mission which are:

- Identification of the UHECR sources.
- Measurement of the energy spectra of individual sources.
- Measurement of the spectrum beyond the GZK limit.

Moreover the technical capabilities of the instrument would also allow it to be a probe for other exploratory objectives like constraining the galactic and extragalactic magnetic fields, the detection of UHE neutrinos, UHE gamma rays and heavy dark matter candidates. It is also suitable to perform spin-off science related to atmospheric phenomena like night-glow, transient luminous events, meteors, meteoroids and perhaps detect unexpected or unknown events.

Table 2.1: Parameters of the JEM-EUSO Instrument

Parameter	Value
Field of View	30°
Monitored Area	$>1.3^{1}05$ km^2
Telescope Aperture	$\geq$ 2.5 m
Operational Wavelength	300 - 400 nm
Angular Resolution	0.075°
Area of focal plane	4.5 m^2
Pixel size	$<$ 3 mm
Pixel number	$\approx 3 \times 10^5$
Pixel size on ground	$\approx$560 m
Time resolution	2.5 μs
Dead time	$<$3%
Detection efficiency	$\geq$20%

2.1.2 Observation Principle

At an altitude of about 400 km, JEM-EUSO would orbit the earth every $\approx$ 90 minutes and perform observations in the dark side of the earth for about 40 minutes per orbit. From this advantageous position and a FoV of $\pm 30°$ the telescope can observe an area of about 1.5×10^5 km^2 on earth's surface and measure the fluorescence UV light produced by the interaction of the UHECR with the atmosphere [46]. The left panel of figure 2.2 shows the observation principle of the telescope which detects the UV photons produced by fluorescence and Cherenkov radiation in the atmosphere. The former emission is isotropic and is detected directly whereas the latter is anisotropic and is detected through the back-scattered photons in the atmosphere and the reflected photons in the earth's surface or cloud tops. The photons that reach the telescope are focused by a refractive optical system composed of Fresnel lenses and detected by the focal surface detector. The optics and detector are described in sections 2.1.3 and 2.1.4.

To fulfill its scientific objectives the instrument is designed to operate in two observation modes. In the first one the telescope points at the nadir to perform the observations with an unprecedented annual exposure roughly equivalent to nine years of exposure of Pierre Auger [47]. Figure 2.3 shows the expected exposure of JEM-EUSO which takes into account the following factors: the ratio between the telescope's aperture covered by clouds and the total aperture; the operational duty cycle and the fraction of the telescope's geometric aperture that can't be used due to terrestrial or atmospheric light sources. Once the desired total exposure has been achieved the telescope will be operated in a second operation mode by tilting it from 20 to 40°. Tilting the telescope by 40° increases the observed area about six times but also raises the primary CR energy threshold necessary for detection. So this mode is intended to perform the study of the high energy part of the spectrum with very good statistics. The area covered by each operation mode is shown in figure 2.4.

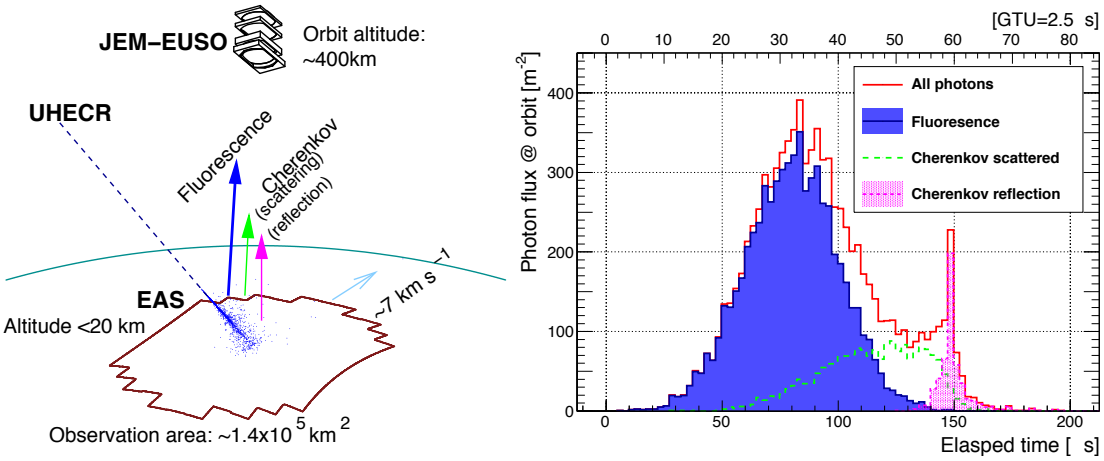

Figure 2.2: Observation principle of JEM-EUSO with an EAS in the FoV of the telescope. *Left:* The fluorescence emission of the EAS propagates through the atmosphere and arrives at the telescope, the scattered and reflected Cherenkov light arrives with a delay. *Right:* An EAS simulation showing the detected signal as a function of time. The fluorescence emission profile grows, achieves a maximum photon production and then decays. The last part of the signal is then dominated by the back-scattered Cherenkov photons and a reflected Cherenkov photon peak.

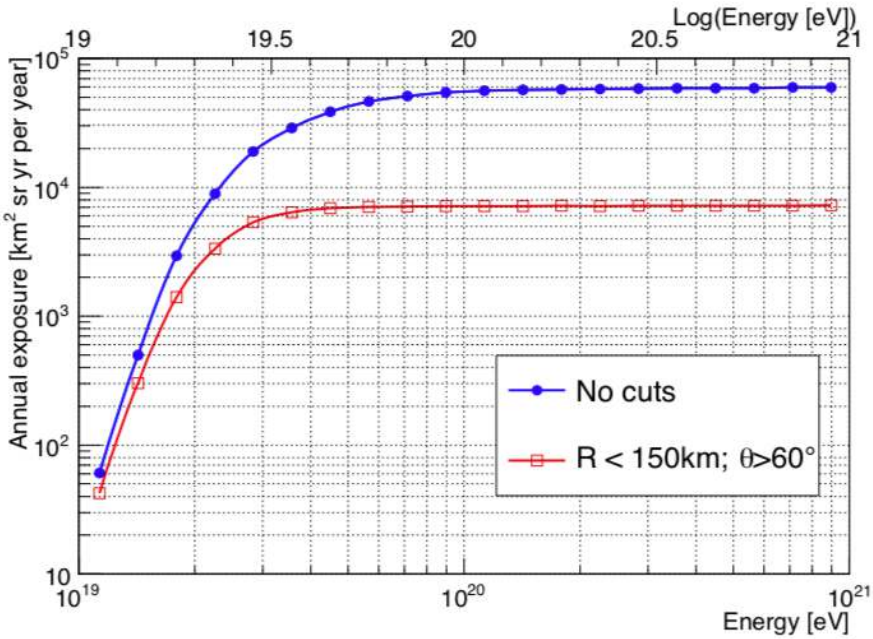

Figure 2.3: Expected annual exposure of JEM-EUSO as a function of energy. The blue line represents the whole FoV. Plot form [47]

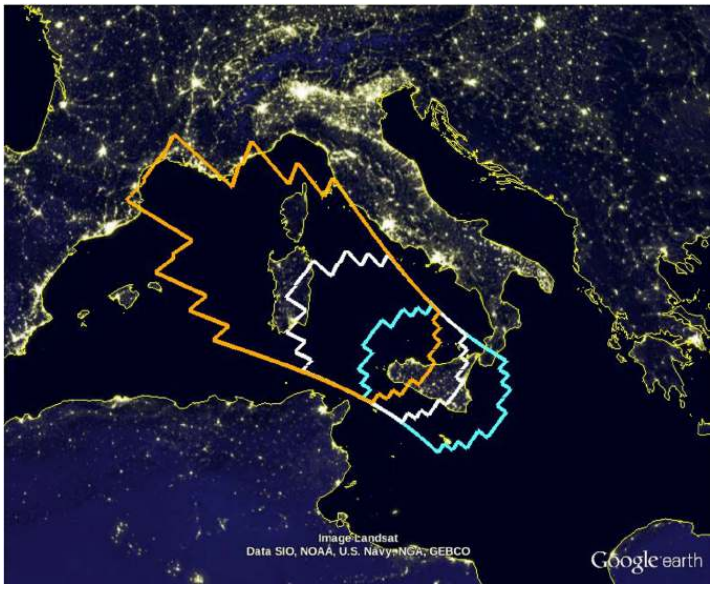

Figure 2.4: Footprints of the JEM-EUSO observation modes projected over Sicily where the concept of EUSO was developed. The smallest area corresponds to the nadir mode, the middle sized area to the telescope tilted 20° and the largest area to the telescope tilted 30°.

An EAS telescope is designed to operate in a continuous observation mode since EAS are rare events and their occurrence is unpredictable. Moreover, EAS develop in the atmosphere at the speed of so a temporal resolution in the order of a few microseconds is necessary to measure the EAS development and reconstruct its features. To achieve this task an ultrafast, highly pixelized detector consisting of photo-multipliers is developed for JEM-EUSO. The detector is capable of counting individual photons with a temporal resolution of 2.5 μs. This capability allows to track the development of EAS in the FoV, which looks like a luminous spot moving from pixel to pixel in each of the acquired frames. The right panel of figure 2.2 shows the luminosity of an EAS as a function of time. We can appreciate the development of the EAS which initially is dominated by fluorescence light, achieves a maximum photon production and then decays. The last part of the shower is then dominated by the backscattered Cherenkov photons and finally a peak of reflected photons.

Another technical hurdle in the detection of EAS is the vast amount of data processed due to the continuous observation. Most of the time the instrument looks at the night-sky background. Saving all the observed data is impractical due to storage and data rate limits. Just thinking about acquiring 400k images per second non-stop illustrates point. Therefore, a discrimination is necessary to reduce the amount of stored data and screen possible EAS candidates. This is achieved through the use of a rare event trigger. Indeed, the triggering technique was born in the context of cosmic ray research and thus is a fundamental tool for the detection of EAS. JEM-EUSO has envisioned a two level trigger hierarchy to reduce the event rate to a frequency that complies with the allowed data rate of the ISS. The JEM-EUSO trigger is described in sec. 2.1.6.

A last critical factor in the detection of EAS and accurate reconstruction of UHECR events are the atmospheric conditions in the FoV of the telescope. The variability in the presence and altitude of clouds affect the UV measurements, so to address this issue JEM-EUSO is provided with an Atmospheric Monitoring System (AMS) designed to support the observations of the main instrument [48]. The AMS is composed of an infrared (IR) camera and a LIDAR (LIght Detection and Ranging) instrument which work in conjunction to monitor the cloud coverage and cloud top height. The accurate determination of these factors will allow to correct the UV signal and reconstruct accurately the event. The AMS concept was tested with two infrared cameras which flew alongside with EUSO-Balloon and EUSO-SPB1

2.1.3 JEM-EUSO Optics

The observational requirements for EAS detection from space involve an important level of complexity as well as high performance for the telescope optics. Also to justify the development of a space-born EAS observatory, the exposure needs to be augmented by at least an order of magnitude compared to existing observatories. To account for this, the optics of the telescope have two main requirements:

- A large diameter to increase the number of photons collected. This lowers the minimum energy threshold for the detection of UHECRs.
- A large field of view (FoV) to increase the volume of atmosphere observed and consequently the number of events.

Moreover, the telescope has to be relatively compact to fit in the proposed location of the ISS and the H-II Transfer Vehicle (HTV). These requirements mean that the optical system needs to maximize the aperture size in the available space, provide a wide FoV coverage and have a fast focal ratio. e.g. a low ratio of the focal length with respect to the optics aperture diameter. These requirements can't be achieved with conventional astronomical optics. That's why the 36 m space telescope proposed by Linsley, although visionary, was ultimately unfeasible even by today's standards. A potential solution is the Schmidt camera design, which was studied for the OWL mission. However a design based on Fresnel optics based design was chosen for JEM-EUSO, based on the MASS proposition of Takahashi [44].

The conceptual design of the JEM-EUSO optics is shown in figure 2.5 [49]. From input to exit the optical system is composed of: a curved doubled sided Fresnel lens, an iris, a precision Fresnel lens, another curved doubled sided Fresnel lens and the focal surface detector, described in sec. 2.1.4. The precision lens is a hybrid lens with one Fresnel side and one diffractive side meant to correct the chromatic aberrations inherent to refractive systems and minimize the size of the multi-wavelength air fluorescence Point Spread Function (PSF). To fit within the HTV opening, the lenses were foreseen to be cut down in two sides, resulting

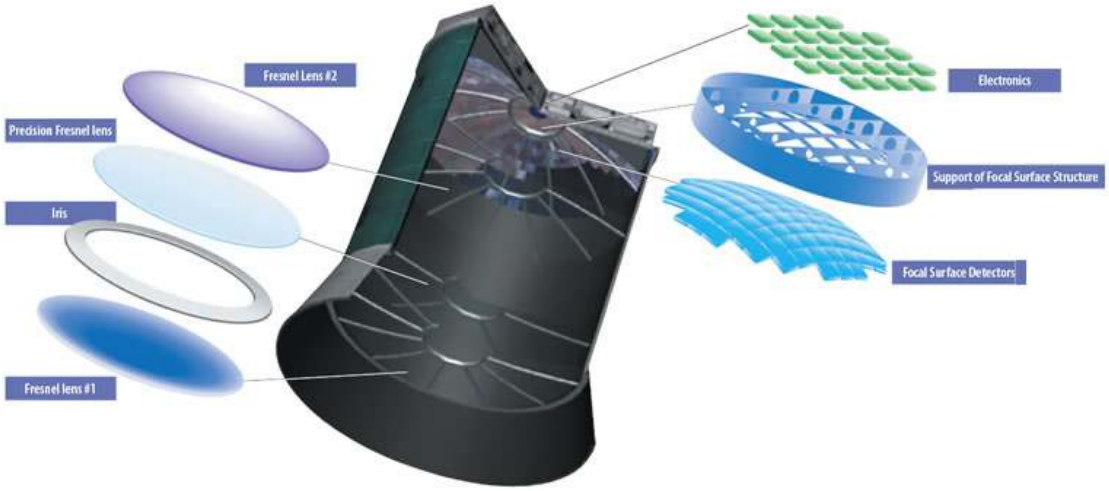

Figure 2.5: Optical system of the JEM-EUSO telescope

in a maximum diameter of 2.65 m and a minimum one of 1.9 m. These axes have a projected footprint on ground spanning about 500 and 300 km for an altitude of 400 km.

Two main materials were studied for the JEM-EUSO optics: CYTOP (by Asahi Glass Co. LTD) and UV grade PMMA-000 (Polymethyl Methacrylate, by Mitsubishi Rayon Co. LTD) more commonly known as Plexiglas CYTOP offered slightly better properties than PMMA, it has more UV transmittance (about 95%) and it's refractive index is lower than PMMA so it provides less dispersion. However, CYTOP is a harder material, making it more difficult to fabricate the lenses; it is also more expensive. Ultimately, only a 1.5 m diameter prototype of the JEM-EUSO optics was built using PMMA. Also, three smaller prototypes were built to test the optics principle: One system consisting of two single sided lenses for the EUSO-TA pathfinder (see see sec. 2.2.3) and two triple lens systems consisting of two single sided refractive lenses and one single sided diffractive lens for the EUSO-Balloon (sec. 2.2.1) and EUSO-SPB1 (sec. 2.2.2) pathfinders. In the three lens system the refractive lenses were placed at the both ends of the optics and the refractive lens in the middle, similar to JEM-EUSO. However, due to performance issues with the diffractive lenses, both balloon pathfinders flew in a configuration akin to EUSO-TA.

2.1.4 JEM-EUSO detector

The detector of JEM-EUSO is an ultrafast camera capable of taking data every 2.5 μs interval called gate time unit (GTU). The detector's design departs from the traditional fluorescence cameras used in ground observatories. The typical construction of fluorescence (or Cherenkov) cameras consists of an array of photo-multipliers tubes (PMT) mechanically coupled to a light-guide, typically a hexagonal Winston cone [50]. This gives the detector an hexagonal pixel

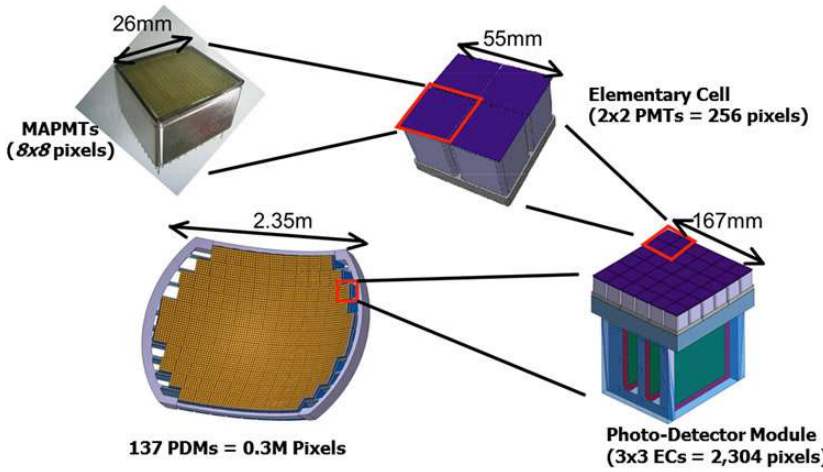

Figure 2.6: Photodetector of JEM-EUSO. The minimal unit is a single MAPMT. 4 MAPMTs grouped together (2×2) forms an Elementary Cell, the base readout unit. 9 Elementary cells (3×3) form the Photodetector Module and 137 PDMs form the JEM-EUSO fluorescence detector.

geometry resembling a honeycomb structure. The requirements of a space mission make this type of construction unfeasible: first because the large pixel size of PMTs ($\approx$ 5cm diameter) plus the light-guide limits the maximum number of pixels that fit in the allocated volume. Second because a large pixel would result in a coarse angular resolution from the altitude of the ISS ($\approx$ 400km). This propels the necessity towards miniaturization of the detector to have a higher pixel density and finer angular resolution. The technology employed in JEM-EUSO's camera is that of Multi-anode photo-multipliers (MAMPT) also known as position sensitive photo-multipliers These devices accommodate multiple photo-multiplication chains in a single compact device, achieving a pixel side length of about 3 mm. This offers a great advantage since the pixel size is decreased and the pixel density increased, making it ideal for a space based fluorescence detector. This is the base for the Focal Surface (FS) detector of JEM-EUSO.

The FS detector is located in the focal spot of the optics, it is about 2.5 m in diameter and has a spherically curved shape. It is composed by 4932 MAPMTs and is divided into sub-modules to facilitate readout and integration. The minimum unit in the FS is a single MAPMT which has 64 pixels (8×8). Four MAPMTs grouped together (2×2) form the elementary cell (EC), the base module for readout. Nine ECs (3×3) form the photo-detector module (PDM), which can work as a standalone detector and is used for most of the EUSO pathfinders. The complete FS consists of 137 PDMs, giving a total of 315,648 pixels. The focal surface and its submodules are shown in figure 2.6.

The development of the JEM-EUSO MAPMTs is a collaborative effort between RIKEN and Hamamatsu [46], a company well known in the photomultiplier field. The MAPMTs have a UV-glass window and an ultra-bialkali (K–Sb–Cs) photocathode which has a quantum efficiency of about 35%. The device is composed of a 12 stage metal channel dynode structure,

allowing gains in the order of 10^6. The rise time of the anode is about 1 ns with a spread of 0.3 ns. The pixels have a crosstalk of less than 1%. For observation purposes, a UV filter screen (Schott BG3) is placed on top of each MAPMT. The BG3 filter allows the transmission of the main air fluorescence emission lines (300-400 nm) but also has a transmission window in the Infra-Red (IR) region. The detector is not sensitive to IR wavelengths

2.1.4.1 High Voltage

MAPMTs have to be polarized with high voltage to achieve the potential difference between each dynode necessary for the secondary electron multiplication. The JEM-EUSO detector is powered by a High Voltage Power Supply (HVPS) system which consists of nine Cockcroft-Walton voltage multipliers and a control board [51]. Each Cockcroft-Walton multiplier powers the detector at the EC level, providing a high DC voltage for the cathode and dynodes of the 4 MAPMTs. At the PDM level the nine voltage multipliers are controlled by a single board which provides insulation between the HVPS system and the rest of the instrument and communication between the nine voltage multipliers, the house-keeping unit and the PDM board.

2.1.4.2 Data readout

Each of the 36 MAPMTs of each PDM is individually read by an ASIC (Application Specific Integrated Circuit) developed for JEM-EUSO named SPACIROC1 (Spatial Photomultiplier Array Counting and Integrating ReadOut Chip) [52]. This chip reads the 64 channels of the MAPMTs and performs single photon counting with a 30 ns double pulse separation. i.e. the minimum time resolution required to discriminate two separate photo-electron pulses. In case of saturation beyond single photon counting capabilities due to more luminous atmospheric phenomena, then SPACIROC is capable of charge-to-time (Q-to-T) conversion. The chip was further updated, with the 2nd generation SPACIROC2 [53] and later by SPACIROC3 [54].

The signal coming from all the MAPMTs of the PDM is read by the PDM board [55]. The electronics of the board are based on a Virtex-6 FPGA (Field Programmable Gate Array). Every μs of data coming from the ECs are sent to the PDM board and stored in a 320 mus (128 GTU) circular memory buffer. The first level trigger (FLT) of JEM-EUSO is implemented in the FPGA logic and is continually executed on the data (see sec. 2.1.6.1 for an explanation on the FLT). The data from eight PDM boards is then fed to one of the 21 foreseen cluster control boards (CCB) which are part of the Data Processor (DP) sub-system.

2.1.5 Data Processor

The DP [56] is core of the digital electronics of the instrument. Its tasks consist in controlling the front-end electronics, perform the second level triggering, tag the arrival time (UTC) and payload position (GPS) of detected events, manage the mass memory, measure live time of the instrument, provide signals for time synchronization of events, perform housekeeping monitoring and handling of the interface to tele-commands and telemetry systems. In total the DP is formed by the following sub-assemblies:

- Cluster Control Board
- CPU
- Data storage
- House keeping system
- Clock board (Clk-board)

The CCB [57] is the interface between the PDM board and the rest of the DP assembly and the location of the second level trigger (SLT) logic. If an FLT is issued then the data of the circular memory buffers from 8 PDMs is passed to the CCB and the SLT algorithm is executed (see sec. 2.1.6.1 for an explanation on the SLT). The SLT is implemented on a Virtex-4 FX-140 FPGA and is executed in parallel on each PDM, regardless of the geometrical disposition of the PDMs connected to the respective CCB. If the SLT is issued then the data acquisition is stopped and the data from relevant PDMs is sent to the on-board CPU system via the SpaceWire protocol. In total, 21 CCBs were planned for JEM-EUSO but only one was necessary for each of the JEM-EUSO pathfinders.

2.1.6 JEM-EUSO Trigger

The phenomena studied in high energy physics experiments are rare and occur at time periods well beyond human perception limits, so we rely on instruments to observe and process the data. Due to real world limitations like data rates and storage capacity, only a small fraction of the data processed on a detector can be recorded. This imposes a tight real-time discrimination criteria to filter out which events to keep, this is the job of the trigger. Multi-level trigger hierarchies are common, they typically include lower level triggers to filter events based on simple criteria and forward the data to higher level triggers which have more time for processing and selecting suitable candidate events.

The total data rate processed by the JEM-EUSO electronics in one second of operation is: 315648 px $\text{FS}^{-1} \times 4 \times 10^5$ GTU $\times$ 8 bit $\text{px}^{-1} \approx 1$ Tbs. However, the telemetry budget allocated for JEM-EUSO is 300 kbs. So a data reduction in the order of 3×10^6 has to be

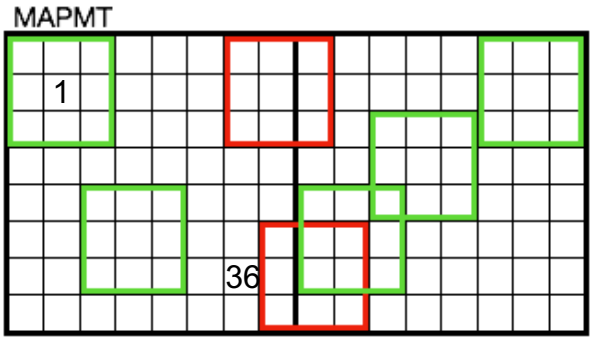

Figure 2.7: First level trigger cells. The cells are 9×9 pixels in size and cannot be shared by adjacent MAPMTs, so each MAPMT can host a total of 36 cells. Green squares indicate valid cells and red squares invalid cells.

performed on real time by the electronics to satisfy the telemetry constraints [58]. To achieve the observational goals of JEM-EUSO a two level trigger hierarchy was designed, each of the levels is described next.

2.1.6.1 First Level Trigger

The JEM-EUSO FLT [58] operates at the EC level. It's aim is to reduce the fake trigger rate to about 1 Hz/EC. Fake triggers are caused by fluctuations of the night-sky luminosity and by luminous sources like artificial lights, lightning, meteors and aurorae. The FLT rejects most of the UV luminosity fluctuations by requiring a locally persistent signal lasting a few GTUs. The persistence requirement depends on the instrument where the FLT is implemented as it can be adapted to the different pathfinders in the JEM-EUSO framework.

The FLT works by monitoring the persistence signal in groups of 3×3 pixel cells. These cells cannot overlap adjacent MAPMTs, so one MAPMT can only have 36 cells, centered in the internal 6×6 pixels (see figure 2.7). The FLT has four main parameters: *R, P, N* and *S*. It tracks if for an R number of GTUs in a range of P consecutive GTUs, at least one cell has a number of counts equal or higher than a threshold value N and if the integrated counts in the cell are equal or higher than a value S. If these conditions are fulfilled, then a trigger is issued. Next, starting from the GTU were the trigger was issued a confirmation counter is activated for a preset N_{GTU} number of GTUs. This counter is increased by one for each GTU where another trigger is issued. If the accumulated value is below N_{GTU}, the trigger is validated and the FLT passes the time and location information of the triggered cells to the SLT. If the confirmation counter value exceeds a threshold N_{gtu}^{thr} in the N_{GTU} window, then the trigger is rejected. This means that the FLT was activated for a duration longer than the expected duration of an EAS, about 45 GTU in one EC. This allows to reject the signals of longer duration events such as lightning, transient luminous events and meteors as well as relatively static sources such as airplanes and cities.

The P and R parameters are defined at the beginning of an observational run. They depend on the distance between the EAS and the instrument and can be modified depending on the instrument performing the observations. The current values for JEM-EUSO are P=4 and R=2. The threshold parameters N and S are changed dynamically every 128 GTU (1 data packet), their value is set according to the average UV background level in the MAPMTs. To account for a non-homogeneous background in the FoV of the telescope, the ECs are subdivided in 2×8 pixel groups, totaling 32 subgroups per EC. Every 128 GTU the average counts per subgroup is computed and the highest value is assigned as the threshold for the whole EC. The persistence values for EAS identification are $N_{GTU} = 73$ and $N_{gtu}^{thr} = 72$ but can also vary. The preset values are determined through Monte Carlo EAS simulations and the performance is studied through simulations and experimental data [59].

2.1.6.2 Second Level Trigger

In the JEM-EUSO detector, a true EAS signal should look as a light spot traversing the pixels during continuous GTUs. The light spot would remain static only in the rare case where shower develops along the line of sight of a group of pixels. The FLT is concerned with selecting localized pixel excesses for a given amount of consecutive GTUs, but it disregards the location and geometrical development of the signal. If a FLT is activated then it passes the GTU and location of the triggered cells (called the trigger seed") to the SLT. The job of the SLT [57] is thus to track the movement of this light spot for a preset time by integrating possible geometrical combinations for the EAS track development direction and discriminate the integrated pattern from the background.

The trigger starts by defining a box centered at the trigger seed. The box integrates photon count values by moving in a 3D space consisting of two spatial dimensions (x and y pixels) and one time dimension (GTUs). The integration is performed over ± 7 GTU in a predefined set of directions defined by two angular parameters: θ and ϕ. The angle θ is the zenith angle (where $\theta = 0$ would correspond to the nadir of JEM-EUSO) and ϕ is the azimuth angle of the EAS (where $\phi = 0$ corresponds to the velocity vector of JEM-EUSO). For clarity, the principle and parameters of the SLT are depicted in Figure 2.8. The left panel shows as an example, a 3×3 light spot moving in the 3D space consisting of an EC plane and 4 GTUs. The angle θ and it's value range of 0 to 90° are depicted on the top EC frame. The right panel shows the integrated frames where the event is now a linear track. The angle ϕ and it's range of 0 to 360° is shown centered at the trigger seed. If the combination of θ and ϕ parameters matches (or approaches the best) the direction of the EAS, then the integrated value will be maximized. Then, if this value exceeds a threshold above the background a SLT will be issued. Due to constraints with the on-board computing resources, power, weight, size and space qualification requirements of the hardware. Currently, a total of 375 points are foreseen for the integration which are equally distributed in space and time. A minimum set of directions containing 67 combinations of θ and ϕ were selected and evaluated with simulations, aiming to meet the aforementioned constraints.

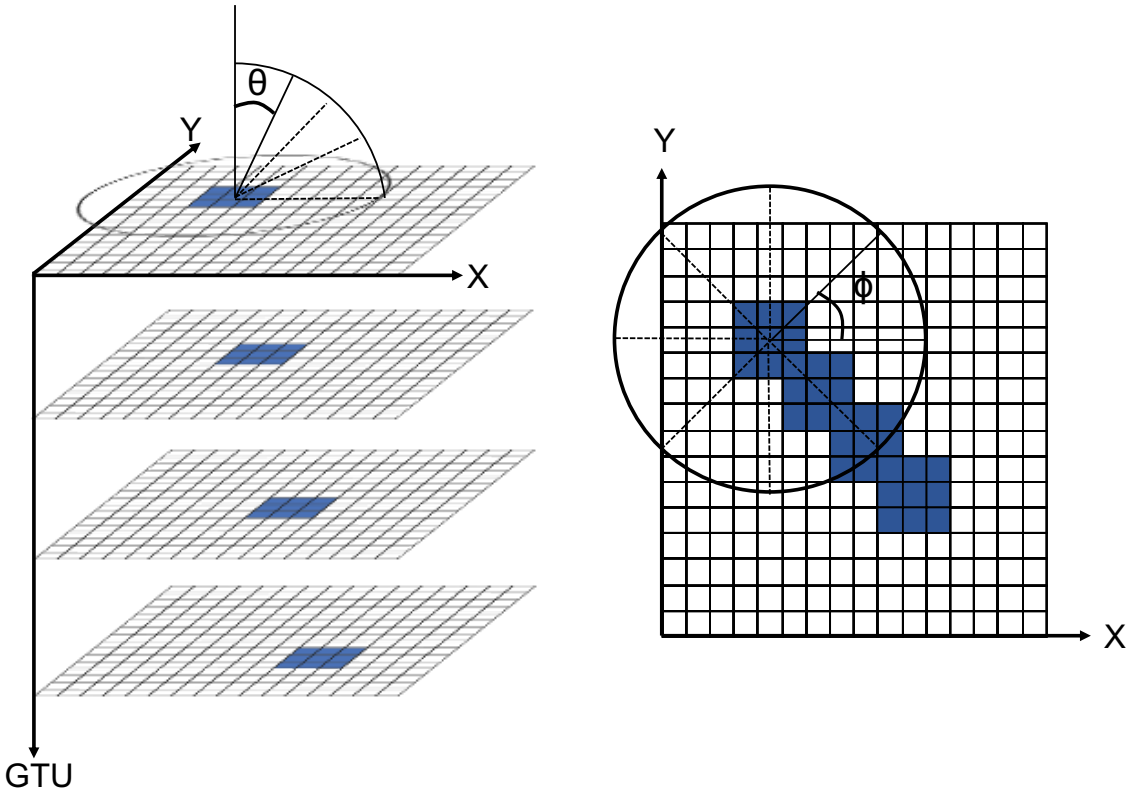

Figure 2.8: Principle of the Second Level Trigger. A box integrates the photon count values in a 3D space of X and Y pixels and GTU frames. If the correct combination of zenith angle θ (left) and azimuth angle ϕ (right) is used to define the direction of integration, then the integrated value will reach a maximum. If the value exceeds a predefined threshold above background then a second level trigger will be issued.

2.2 JEM-EUSO Pathfinders

An important step in the implementation space missions that use novel technology, is the demonstration and validation of it's technology and principles prior to the debut of the main mission. The reason is clear, it would be an extreme waste of resources putting in orbit an instrument that does not perform as expected. Therefore, the rigorous testing of prototypes is a requirement to asses the TRL of a proposed instrument. In an ideal case, this can be demonstrated on ground. In rare cases, the principle of satellite missions is validated through satellite pathfinders. However, this is an expensive approach and is reserved only for cases with the highest potential (and funding) or through multi-experiment satellite payloads. A viable and cheaper alternative is the use of stratospheric balloons to test the prototype technology and principles in a suborbital space. Many high energy astronomy experiments use the latter approach and JEM-EUSO is no exception.

The JEM-EUSO collaboration has developed multiple pathfinders to demonstrate its technology. These demonstrators include a ground based observatory which is good to test the technology, but to fully validate the observational principles the use of stratospheric balloons is necessary. This is kind of nice since the field of cosmic rays started with a balloon flight and now we find ourselves recurring again to balloons to attempt a more ambitious type of observation. In total JEM-EUSO has two tested balloon pathfinders with a third in preparation plus others which we will review.

2.2.1 EUSO-Balloon

EUSO-Balloon [60] is the first pathfinder mission developed by the JEM-EUSO collaboration and also the first to take data and perform obsevations from above. The mission was proposed in 2011 by three french laboratories (APC, IRAP and LAL) to the French space agency "CNES" (Centre National d'Etudes Spatiales[2]). Following the acceptance of EUSO-Balloon, it went through a fast development cycle of only three years which culminated in its maiden flight in 2014. This was possible thanks to the joint effort of many JEM-EUSO member institutions which were in charge of developing different aspects of the instrument. The institutions responsible for the development of the various subsystems of EUSO-Balloon are listed in 2.2 and the instrument is shown in 2.9.

Like the JEM-EUSO instrument, EUSO-Balloon is also a nadir pointing UV telescope. It is an experimental mission designed to test the proof of principle for observing EAS from space. The primary objectives of the mission are threefold:

1. Test and validate the key technologies and methods needed to observe EAS "from above".
2. Acquire data to perform a UV background study of night time earth.

[2]National Center of Space Studies

Table 2.2: Responsible institutions for the procurement and delivery of the different subsystems of the EUSO-Balloon instrument and the Helicopter under-flight during the Timmins flight. Table from [60]

System	**Sub-assembly**	**Institution**	**Country**
Telescope	Fresnel Lenses	RIKEN	Japan
	Lens fitting	IRAP	France
	Structure / Gondola	IRAP	France
Photo Detector Module	Multi-Anode photomultipliers	RIKEN	Japan
	ASIC	LAL	France
	Elementary Cell	LAL, KIT	France, Germany
	HV power supply and switches	NCBJ, APC	Poland, France
	PDM board	EWHA	South Korea
	PDM low power supply	UNAM	Mexico
	PDM Structure	INFN Frascati	Italy
Data Processor	Main processing unit	INFN Napoli	Italy
	Data Storage	INFN Napoli	Italy
	Clock Generator	INFN Napoli	Italy
	Trigger software	INFN Torino	Italy
Digital	CCB Data Processor	IAAT	Germany
	House keeping board	UNAM	Mexico
	Low voltage power supply	UNAM	Mexico
Battery Pack	Batteries and Controller	UAH, IRAP	Spain, France
IR-CAM	Infrared camera	UAH	Spain
Helicopter Underflight	UV-Laser, LED and Xenon Flashers	UHA, CSM	United States
Integrated system	All integration and test	IRAP	France

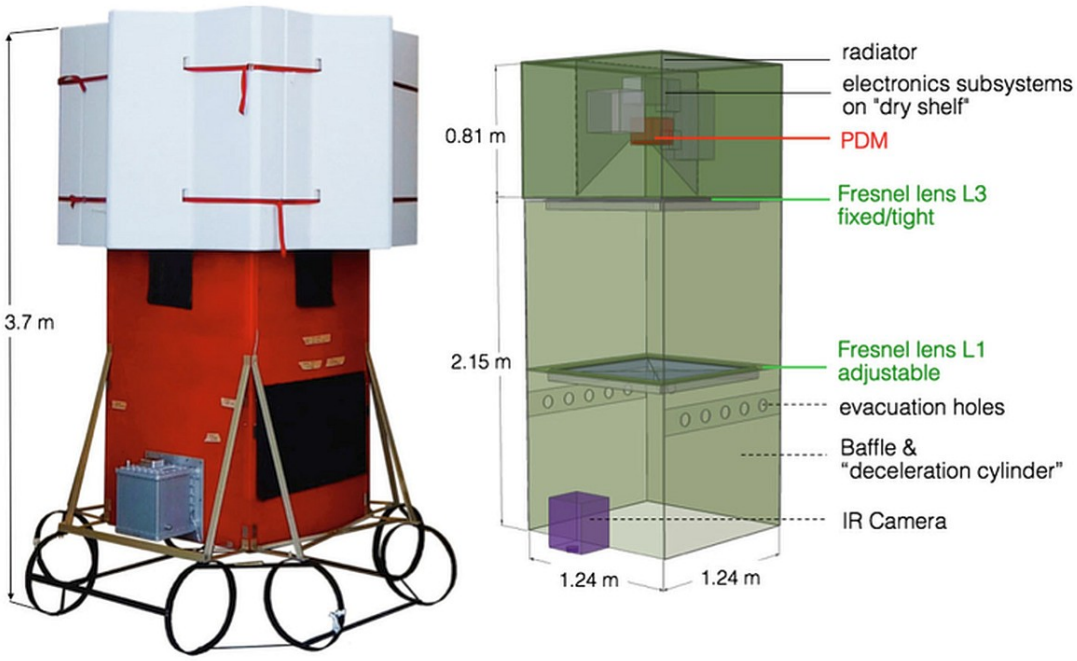

Figure 2.9: EUSO-Balloon Instrument. *Left*: Instrument ready for flight. *Right*: Schematic view of the instrument showing the components. The lower red box holds the Fresnel lenses of the telescope.

3. Be a pioneering mission for JEM-EUSO

The instrument was launched on the 25th of August, 2014 from the stratospheric balloon base in Timmins, Canada by CNES. During its 8 hour flight, the balloon operated an entire astronomical night from an altitude of ≈38 km flying over forest and inhabited areas before splashing down in a small lake. Following data analysis a multitude of results were published: EUSO-Balloon observed a variety of UV-light sources from ground successfully producing data to demonstrate it's UV imaging capabilities [61] and it detected UV laser tracks in the atmosphere during a helicopter under-flight [62]. The success of the mission opened the door for future pathfinder projects in the JEM-EUSO framework, with EUSO-SPB1 being the next in line.

Although the EUSO-Balloon mission was a success, one of the unresolved issues from the instrument is the incomplete understanding of the optics performance. The optics of EUSO-Balloon are a smaller and simpler version of the JEM-EUSO optics. The baseline design consists of two refractive Fresnel lenses and one diffractive lens. However, due to issues with the diffractive lens, only the two refractive lenses were used for flight. Results from the characterization campaign showed that the numerical simulations were not in agreement for either (two or three lens) configuration. The optics were simulated using a variety of tools

including an internally developed ray tracing software and the industrial software CODE V® and ZEMAX®. This issue is one of the core problems of this thesis and is treated in chapter 3 which also includes a detailed description of the optical system.

The detector of EUSO-Balloon is a first generation JEM-EUSO PDM, the flight provided the first opportunity to demonstrate it's capabilities by observing and taking data from above. The flight allowed to validate the performance of the PDM and associated electronics in a suborbital environment. The EC readout was performed by the SPACIROC1 ASIC which gave the instrument a double pulse resolution of 30 ns (sec. 2.1.4.2). The HVPS was also tested with positive results (sec. 2.1.4.1).

Due to the time constraints set by the balloon launch deadline, the FLT was not fully implemented in FPGA logic the PDM board. Instead the instrument flew with an artificial trigger which fired with a 20 Hz rate. This was not a problem, since the goals of the mission were not to detect EAS but to test the capabilities of the instrument by measuring the UV night sky and scattered light from laser shots. Detecting an EAS would have been be a plus, however the chances of the trigger coinciding with one are low and the data analysis didn't show any indication of this. Nevertheless, the data gathered by EUSO-Balloon was used to test the FLT offline, yielding positive results by detecting the UV laser shots in the atmosphere [63]. The SLT is also not available in EUSO-Balloon.

Aside from the optics and detector, EUSO-Balloon also provided the opportunity to test the design and functionality of almost all the sub-systems envisioned for JEM-EUSO. This includes the data processor, an IR camera for cloud monitoring and the waterproof gondola. A detailed instrumental description of the instrument is provided in [60].

2.2.2 EUSO-SPB1

EUSO-SPB1 (Super Pressure Balloon) is the second balloon pathfinder of the JEM-EUSO collaboration. The mission was selected as a NASA's mission of opportunity[3], it was developed using most of the EUSO-Balloon components and was ready for flight in the first quarter of 2017. The optics characterization, the balloon launch campaign activities and the flight data analysis are an important part of this work and are discussed respectively in chapters 3, 4, and 5. In this section we'll describe the main characteristics of the instrument and it's objectives.

EUSO-SPB1 built up on the technical success gained from the flight of EUSO-Balloon, it featured several technical improvements in the detector and electronics and had more ambitious scientific goals, which were:

- Perform the first observations of ultra high energy cosmic ray air showers by looking at the atmosphere from suborbital space with an air fluorescence detector.

[3] A mission of opportunity is a Non NASA sponsored mission, with a cost for NASA of less than 55 million USD.

- Measure the Earth's UV night emission over ocean and clouds.
- Search for fast UV signatures from other objects / events.

The optics of EUSO-SPB1 share a similar design to the optics of EUSO-Balloon and EUSO-TA. Therefore, the description of the EUSO-Balloon optics (sec. 3.3) also applies for EUSO-SPB1. Like EUSO-Balloon, the optics was tested with three and two lenses, but the performance results favored the two lens configuration. The detector of EUSO-SPB1 is a second generation JEM-EUSO PDM. The version used for this mission featured several improvements over its predecessor. The improvements include a better insulated design of the HVPS PDM board [51], a double pulse resolution of 10 ns and a fully implemented FLT on the PDM board.

The FLT envisioned for JEM-EUSO was tested online for the first time in the EUSO-SPB1 flight. For the operational balloon flying altitude of about 33 km the trigger parameters P and R with values of either 0 or 1 are good. Indeed, during flight the trigger was tested with P=0, R=0 and P=1, R=1 parameters and additionally with the JEM-EUSO optimized values of P=4, R=2. Since EUSO-SPB1 uses only one PDM and flies at a much lower altitude compared to JEM-EUSO, an EAS would cross the FoV in just a few GTUs, so the FLT confirmation counter is not necessary. This means, that a P=0, R=0 configuration will validate a trigger as soon as the first threshold excess is detected, whereas a P=1, R=1 configuration would need two consecutive threshold excesses to validate a trigger condition. The SLT, despite being implemented in the CCB, was not used for the flight. The FLT performance is reviewed in the context of the data analysis in sec. 5.2.3. A detailed review of the FLT performance is given in [64] and [65].

2.2.2.1 Ancillary instruments of EUSO-SPB1

University of Chicago Infra-red Camera (UCIRC)

The University of Chicago Infra-red camera (UCIRC) [66] is an ancillary instrument designed to acquire Infra-Red (IR) images to monitor the cloud cover in the FoV of the telescope and determine the cloud top height (CTH). Cloud monitoring is an important task, since the cloud cover impacts the observation of UHECRs: it introduces noise, uncertainties and affects the duty cycle of the detector (but would help to detect reflected Cherenkov light). Therefore, detailed knowledge of the atmospheric conditions in the FoV of the telescope and determination of the CTH are essential to correct for the uncertainties introduced by the presence of clouds and to accurately reconstruct EAS.

UCIRC consists of two IR cameras with a spectral sensitivity of 7.5 to 13.5 μm wavelength. The cameras have a FoV of 32 $\times$ 24°and each one is coupled with a bandpass filter centered at 10 μm and 12 μm. The use of two IR spectral bands is motivated by a CTH reconstruction

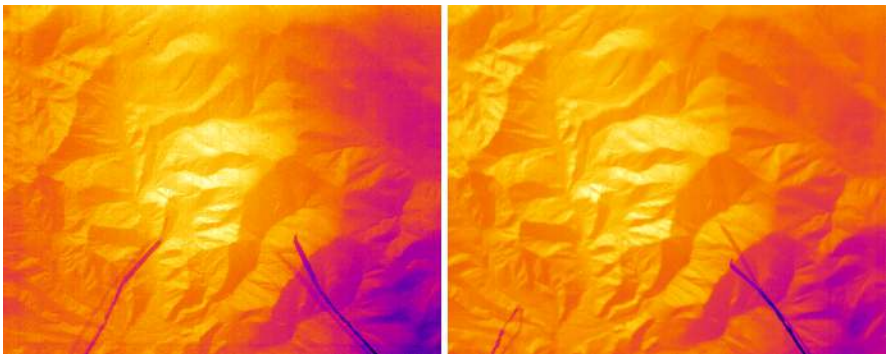

Figure 2.10: Two IR images taken by UCIRC centered at the 12 μm (Left) and 10 μm (right) bands. The images show the southern alps in the south island of New Zealand. Picture from [66]

technique called the radiative method [67]. In this method the brightness temperature (BT) of the cloud, i.e. the radiation detected by the IR camera, is used to determine the cloud top temperature (CTT) through the use of bi-spectral reconstruction algorithms. Once the CTT is determined the CTH can be estimated using vertical temperature profiles.

UCIRC was designed to operate between 0 and 33 km above sea level. To maintain the instrument operable in the harsh night-day temperature variations, it was equipped with an active temperature management system. The instrument performed well during the initial phases of the balloon flight however issues with the temperature system rendered the instrument unusable for long periods of time. Furthermore, during periods where the instrument was functional, data acquisition issues prevented it from taking data continuously, creating gaps in time for the IR images. Ultimately, UCIRC was only able to take less than a hundred pictures, an example is shown in figure 2.10.

Silicon photomultiplier Elementary Cell Add-on camera (SiECA)

Silicon Photo-multipliers (SiPM) are compact solid state photosensitive devices which offer gains similar to PMTs ($\approx 10^6$) along with several advantages: lower power consumption, higher quantum efficiency, higher sturdiness and resistance to magnetic fields. However, they have also have a higher noise rate and temperature dependence. SiECA [68] is an experimental silicon SiPM detector conceived with the objective of evaluating the SiPM technology on a non-terrestrial fluorescence telescope. This is motivated by the development of prototype terrestrial detectors using SiPM technology which might potentially replace PMTs. Examples include the AMIGA [69] and FAMOUS [70] instruments of the Pierre Auger observatory, and the upgraded IceTop scintillators of IceCube [71].

The SiECA detector, shown in figure 2.11, is composed by an EC board with four Hamamatsu (S13361-3050AS-08) SiPMs of 8×8 channels each. The SiPMs are covered by a BG3 filter. There are four temperature sensors placed at the junction of the four devices. Fur-

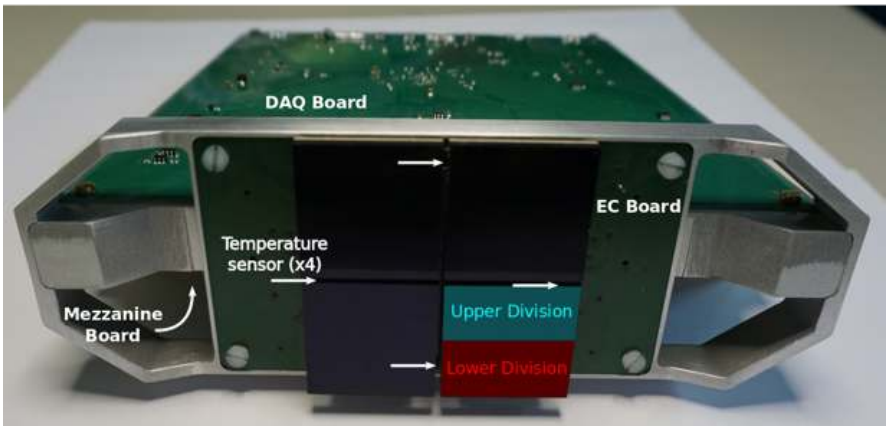

Figure 2.11: The SiECA detector. Picture from [68]

thermore, each SiPM is partitioned into an upper and lower division of 8×4 pixels for power supply and readout purposes. The readout is performed by a Data Acquisition and "Mezzanine" boards which houses eight ASICs, eight bias voltage generators, an FPGA and other electronics. The instrument is powered by a dedicated 5 V, 2 A power supply which provides the necessary voltage for the camera and front end electronics. The design of SiECA allowed it to be mounted adjacent to the EUSO-SPB1 PDM and to be evaluated during flight. However, electrical interference problems observed during flight, most likely caused by SiECA, affected the stability of the PDM and resulted in switching off this ancillary detector to prioritize the performance of the PDM.

2.2.3 EUSO-TA

EUSO-TA (Telescope Array) [72] is a ground based EUSO telescope located in the TA site in Black Rock Mesa, Utah. It is the second operational JEM-EUSO pathfinder and the first to perform observations of EAS from ground. The instrument is composed of two refractive Fresnel lenses and one PDM with it's associated electronics. EUSO-TA shares an optical system identical to that of it's balloon-borne counterparts. The telescope structure is held on a stand with an adjustable elevation angle between 0°and 30°and is housed in a container just in front of one of the Telescope Array Fluorescence Detector (TAFD). Figure 2.12 shows the instrument along with EUSO-SPB1 during a test campaign performed in Utah, USA.

EUSO-TA's main objective is to test the capabilities of the JEM-EUSO technology and evaluate it's performance. Five observation campaigns were performed between 2015 and 2016 where the instrument was tested in multiple scenarios. The instrument has been able to observe 9 EAS thanks to the TAFD external trigger, allowing coincident detections in the overlapping portions of their FoV. The JEM-EUSO FLT has been also tested with the aid of laser shots mimicking EAS. It has been able to measure the night sky UV emission and is capable of detecting stars, proving the capability to image point sources. Although the

Figure 2.12: The EUSO-TA and EUSO-SPB1 instruments in front of the Telescope Array Fluorescence detector. Picture by M. Mustafa.

instrument is tuned for detection of fast events with a temporal resolution of 2.5μs it is also capable of detecting slow events like meteorites and airplanes traversing the FoV. Overall, EUSO-TA is a very valuable test-bench, necessary to validate the techniques required for the success of other EUSO pathfinders.

2.2.4 Mini-EUSO

Mini-EUSO [73] is the smallest instrument in the EUSO family of UV telescopes. It is composed of three main units: a JEM-EUSO PDM, a 25 cm diameter Fresnel lens based optical system and the data acquisition system. Additionally, Mini-EUSO has two ancillary cameras, one for near IR (1500 to 1600 nm) and one for visible wavelengths (400 to 780 nm) to provide atmospheric monitoring and complement the UV luminosity measurements. The optics is composed of two double sided Fresnel lenses with a field of view of 44°. Mini-EUSO was launched August 22 at 3:38 UTC from the Baikonur cosmodrome and docked to the ISS on August 27. The instrument had it's first light on October 7, 2019 at 18:46 UTC. The instrument is shown in figure 2.13

The goal of Mini-EUSO is to study the UV luminosity of the night time earth by performing high resolution mapping of the UV emissions in the 300-400 nm band. Thanks to it's temporal resolution and multiple triggers Mini-EUSO will also be able to detect other atmospheric events such as transient luminous events, including: blue jets, sprites and elves. These phenomena are bright in the UV and will be necessary to characterize to avoid interference with UHECR signals. It will also be able to observe slower events like meteors, fireballs as well as searching for strange quark matter. These events will be detected mostly by the use

Figure 2.13: Flight model of Mini-EUSO. Picture by P. Klimov

of offline triggers on-ground. An exploratory objective of the mission is the detection of space debris. With it's high speed imaging and large field of view it will be used as a prototype to detect debris during the twilight period of the orbit, in which the debris will be illuminated by the sun.

Mini-EUSO is not designed to observe UHECR due to the small size of the optical system. However, technically it can observe CRs above an energy threshold of 10^{21} eV, which is unlikely due to the suppression of the spectrum predicted by the GZK effect. The observations will likely provide a null detection upper limit considering Mini-EUSO's exposure of about 15000 km^2 sr year assuming a 20% duty cycle. It will validate the JEM-EUSO observation technique by using Fresnel optics downscaled to a single observation module and will augment the TRL of the JEM-EUSO instrumentation.

2.3 Future projects in the JEM-EUSO framework

2.3.1 EUSO-SPB2

EUSO-SPB2 is the second EUSO telescope to be flown on NASA's super pressure balloon [74]. It expands the scientific objectives of JEM-EUSO and will observe the southern hemisphere night sky. The objectives of EUSO-SPB1 are threefold:

- Detect Cherenkov light from EAS from near space;

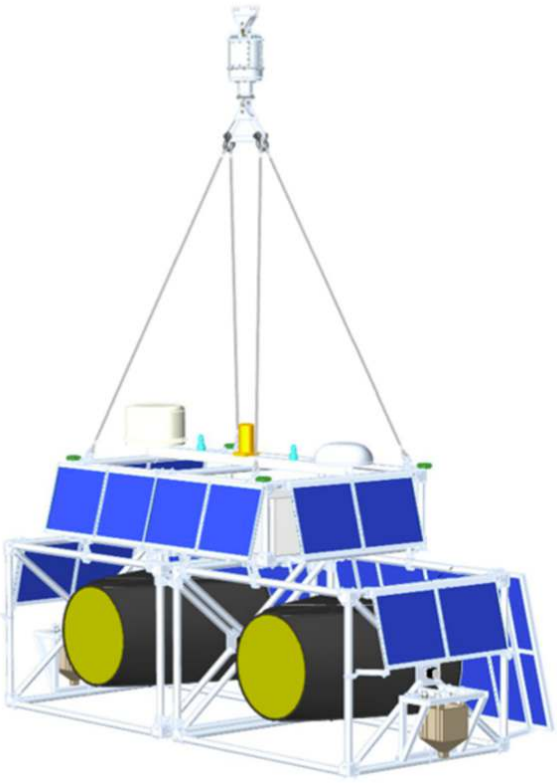

Figure 2.14: Concept drawing of EUSO-SPB2 integrated in the gondola. Figure from [74]

- Measure the background for up-going tau decays from tau neutrinos
- Study fluorescence from high altitude horizontal showers in a nearly constant density atmosphere to check hadronic interactions at ultra-high energies.

EUSO-SPB2 has a science payload that differs drastically from it's predecessor. It will be equipped with two main instruments for the planned long duration mission. The first one is the fluorescence telescope that uses an arrangement of three JEM-EUSO PDMs to observe the fluorescence emission of EAS. The second one will measure the Cherenkov light emission from lower energy EAS to study the background contribution in the aim of detecting cosmogenic Neutrinos. The optics of EUSO-SPB2 will shift from a refractive design to a reflective based design using a Schmidt telescope. This marks a departure from the traditional JEM-EUSO design and sets EUSO-SPB2 as a pathfinder oriented for the proposed satellite mission POEMMA.

2.3.2 POEMMA

The Probe of Extreme Multi-Messenger Astrophysics (POEMMA) [75] (see fig. 2.15) is a future NASA satellite mission designed to observe UHECRs and cosmogenic neutrinos.

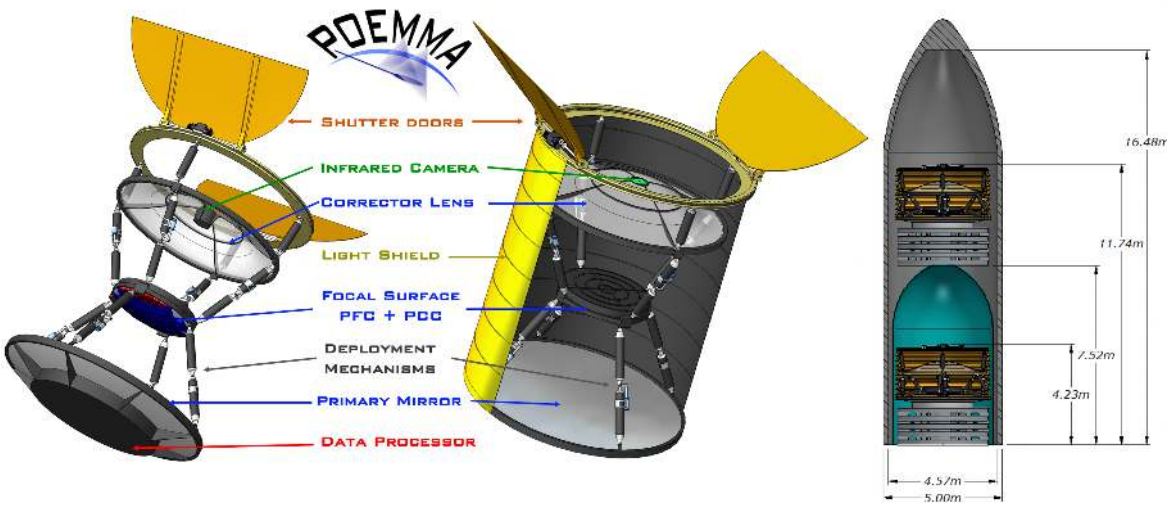

Figure 2.15: *Concept drawing of one of the POEMMA satellites with it's main components identified. Right:* Both POEMMA satellites accommodated inside an Atlas V fairing. Figure from [75]

POEMMA has a large contribution from members of the JEM-EUSO collaboration and in many aspects it will inherit some of the successes achieved by the latter. POEMMA will expand the scientific objectives of JEM-EUSO, which are as follows:

- Discover the nature and origin of UHECR.
- Discover the neutrino emission above 20 PeV from extreme astrophysical transients.
- Probe particle interactions at extreme energies.
- Observe transient luminous events and meteors.
- Search for exotic particles such as nuclearites.

POEMMA will use a twin satellite formation configuration. The identical satellites will perform observations in stereo mode using their Schmidt optics. Technology-wise POEMMA builds on technology developed for JEM-EUSO. The required technology will be tested both in suborbital flight (EUSO-SPB1) and spaceflight (Mini-EUSO). Despite the departure from the original principle of JEM-EUSO, a significant portion of the work done for the latter will continue to fulfill it's vision to observe UHECRs.

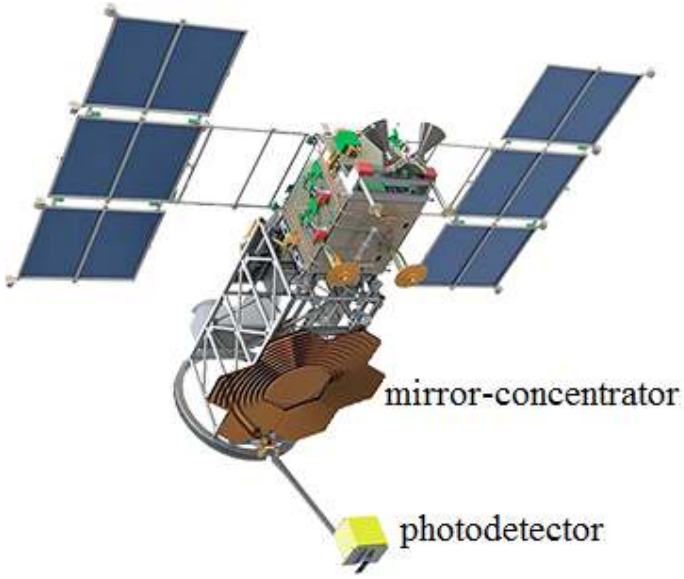

Figure 2.16: Schematic depiction of the Lomonosov satellite hosting the TUS detector. The mirror and photo detector module can be seen in front. Picture from [76].

2.4 Projects integrated in the JEM-EUSO Framework

2.4.1 Tracking Ultraviolet Setup

The Tracking Ultraviolet Setup (TUS) [76] is an experimental UHECR detector hosted on-board the Lomonosov satellite, designed to observe CR with $E > 5 \times 10^{19}$ eV. TUS is a pathfinder for the KLYPVE project [77] (2.4.2), but eventually both projects became part of the JEM-EUSO framework. The Lomonosov satellite was launched on April 28, 2016, making TUS the first instrument in orbit for detecting UHECR.

The instrument consists of a Fresnel type parabolic mirror-concentrator and a square shaped photo-detector formed by an array of 16×16 PMTs. The mirror is composed of seven equal sized hexagonal segments, it has a total collecting area of about 2 m^2 and a focal length of 1.5 m. The optical system has an efficiency of about 70%. The photo detector has a FoV of ± 4.5 deg, covering an area of approximately 80×80 km^2 at sea level, and a spatial resolution of about 5 km per pixel. The instrument has four main operation modes with a time resolution of: 0.8 μs, 25.6 μs, 0.4 ms and 6.6 ms where the former is used for UHECR observation and the rest for slower events in the atmosphere. The instrument is shown in 2.16.

During it's observation runs, TUS detected a plethora of events ranging from background noise caused by cosmic rays and transient luminous events like Elves. The most remarkable event is what seems to be a CR of extreme energy of the order of 10^{21} eV [78], however this energy is beyond the expected cutoff in the CR spectrum and if true it would be the highest

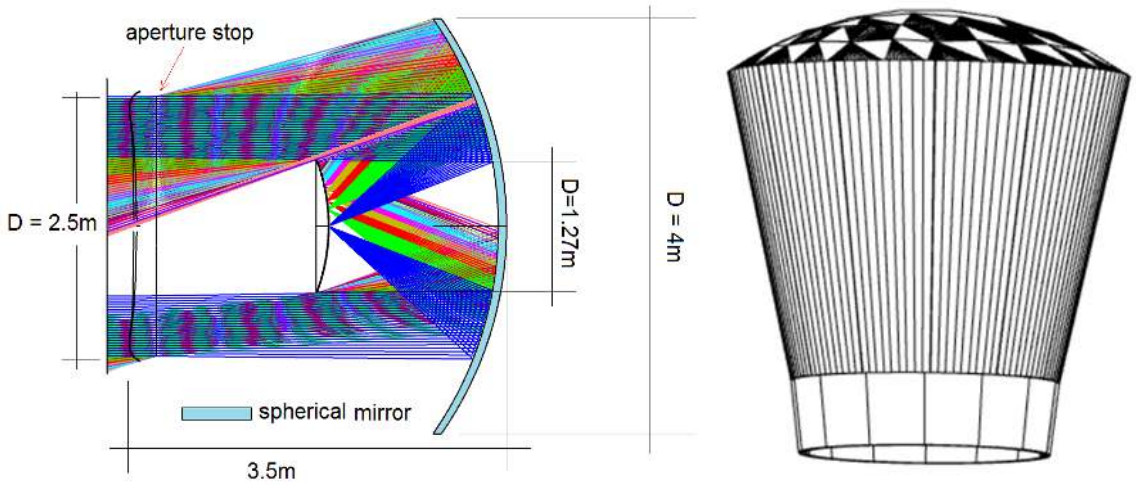

Figure 2.17: *Left:* Ray tracing simulation. *Right:* . Proposed design of the K-EUSO optics Schmidt camera. Figure from [77]

event ever detected, therefore it poses major questions regarding its nature. Further analysis is needed to confirm the event is an UHECR particle.

TUS stopped taking data in late 2017. On June 30, 2018 it was reported that the Lomonosov satellite had a malfunction in it's data transmission system and that attempts were underway to fix the problem. As of 2019 it seems that no recovery was possible, possibly ending the mission. Despite the short observation run, TUS was able to detect many events, proving it's capabilities and pioneering the detection of UHECR from space.

2.4.2 K-EUSO

KLYPVE-EUSO (K-EUSO) is a SINP-MSU (Skobeltsyn Institute of Nuclear Physics - Moscow State University) and Roscosmos[4] led mission that aims to place a UV telescope for the observation of EAS on board the Russian segment of the ISS. Initially, the instrument was conceived as a standalone UHECR observatory named KLYPVE [5] which was designed to build up on the experienced gained with the TUS pathfinder. However, eventual cooperation with the JEM-EUSO collaboration led to both projects becoming integrated into the EUSO framework. This led to an upgrade of the instrument using EUSO technology, improving it's performance and becoming K-EUSO [79]. It will be the first space detector capable of studying the UHECR spectrum and anisotropy with sufficient statistics and full celestial coverage, furthermore it will investigate Earth's atmospheric phenomena and search for strange quark matter [80].

The baseline design of the K-EUSO optics is different from the refractive Fresnel lens

[4]Russian Space Agency
[5]KLYPVE is the russian acronym for UHECRs

design of other JEM-EUSO pathfinders and instead uses a Schmidt camera based design. The telescope has a FoV of 40°, an entrance pupil diameter of 2.5 m, a 4 m diameter primary mirror with a focal length of 1.7 m, a corrector plate and a spherical focal surface. Simulations of the optical system result in an optical efficiency of 70% over the entire field of view and a polychromatic RMS spot size below 3 mm. The FS will feature 52 of the latest generation PDMs arranged in a concave shape (1.27 m diameter and a radius of curvature of 1.7 m) [77]. The preliminary design of K-EUSO's Schmidt camera is shown in figure 2.17.

Chapter 3

The Optics performance of the JEM-EUSO balloon pathfinders

3.1 Introduction

One of the features that sets apart the JEM-EUSO telescope and it's pathfinders from other experiments is the experimental optical system composed of Fresnel lenses. This idea can be traced back to the work of K. Greisen and A.N. Bunner [32] who built a prototype using Fresnel lenses (see sec. 1.4.2). The idea was later adopted by Takahashi [44] who played an important role in JEM-EUSO and thus the optics principle remained.

Despite the success of the EUSO-Balloon mission in terms of it's primary objectives, one of the issues of the experiment was the misunderstood performance of the optical system. The initial numerical ray tracing (RT) simulations of the optics predicted a promising performance. However, the characterization results showed a disagreement with the predicted performance and overall behavior of the system. This situation was again repeated for EUSO-SPB1 which also flew with a misunderstood optics performance not represented by the RT.

One of the main goals in this thesis is to model the optics and give a plausible explanation for the performance measured in both balloon pathfinders. This chapter is a continuation to the work done by C. Catalano [81] who characterized the EUSO-Balloon optics and attempted to find an explanation for the measured performance. We extend the work to include the characterization of the EUSO-SPB1 optics and aim to achieve a closure on the unresolved issues regarding the misunderstood performance.

The chapter starts by reviewing the history and functional principle of Fresnel lenses. We then describe the optics of EUSO-balloon and EUSO-SPB1. We review the main aspects of the characterization done by Catalano and its main results. We present the characterization of the EUSO-SPB1 optics and its results. We discuss the possible causes and present our hypothesis for the measured performance. We describe an experimental campaign designed to understand the behavior of each lens and conclude by presenting a semi-empirical model which can explain the measured performance.

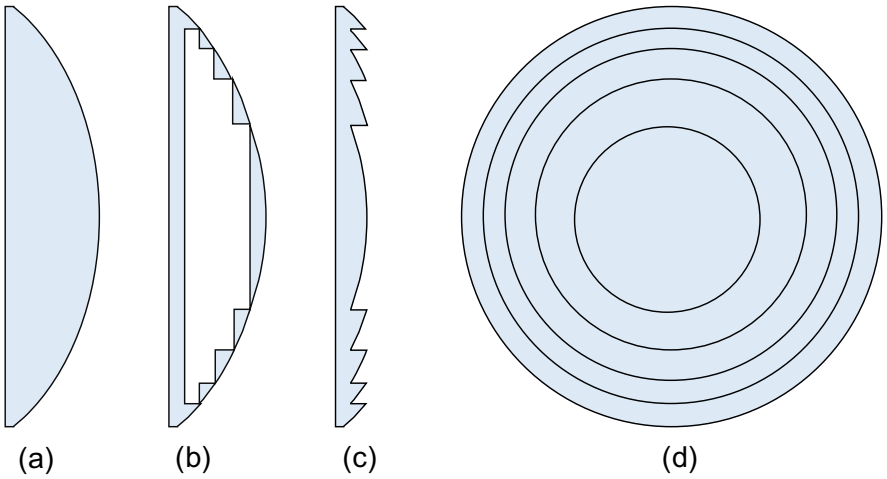

Figure 3.1: Design and functional principle of Fresnel lenses. *(a):* A base plano-convex lens. *(b):* The intermediate material of the lens is removed and the curvature is preserved. *(c):* The remaining curved sections of the material are collapsed to form a flat lens with annular sections. *(d:)* Front view of the lens.

3.2 History and principle of Fresnel Lenses

The principle behind the design of Fresnel lenses is that the direction of light does not change inside an optical medium. The light is refracted only in optical medium interfaces and thus the bulk of a lens internal material only absorbs light. The lenses are created by taking a regular lens as a base, for example, a plano-convex lens. The surface profile of the convex side is divided into annular sections which preserve the lens curvature, the intermediate material of the lens is removed and the annular sections are collapsed, this process is depicted schematically in figure 3.1. This produces a flat and light lens with similar optical properties as the base lens and acceptable performance at the cost of image quality due to the non-continuity of the lens curvature.

Fresnel lenses were developed by Jean Augustin Fresnel [1] (1788-1827), a French physicist and engineer whose contributions led to the acceptance of the wave theory of light. He was responsible for the design and production of the first Fresnel lens in 1822 which would serve to capture the light in lighthouses and collimate it to produce a powerful beam visible at long distances. In 1823 the lighthouse in Cordouan, France was the first one to be equipped with a Fresnel lens. With this addition it's light could be seen from a distance of about 31 km. The invention became extremely useful that soon enough other lighthouses were equipped with

[1] Typically Fresnel is credited with the invention of the lenses that bear his name, however he was not the first one to propose a similar design. Georges-Louis Leclerc, Comte de Buffon proposed grinding a piece of glass in concentric annular zones (date unclear), this design was first executed by Abbé Rochon in 1780. In 1773 Nicolas de Cordocet suggested building Buffon's design in separate pieces. In 1811 Sir David Brewster also proposed this mode of building lenses (it is unclear if he did so independently or referencing Buffons's idea). Fresnel was unacquainted with these explanations and independently developed the design in 1819 [82].

Figure 3.2: Example applications of Fresnel lenses. *Left:* Lighthouse. *Center:* Automobile headlight. *Right:* Solar concentrator

them and Fresnel lenses began to shine along European coasts.

Nowadays, Fresnel lenses are still present in lighthouses and are also quite popular in non-imaging optical applications One example is solar concentrators but also more ubiquitous devices like illumination systems of many types, such as car headlights and smartphone flashes. Some of the applications are shown in figure 3.2

3.3 Description of the EUSO-Balloon and EUSO-SPB1 optics

The goal of the optics JEM-EUSO and it's pathfinders consists in collecting the UV fluorescence photons of an EAS with a good efficiency for detecting UHECR. We'll refer to this efficiency as the Photon Collection Efficiency (PCE) of the optics, given by:

$$PCE = \frac{\text{Photons incident in the focal surface}}{\text{Photons incident in the front lens}} \tag{3.1}$$

Moreover, the collected photons should be densely focused, so a narrow point spread function (PSF) is also desired. By optimizing the PSF and the PCE we increase the signal-to-noise ratio on the PDM pixels, this in turn increases the trigger efficiency and decreases the energy threshold necessary to detect an EAS. Thus, the characterization of the optics is an important task to understand the performance of the optical system.

The optics of EUSO-Balloon and EUSO-SPB1 have the same baseline design. They are conceived to be a scaled down version and to offer a representative performance of the main JEM-EUSO instrument [49]. The optics are dimensioned to have a field of view of $\pm 6°$, to measure an UV night time emission of $\approx$ 1-1.5 photoelectrons per pixel per GTU (2.5 μs) and to produce a PSF size in the order of one pixel of the PDM ($\approx 3 \times 3$ mm^2) with a PCE of about 40% [83].

The baseline design of EUSO-Balloon and EUSO-SPB1 consists in a three lens (3L) configuration akin to JEM-EUSO: two single sided Fresnel lenses (L1, L3) and one middle diffractive lens (L2). The latter works as a corrector for the chromatism of the refractive elements. Ultimately, in both pathfinders, the 3L configuration was dropped due to a lower transmission efficiency observed during the optics characterization Thus, a "purely refractive" two lens (2L) configuration was favored and used for the flights in Timmins, Canada and Wanaka, New Zealand for EUSO-Balloon and EUSO-SPB1 respectively. Dropping the L3 resulted in a gain in efficiency but a PSF about three times wider. For the purpose of explaining the measured performance we will only focus in the 2L configuration. However, the performance results of the EUSO-SPB1 3L configuration are also presented.

The 2L flight configuration consists in two 1 m^2 aspherical based design Fresnel lenses: the front lens (L1) and rear lens (L3) which have focal lengths of 2585.6 mm and 600.2 mm respectively (these are reference values since the lenses can't form stigmatic images). Both lenses are milled only on one side of the PMMA sheet while the other side is flat (fig. 3.5 shows a cross section view of L1 and L3). The Fresnel zone sides of each lens are placed facing each other 1115 mm apart and the focal surface is placed at a distance from L3 (D_{L3}) of 440 mm. Two squared baffles are placed between L3 and the PDM for stray light mitigation, the baffles are placed at D_{L3}= 180 and 347 mm and have a side length of 524 and 280 mm respectively. A schematic of the configuration is shown in fig. 3.3.

3.3.1 Fresnel lens fabrication

The lenses were fabricated by RIKEN using 1m x 1m x 8 mm sheets of PMMA, this material was chosen for various EUSO pathfinders due to it's good UV transmission properties [83]. Figure 3.4 shows the refractive index and transmission properties of PMMA. To create the Fresnel zone structures, the lenses are milled using a single point diamond turning machine on the PMMA sheets. This operation is performed in two stages: first, by using a diamond tool bite of 0.5 mm radius to carve the desired form of the lenses. Second, by using a smaller tool bite of 50 μm radius to smooth down the lens surface topography and carve deeper the Fresnel zone valleys [84]. In order to avoid heavy scattering losses a surface roughness lower than 20 nm RMS (Root mean squared) is desired. Fig. 3.6 shows the lenses on their internal frame.

3.4 EUSO-Balloon optics characterization

The characterization of the EUSO-Balloon optics was performed at IRAP and took place during two campaigns in 2014 and 2015, pre-flight and post-flight respectively. The pre-flight work allowed to optimize the optics configuration for the balloon flight, i.e. the placement of the optical elements and PDM that gives the optimal PSF and PCE. However the campaign

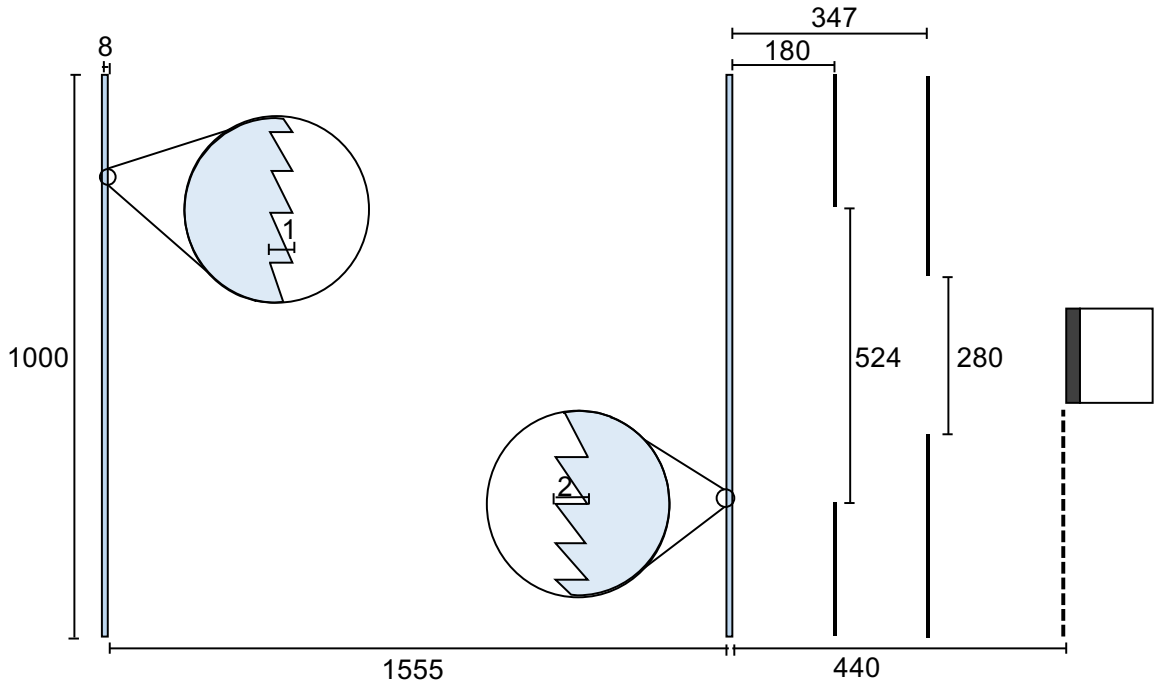

Figure 3.3: Configuration of the EUSO-Balloon optics for the Timmins flight, all units are in mm. This was optimized during the characterization campaign of the optics prior to the balloon flight. L1 and L3 Fresnel zones face each other

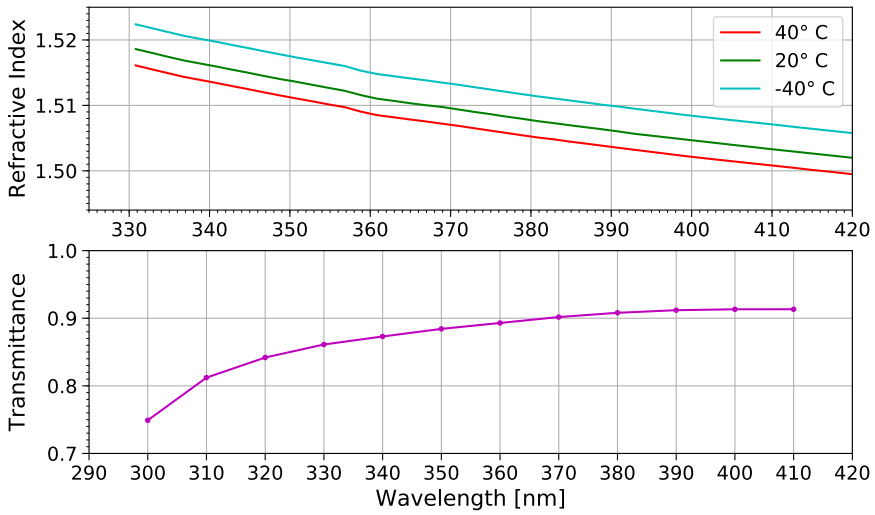

Figure 3.4: Optical properties of PMMA in the 300 - 405 nm Ultraviolet band. *Top:* Refractive index at three different operational temperatures of EUSO-Balloon. *Bottom:* Transmittance of PMMA

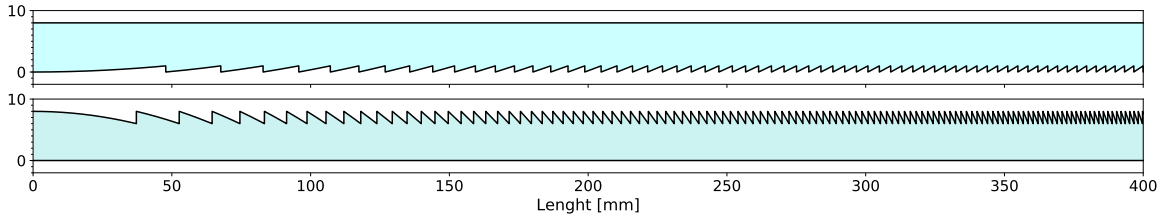

Figure 3.5: Fresnel lenses cross section from the center of the lens up to a radius of 400 mm. *Top:* Cross section of L1, the Fresnel zones have a height of 1 mm. *Bottom:* Cross section of L3. The Fresnel zones have a height of 2 mm and a shorter width than L1

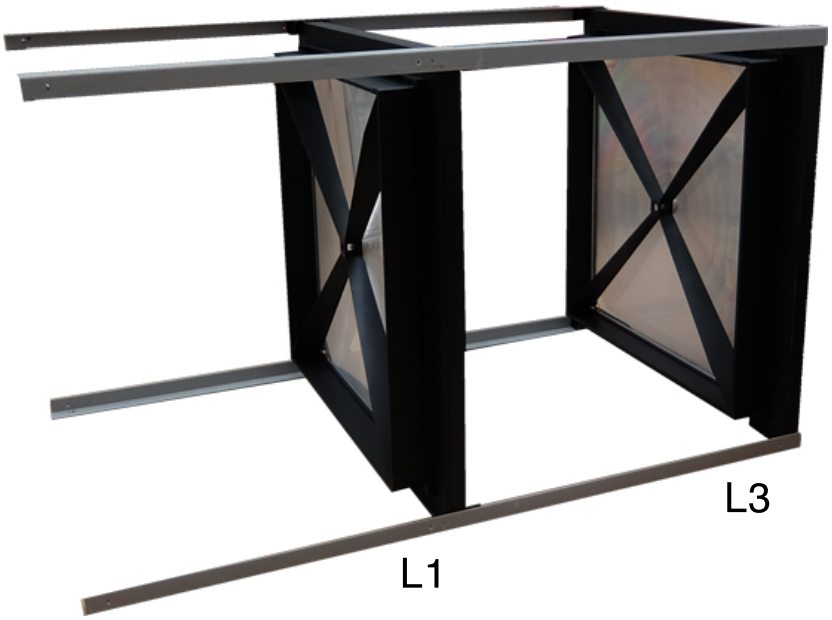

Figure 3.6: EUSO-Balloon lenses installed on their spider frames

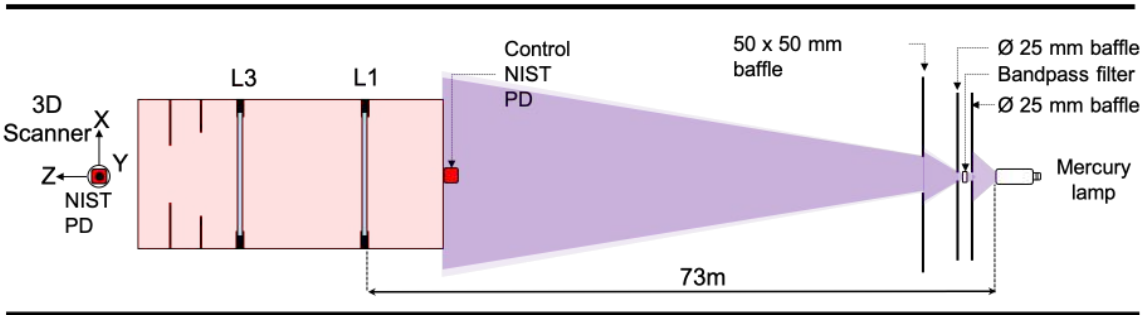

Figure 3.7: Schematic of the EUSO-Balloon characterization campaign setup, the light source is placed at a hyperfocal distance (73 m) away from the input of the optics.

was not exhaustive due to the tight deadlines imposed by the balloon launch date. The post-flight work allowed to measure more exhaustively the optics performance. This section revisits the work done by Catalano (and the EUSO-Balloon team) to characterize the optics and the main results obtained from the post-flight campaign. The employed methods and results are fully detailed in Catalano's dissertation [81].

The goal of the post-flight characterization is to understand the PCE[2] of the optics flight configuration as a function of angle. Even if the PSF size was increased by dropping the L2 this can be acceptable within certain limits. The goal of the optics is not to produce sharp images, but to focus the photons on the PDM to produce a signal above the trigger thresholds in the aims of observing an EAS, given that the FLT operates in 3×3 pixel cells. Then, the efficiency criterion can be relaxed up to a PSF diameter of 9 mm (henceforth $\mathrm{PCE}_{9\ mm}$).

3.4.1 Post flight test bench setup

The post-flight characterization of the optics was performed with a test bench developed at IRAP. The light source was placed at a hyperfocal distance (73 m) from the optics and was tested using four wavelengths (313, 337, 365 and 405 nm) and four incidence angles (0.1, 2.3, 3.3 and 4.5°). The whole setup is shown in fig. 3.7. The Point Spread Function (PSF) was measured using an XYZ focal plane scanner setup shown in fig. 3.8. For this setup the Z axis of the scanner is parallel to the optical axis of the telescope and the XY axes plane is normal to it.

The light source, a mercury arc lamp, has strong emission lines in the UV: 313, 334, 365 and 405 nm. Each wavelength was isolated with bandpass filters corresponding to each emission line, these bands are close to air fluorescence emission lines and hence are useful to characterize the UV PCE of the optics. The stray light coming from the source was mitigated

[2]In the optics characterization we don't measure photons but the radiant flux. However the efficiency is calculated in the same manner, i.e. ratio of flux measured in the focal plane w.r.t. incident flux. So we'll use the same parameter

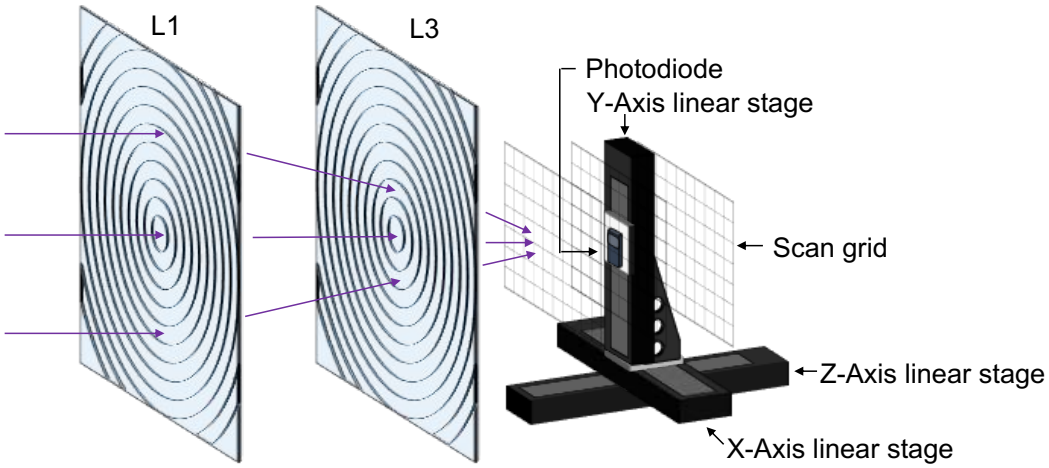

Figure 3.8: EUSO-Balloon focal plane measurement setup. A photodiode is placed in the vertical axis normal to the optical axis and various planes are scanned in a discrete 2D grid to map the distribution of the PSF at different distances from the rear lens. The Z axis corresponds to the optical axis.

Table 3.1: Acquisition equipment used for the EUSO-Balloon optics characterization campaign.

Equipment	Qty	Model	Manufacturer
Linear Stage	2	M-ILS100PP (100 mm)	Newport Instruments
Linear Stage	1	M-IMS300PP (300 mm)	Newport Instruments
Motion controller	1	ESP300	Newport Instruments
NIST Photodiode	2	PD300-UV	Ophir Photonics
Pinhole	1	$r = 0.70 \pm 0.05$ mm	Custom made
Powermeter	1	LaserStar Dual Channel	Ophir Photonics

by placing a series of baffles in front of the source along the optical axis.

The focal plane setup consisted of a PD, a power meter, three linear axis stages set in a 3D configuration (3D scanner) and a pinhole (Ø 0.7 mm). The PD was placed on the vertical deck of the 3D scanner and the pinhole was placed on top of the photosensitive surface of the PD to reduce the detection area, i.e. to have smaller pixels. The list of acquisition material is shown in table 3.1.

3.4.2 Measurement of the Point Spread Function

The PSF of the system was mapped by performing 2D scans, moving the PD in the X and Y axes and taking a measurement at each coordinate. After one plane was mapped the Z axis was shifted to scan another plane, this allowed to characterize the PSF at different image planes forming a 3D array of measurements called "cube scans". These measurements were

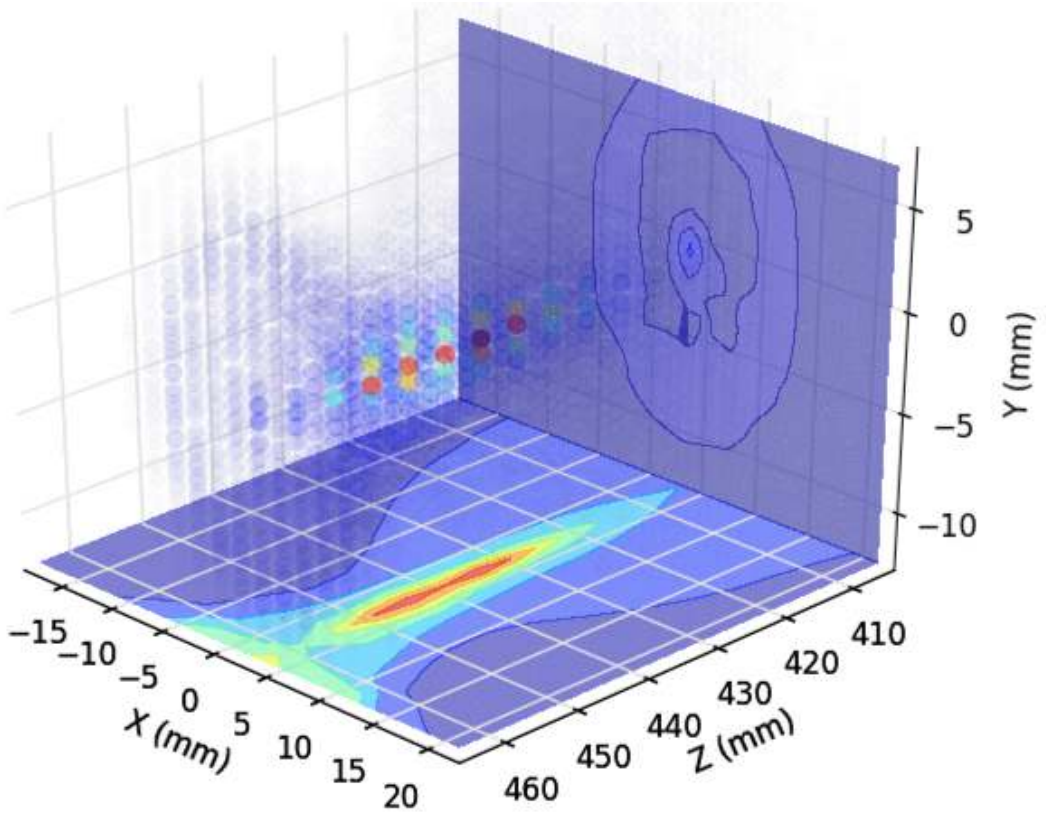

Figure 3.9: Cube Scan plot to measure the PSF at different distances from the rear lens. The Z axis corresponds the optical axis (distance from the rear lens) and the XY axes correspond to image plane coordinates. The translucent spheres represent the measurement points.

useful to understand the optics behavior as a function of D_{L3}. This is a trade-off between the optimal focal distance as a function of wavelength and the overall system efficiency. Figure 3.9 shows a typical 3D plot of a cube scan.

To determine the PCE of the system,the Encircled Energy (EE) is computed from the measurements. The EE at a given distance from the centroid of the PSF is the energy concentrated in a circle of a radius equal to this distance. In practice, the intensity of all the measurement points contained within a given radius is summed and then adjusted with the area ratio of all the points with respect to the given radius. This EE is then divided by the incident flux, this gives the PCE as a function of the PSF radius, as in equation 3.2:

$$E_{\mathrm{e}}(r) = \frac{1}{I_0}\frac{\pi r^2}{nS_p}\sum_{i=1}^{n} I_n \tag{3.2}$$

Where $E_{\mathrm{e}}(r)$ is the EE at a given distance r from the centroid; it is given as the percentage of the incident flux, I_0 is the incident flux calibrated by the control PD measurement, I_n is

Table 3.2: Comparison of the optics characterization measurements and the desired specifications established with the aim of observing an extensive air shower [83]. The minimal specifications are necessary to measure an UV background noise at a level usable by JEM-EUSO. The simulated performances are obtained from the ray tracing simulations and the measured performances obtained from the 2015 characterization campaign. The spot size and efficiency are averaged for all the wavelengths and incidence angles.

	Desired specifications	Minimal specifications	Simulated performance	Measured performance
Pupil area	> 0.785 m^2	> 0.785 m^2	0.95 m^2	0.91 m^2
Optimal D_{L3}	–	–	431 mm	440 mm
FoV	$> \pm 6°$	$\pm 4°$	$\pm 4°$	$\pm 5.1°$
FoV / px	$>0.25°$	0.17	0.17°	0.21°
PSF size	< Pixel Size (3x3 mm^2)	< PMT Size	9 mm RMS	12 mm RMS
PCE_{9mm}	60%	>15%	41.4%	22.7%

the intensity measured by the PD calibrated by the control PD, n is the number of PD measurements in a circle of radius r and S_p is the area of the pinhole placed on the PD.

3.4.3 Post flight characterization results

Table 3.2 summarizes the average performance results comparing the desired optics specifications (assuming the baseline 3L config.), the expected performance given by the RT simulations and the measurements. The optimal D_{L3}, (determined during the pre-flight campaign) is 440 mm while the RT simulations give 431 mm. The RMS PSF diameter was 12 mm in the measurements and 9 mm in the simulations (using the Full Width Half Maximum criteria). The mean $PCE_{9\ mm}$ was 22.7% while the simulations gave 41.4%. The field of view (FoV) was $\pm 5.1°$in the measurements and $\pm 4°$ in the simulations.

The $PCE_{9\ mm}$ at $D_{L3} = 440$ mm for each wavelength are summarized in table 3.3, this configuration favors the 365 nm wavelength. The EE plots of the four wavelength measurements and RT simulations for an incidence angle of 0.1°are shown in fig. 3.10. In order to get an approximation of the efficiency for real EAS events the efficiencies of the main emission lines of the air fluorescence (337, 357 and 391 nm) were calculated by linear interpolation, the results are shown in table 3.4.

Table 3.3: Encircled Energy efficiencies at a 4.5 mm radius measured during the characterization campaign. The plots are taken at the optimal position of the detector during the balloon flight: 440 mm away from L3. The gray column indicates that the distance of the detector during the flight is the same as the optimal distance along the optical axis for this wavelength. Table from [81]

Optical efficiencies		Wavelength			
		313 nm	334 nm	365 nm	405 nm
incidence angle	0.1°	$15 \pm 2\%$	$25 \pm 3\%$	$34 \pm 4\%$	$22 \pm 2\%$
	2.3°	$10 \pm 1\%$	NA	$29^{+2\%}_{-6\%}$	$19 \pm 2\%$
	3.3°	$8 \pm 1\%$	$19 \pm 2\%$	$25 \pm 3\%$	$16 \pm 2\%$
	4.5°	$6 \pm 0.6\%$	$16 \pm 2\%$	$30 \pm 3\%$	$25 \pm 3\%$

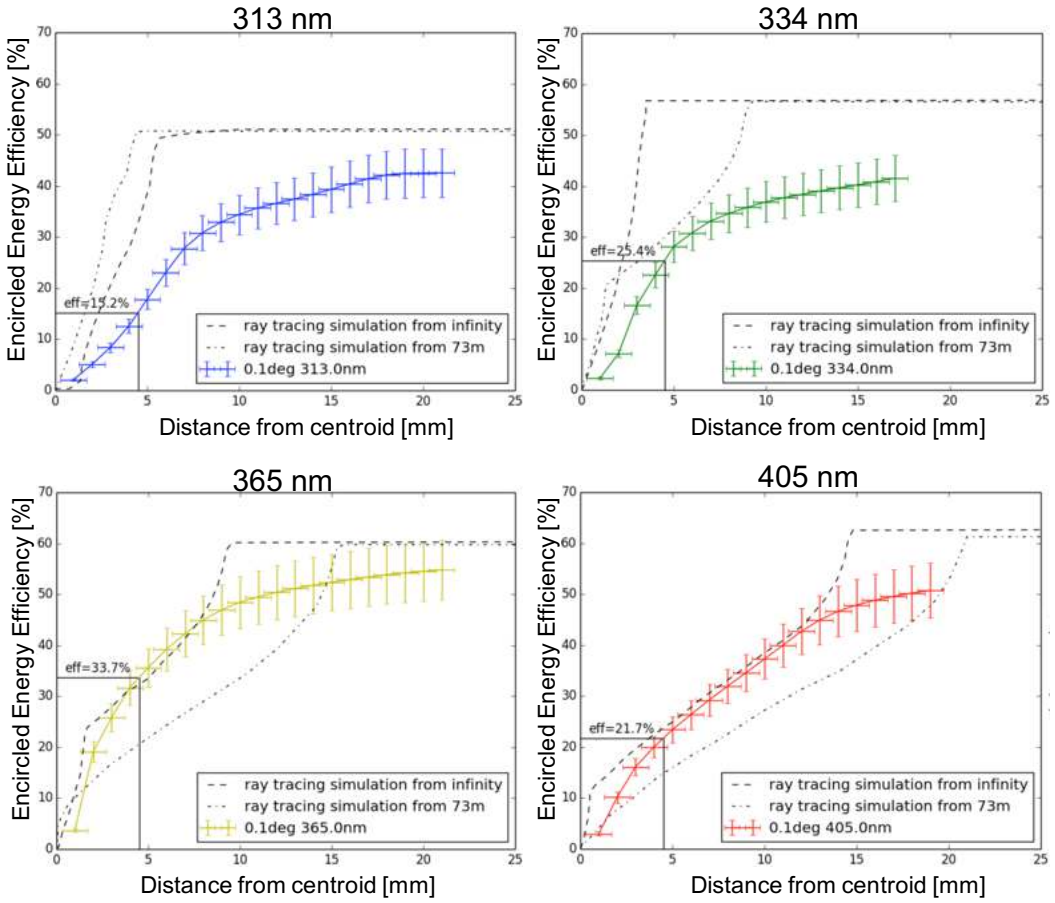

Figure 3.10: Encircled energy plots of the EUSO-Balloon post-flight characterization campaign and ray tracing simulations at 0.1° incidence. The light source is simulated at a distance of 73 m and Infinity. From left to right, top to bottom: 313 nm, 334 nm, 365 nm and 405 nm.

Table 3.4: Efficiency of the optics for a detection of air showers at the relevant fluorescence wavelengths. These results are interpolated from the measured efficiencies of the characterization campaign. Table from [81]

Optical efficiencies for an EAS		Wavelength			
		337 nm	357 nm	391 nm	mean
incidence angle	0.1°	$26 \pm 3\%$	$32 \pm 4\%$	$26 \pm 3\%$	$28 \pm 3\%$
	2.3°	$19 \pm 2\%$	$26 \pm 4\%$	$23 \pm 3\%$	$22 \pm 3\%$
	3.3°	$20 \pm 2\%$	$23 \pm 3\%$	$19 \pm 2\%$	$21 \pm 2\%$
	4.5°	$17 \pm 2\%$	$26 \pm 3\%$	$27 \pm 3\%$	$23 \pm 3\%$

The results show a significant discrepancy between the RT simulations and the measurements. Although the average results (see table 3.2) give a lower performance for the measurements. In the EE plots of each wavelength (see fig. 3.10), we can observe an odd behavior comparing the measurements against the simulations with the source at a 73 m distance. For λ= 313 and 334 nm, the simulations predict a higher PCE9mm and smaller PSF than the measurements. Whereas for λ= 365 and 405 nm, the simulations predict lower PCE and larger PSF size.

In all cases the measurements EE show a growth profile different than the simulations. This is characterized by two features: first there is a steep slope followed by a transition into a second less steep slope. The first central slope is the focal spot of the PSF and the second slope is a tail of diffused light. The latter does not achieve a stable level, indicating the presence of diffuse light at a larger radius. In the simulations, the EE plots exhibit a different growth profile which achieves a plateau and exceeds the measurements in all cases. The start of the plateau means that all the energy is contained at this point. These effects and their causes are discussed in section 3.6. Before proceeding to the discussion of the observed performance, we will present the characterization of EUSO-SPB1, whose performance showed a similar behavior

3.5 EUSO-SPB1 Optics characterization

The optics of EUSO-SPB1 were characterized with the goal of determining the optimal optical configuration for the balloon flight. In this campaign both 2L and 3L configurations were tested, but as mentioned in chapter 4 the 2L configuration was chosen. Nevertheless, we present the results of both configurations. We will proceed to review the characterization setup, the procedure and the results.

Equipment	Qty	Model	Manufacturer
XYZ Scanner	1		
Windmill scanner	1		
NIST Photodiode	2	PD300-UV	Ophir Photonics
Powermeter	2	Nova	Ophir Photonics
Fiber coupled LED	1	M340F3	Thorlabs
Fiber coupled LED	1	M365FP1	Thorlabs
Fiber coupled LED	1	M385FP1	Thorlabs
LED Driver	1	LEDD1B	Thorlabs
Bandpass filter (340 ±2 nm)	1	FB340-10	Thorlabs
Bandpass filter (355 ±2 nm)	1	FB355-10	Thorlabs
Bandpass filter (370 ±2 nm)	1	FB370-10	Thorlabs
Bandpass filter (390 ±2 nm)	1	FB390-10	Thorlabs
Aperture	2	1×1 , 3×3 mm	Custom made

Table 3.5: List of equipment used for the characterization of the EUSO-SPB1 optics

3.5.1 Test bench setup

The EUSO-SPB1 optics of was characterized using four wavelengths (340, 350, 370 and 390 nm), two incident angles (0 and 4 degrees) and using a 2L and 3L configuration. The light source was a collection of fiber coupled UV LEDs which cover parts of the fluorescence emission spectrum of air. Each UV line emission was isolated by using a bandpass filter centered at each of the four wavelengths with a Full Width Half Maximum (FWHM) of 10±2 nm. The output of the fiber coupled LED was split in two lines. The output of one line was placed in front of a PD to monitor the flux from the LED and the output of the other was placed at the focal point of a 1 m mirror. The divergent beam was then reflected on the mirror and collimated, simulating a source at infinity.

To characterize the performance of the EUSO-SPB1 optics for every wavelength a two step process is followed:

- The incident flux is determined by measuring the flux of the collimated source at the entrance of the optics.

- The PSF is characterized by using 3D scans in an similar manner as the EUSO-Balloon optics. However, different scan types were used.

Once both steps are completed, we can compute the efficiency from the resulting measurements. Each of the steps is described in detail in the next sections.

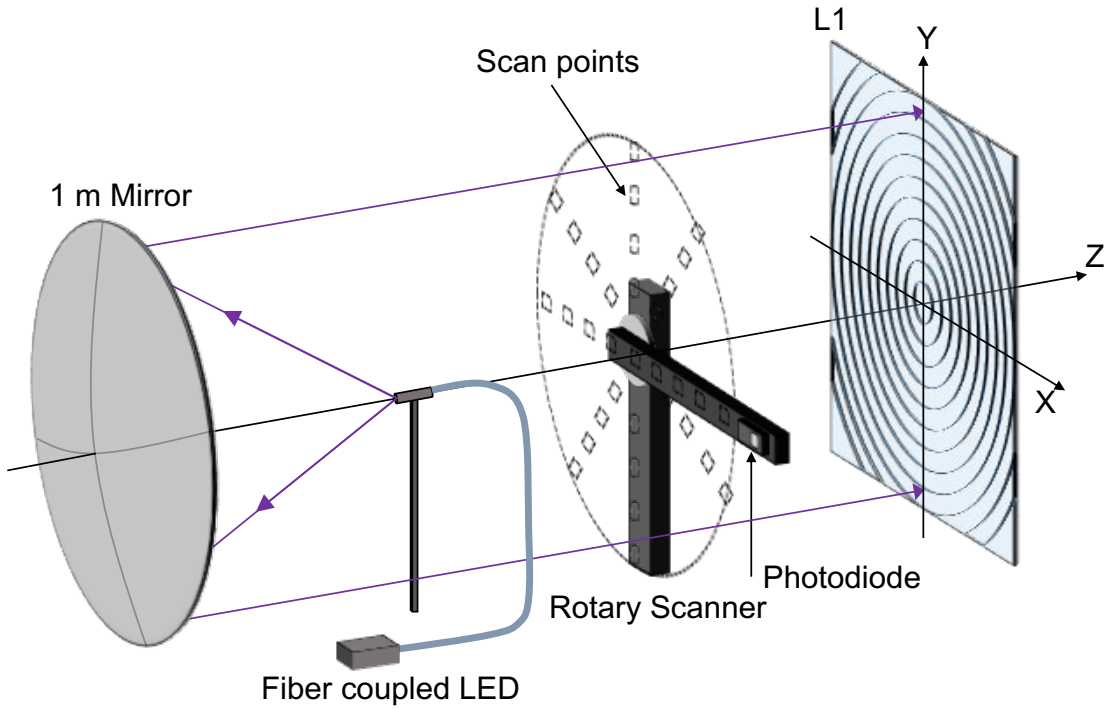

Figure 3.11: Incident flux measurement setup of the EUSO-SPB1 optics. The incident flux is determined by measuring the collimated source flux at the entrance of the EUSO-SPB1 optics with a rotation scanner.

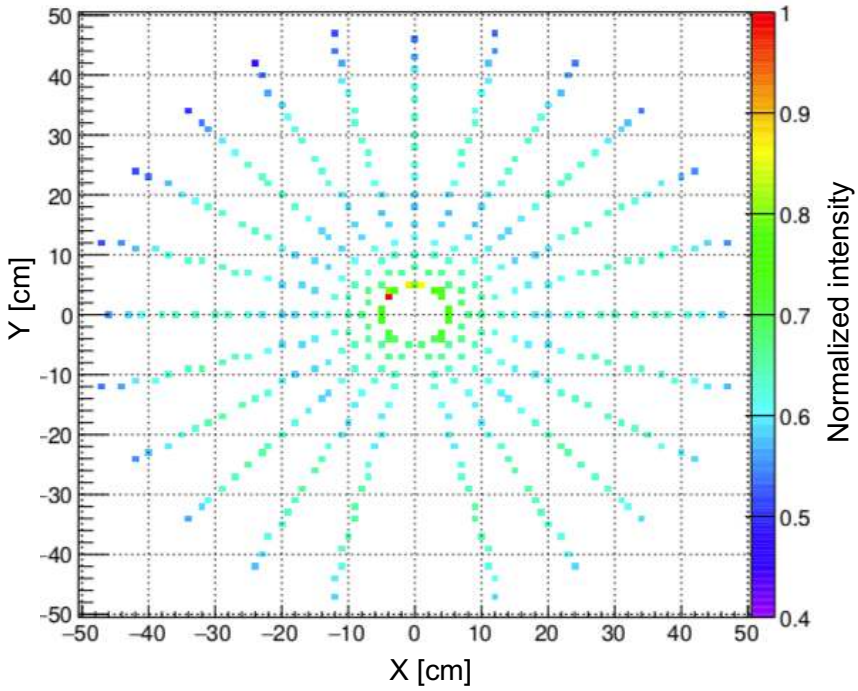

Figure 3.12: Rotation scan of the incident flux on the optics for $\lambda = 390$ nm. The windmill scanner perform movements in polar coordinates and takes measurements at multiple points covering the whole aperture of the optics, the scanned wavelength was 390 nm. The lack of data at the center and bottom column of the plot is due to the support structure of the scanner. Plot by J. Eser [85]

3.5.2 Measurement of the incident flux

The incident flux is measured by using a rotation scanner placed in front of L1. This part of the setup colloquially called "windmill scanner", is composed of a rotation stage and a linear stage whose combined movements allow to perform a controlled motion in polar coordinates. A photodiode is placed on the moving deck of the linear stage, which faces the collimating mirror and performs the measurements. The incident flux measurement setup is shown in figure 3.11. A scan routine is launched to measure samples of the incident flux covering the whole aperture of the optics, in total 408 samples per scan are taken. One such measurement is shown in figure 3.12. The scan shows that the intensity of the wavefront is not entirely uniform and shows an oscillatory behavior. There is a maximum near the center which then oscillates between a minimum and maximum again approximately every 10-12 cm, this is related to the non-uniform emission of the LED as a function of angle. This non-uniformity is taken into account when computing the incident flux which is calculated by interpolating and integrating over these points.

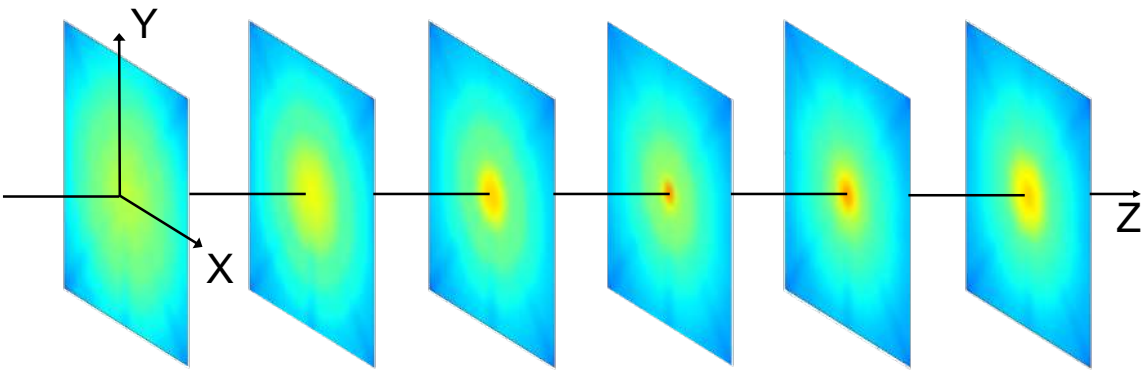

Figure 3.13: 3D Cube scan of the EUSO-SPB1 Optics. Each slice is one PSF measurement taken at different distances from the rear lens. The PSF goes from broader to narrower as the system achieves a better focus.

3.5.3 Point Spread Function measurement

To measure the PSF we set up a system identical to EUSO-Balloon, as described in sec. 3.4.2. However, in this time, we performed different type of scans as follows:

- **Optical axis scan:** This is a fast scan performed by centering the PD on the optical axis and performing a scan along it, the whole aperture of the PD (1 cm^2) is used. This scan allows to measure the efficiency of the system in a single 1 cm^2 pixel as a function D_{L3}.

- **3D Cube Scan:** These scans are identical to the scans done for EUSO-Balloon. The only difference was that we used either the whole PD aperture for a coarse 3D scan and squared apertures of 1×1 mm^2 and 3×3 mm^2 to obtain a finer granularity in the x and y axes. Figure 3.13

- **Slit scan:** In this scan the PD is covered with a vertical slit aperture with a width of 0.25mm. The scan is done along the Y axis and was used only to estimate the cross section of the PSF.

The PCE for optical axis scans at a given D_{L3} is given by:

$$PCE_{PD} = \frac{I_{PD}}{I_0} \tag{3.3}$$

Where I_{PD} is the PD measurement. The EE efficiency for each cube scan slice is given by eq. 3.2.

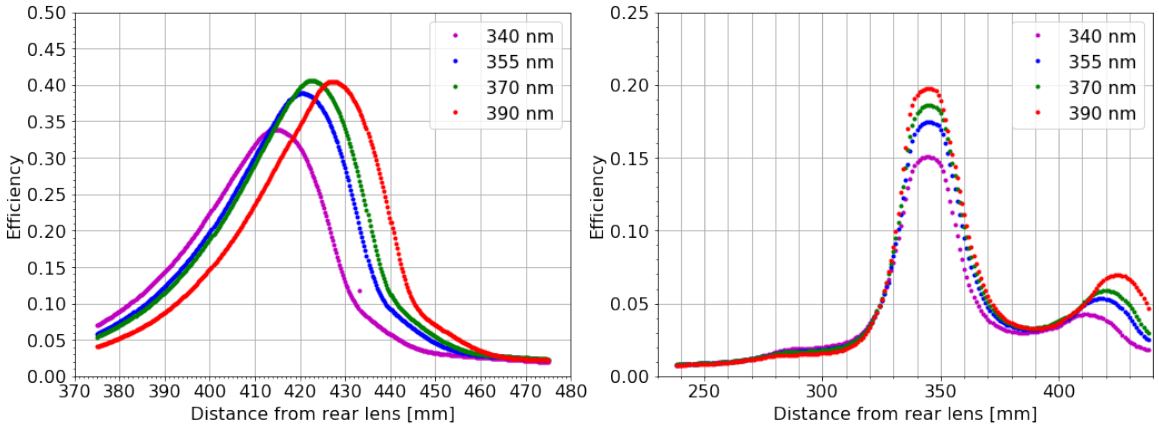

Figure 3.14: Optical axis scans of the 2L and 3L configuration. *Left:* The 2L configuration has a higher efficiency at the expense of a different focal length for each wavelength *Right:* The 3L configuration focuses all the wavelength's at the same position at the expense of lower efficiency. There is also a second focus which matches the foci of the two lens configuration.

3.5.4 EUSO-SPB1 optics characterization results

The results of the optical axis scans are shown in figure 3.14. It can be seen that for the 2L configuration each wavelength achieves an PCE_{PD} between 34 and 40%. However, the chromatism of the optics changes the optimal focus of each wavelength. The dispersion results in a focal length that varies from 3 to 6 mm between each wavelength. On the other hand, the 3L configuration shows two main foci. In the first one the chromatic aberration is corrected and all the wavelengths are focused at about $D_{L3} = 345$ mm, with a PCE varying between 15 to 20%. In second focus shows each wavelength focused at a D_{L3} that matches the multi-wavelength foci shown in the two lens configuration plot. This means that although the diffractive lens does manage to correct the aberration, it does not completely modulate the zeroth diffraction order and some efficiency is lost in this second focus.

The optical axis scans allowed to find the optimal D_{L3} for each wavelength in a 1 cm^2 area, this served to set the starting point for the cube scans. We then compute the EE of each cube scan slice and obtain the $\text{PCE}_{9\ mm}$ in the aims of determining the optimal PDM placement. For the 3L configuration this is easy to determine since all the wavelengths converge at the same D_{L3}. For the 2L configuration a compromise has to be taken due to the different focal lengths. As we saw previously, for the EUSO-Balloon optics the optimal D_{L3} was chosen by favoring one wavelength, for EUSO-SPB1 a different approach was taken. The optimal D_{L3} was determined by using a weighted average of all the tested wavelengths. This was calculated using two weighting factors to determine the significance of each wavelength for EAS observation. The first weight is the transmission efficiency of each wavelength in the atmosphere. The second is the relative intensity of each wavelength in the fluorescence emission spectra taken from [30]; the weighting factors are shown in table 3.6. Since the tested wavelengths do not exactly match the fluorescence emission lines, the relative intensity of the

Table 3.6: Weighting factors used to calculate the weighted efficiency of the EUSO-SPB1 optics. Weight 1 is the transmission efficiency of the wavelength in the atmosphere. Weight 2 is the relative intensity of the fluorescence emission lines which are closer to the tested wavelengths.

Wavelength (nm)	**Weight 1**	**Weight 2**
340	.62	1
355	.67	.88
370	.71	.05
390	.76	.28

emission line closest to each tested wavelength was used. As an example, the peak emission line is 337 nm so its relative intensity was used as the weight for the 340 nm which has the most comparable performance in the telescope optics, i.e. refraction and transmittance (see fig. 3.4).

The $PCE_{9\ mm}$ from all the cube scan slices is extracted to obtain the PCE as a function of D_{L3} as shown in figure 3.15. The weighted $PCE_{9\ mm}$ is shown in the black line and tends towards the shorter wavelengths (340 and 355 nm) due to their higher weight. At 0° incidence the 2L configuration gives a top weighted $PCE_{9\ mm} \approx 30\%$ at $D_{L3} = 419$ mm, whereas the 3L configuration gives $PCE_{9\ mm} \approx 14\%$ at $D_{L3} = 347$. At 4° incidence the 2L configuration gives a top weighted $PCE_{9\ mm} \approx 26\%$ at $D_{L3} = 415$ whereas the 3L configuration gives $PCE_{9\ mm} \approx 11\%$ at $D_{L3} = 345$. These measurements allowed to define the optimal D_{L3} to place the detector for each optical configuration. A $D_{L3} = 417$ and $D_{L3} = 346$ was chosen for the 2L and 3L configurations respectively.

The encircled energies for the 2L and 3L configurations at a respective $D_{L3} = 417$ and $D_{L3} = 346$ at 0° incidence are shown in figure 3.16. Like the EUSO-Balloon optics, the growth of both plots show two main components: A steep slope followed by a transition into a less steep slope. In the 3L configuration the slope is steeper and makes the transition at a shorter distance from the centroid, this means that the focal spot is concentrated in a smaller radius and proves the better focusing capabilities of the 3L configuration. The second slope represents light that is scattered around the focal plane, which contains a significant fraction of the flux. To understand the extent of this diffused light, the encircled energies of a small and coarse cube scan measurements in a two lens configuration were combined. The first one used a 3×3 mm^2 aperture size, the second one used the full PD aperture of 1×1 mm^2 and was computed starting at a larger radius due to the bigger pixel size. The resulting plot is shown in figure 3.17, it can be seen that the diffuse light curve keeps rising up the scan range of 115 mm from the centroid and contains about 20 to 22% of the incident flux.

Despite the diffuse light behavior which was not well understood at the time of the characterization, in both cases the 2L configuration shows a higher efficiency for all wavelengths. This made it the most likely configuration to be used for the flight. However, the final decision was made after analyzing the results of the experimental campaign done in the Utah desert

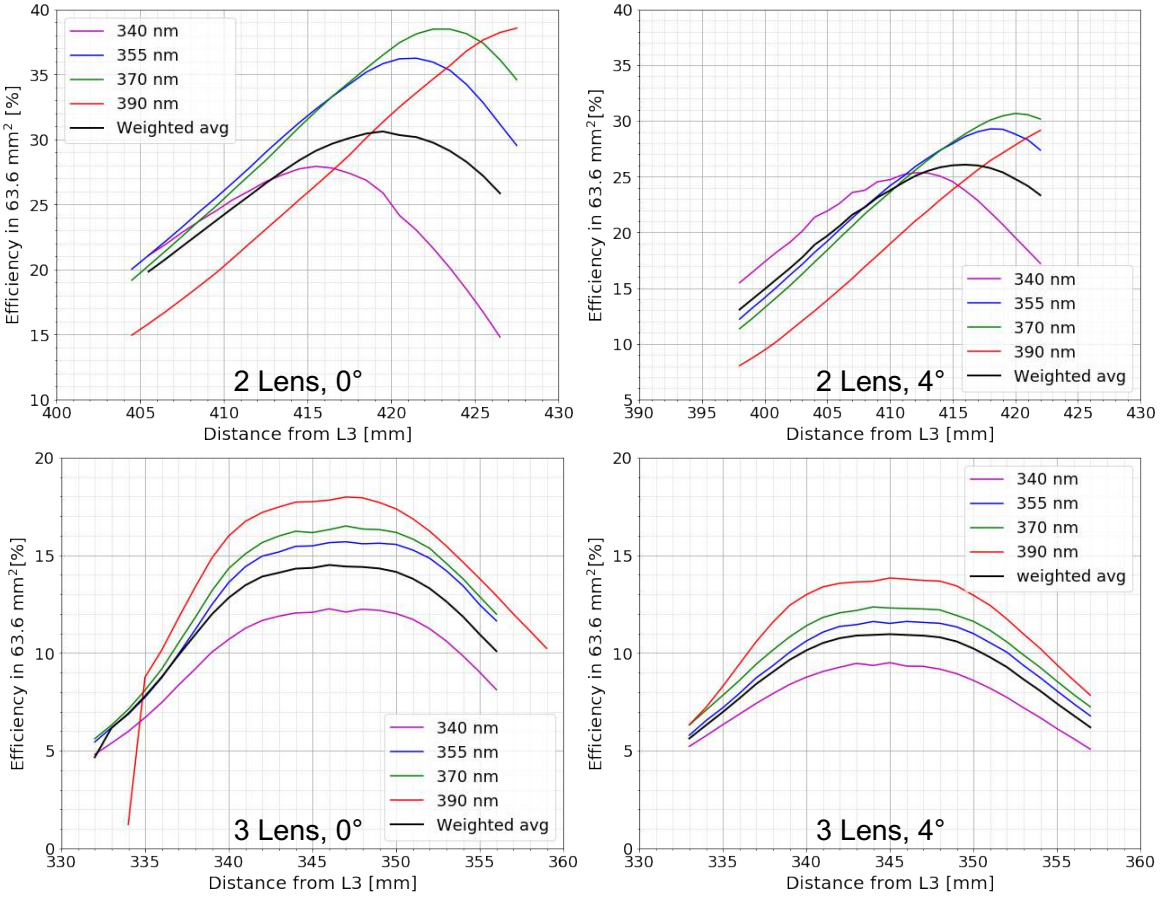

Figure 3.15: *Top Row:* Efficiencies for the two lens configuration with a 0°(left) and 4°(right) incidence angles, the black line denotes the average weighted efficiency calculated using the weights listed in table 3.6. Bottom Row: Efficiencies for the three lens configuration with a 0°and 4°incidence angle, all of the wavelengths are focused at the same distance from L3.

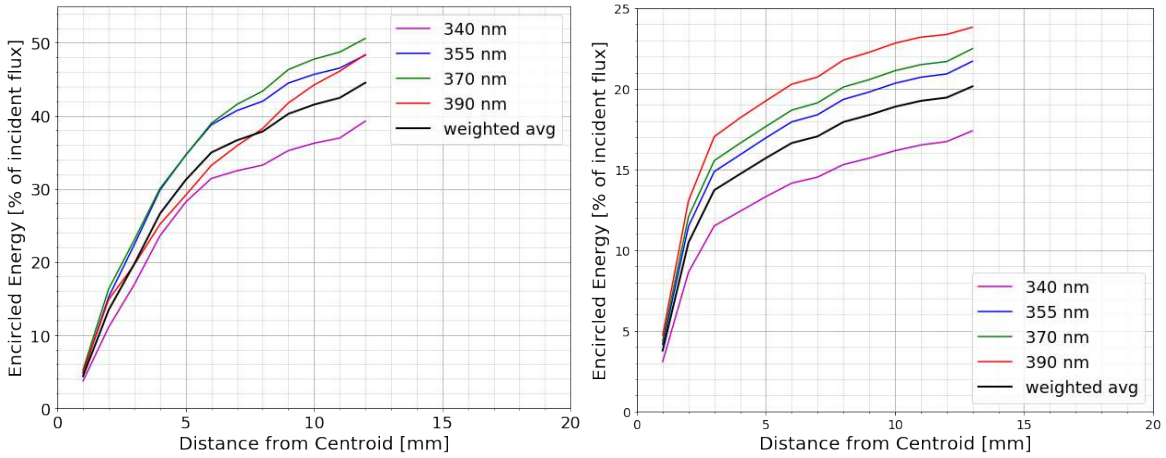

Figure 3.16: Encircled energies of the EUSO-SPB1 optics at an incidence angle of 0°. *Left:* Results for the two lens configuration at a distance of 417 mm from L3. *Right:* Results for the three lens configuration at a distance of 346 mm from L3

with the fully assembled instrument, as explained in sec. 4.2.1.

3.6 Post Characterization conclusions

As we saw, the EE energy plots of the EUSO-Balloon and EUSO-SPB1 characterizations showed a similar pattern. A central focal spot characterized by a steep growth in it's PCE curve which then transitions into a diffuse light background, characterized by a less steep PCE curve. For the remainder of the discussion we will focus on the EUSO-Balloon optics, since it's the only one that could be recovered and retested after it's flight.

Following the analysis of the EUSO-balloon characterization campaign results, many questions arose regarding the performance of the instrument due to the differences between measurements and simulations shown in section 3.4.3. Several hypotheses were proposed between the optics group to explain the discrepancies in the measured performance. However, there was no conclusive result which could explain the measurements and not all hypotheses could be tested due to the fact that the available manpower and resources were already allocated to the EUSO-SPB1 campaign which took flight less than two years after EUSO-Balloon. Quoting Catalano [81] on this topic:

"It wasn't stated from where these differences came: From a simulation not close to reality (Diffuse light not reproduced, overvalued focusing power, surface roughness not taken into account) or from a difference in the fabrication of the lenses (Fresnel Lenses not milled completely). This differences make today an intense discussion topic with the Fresnel lens experts in the collaboration".

Knowing that the presence of diffuse light is a major factor in the performance, the next

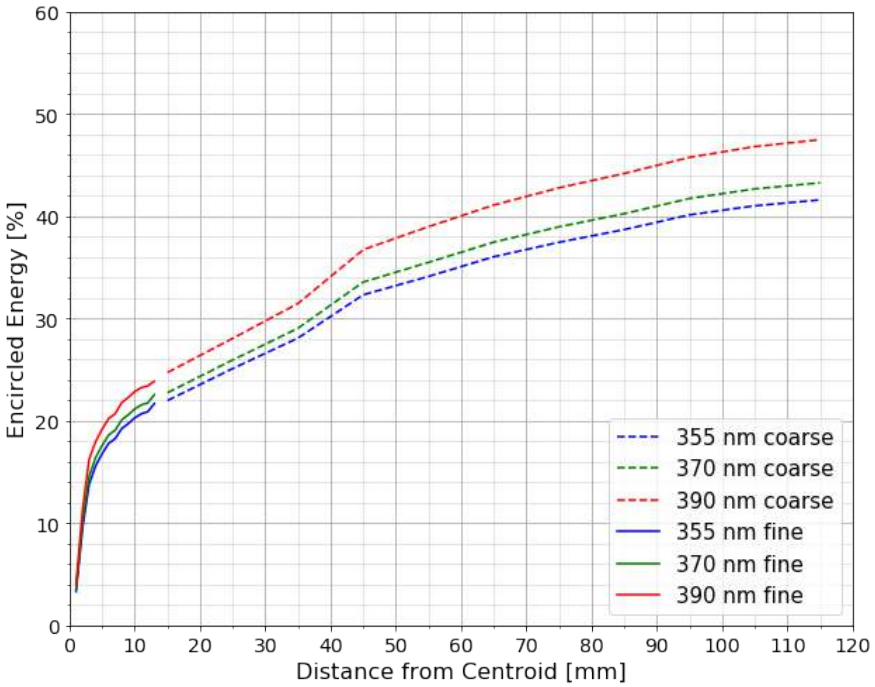

Figure 3.17: Encircled energy plot of fine and coarse scans of the EUSO-SPB1 optics using a 3L configuration. The combination of measurements show that the efficiency increases very slowly as a function of the distance from the PSF centroid and only achieves a maximum efficiency between 40 and 50% depending on wavelength

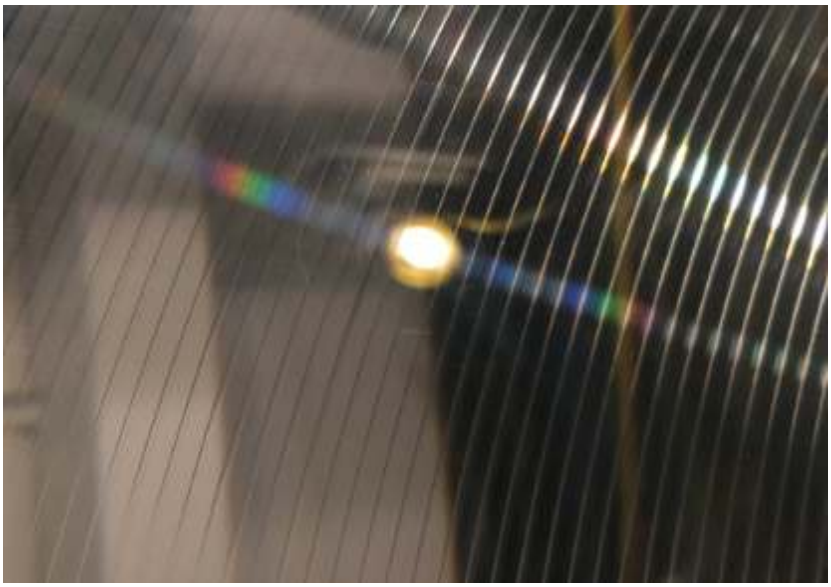

Figure 3.18: First observation of the unintended diffraction effects of the Fresnel lenses

time that the lenses were available we performed a thorough observation to try to identify the causes.

3.7 Observation of diffraction effects by the Fresnel lenses

The EUSO-Balloon Fresnel lenses were designed to be refractive elements. The grated structure and sharp edges can cause diffraction effects, but since the width of Fresnel zones is much larger than the wavelength of light observed by the instrument, the lenses are treated entirely as refractive optical elements. Because of this the use of ray tracing methods seemed suitable enough to simulate the optics.

The decisive hint to what was happening came when observing at a photograph taken during the Golden characterization tests in 2016. A light source situated behind one of the lenses showed a band of colors with the dispersed spectrum of the source (see 3.18). Initially no second thought was given since chromatic dispersion is expected for a refractive element. However, a deeper analysis of one of these dispersion patterns allowed to recognize it was in fact diffraction. In figure 3.18 we can see the that the white light of the bulb corresponds to the 0^{th} diffraction order which preserves the color of light and behaves according to refraction. At both sides of the 0^{th} order the color components can be seen, this are the $\pm 1^{st}$ diffraction orders. The shorter wavelengths (violet) are closer than the long ones (red), meaning that the former are dispersed at smaller angles, a characteristic of diffraction whereas in refraction the shorter wavelengths are dispersed at larger angles.

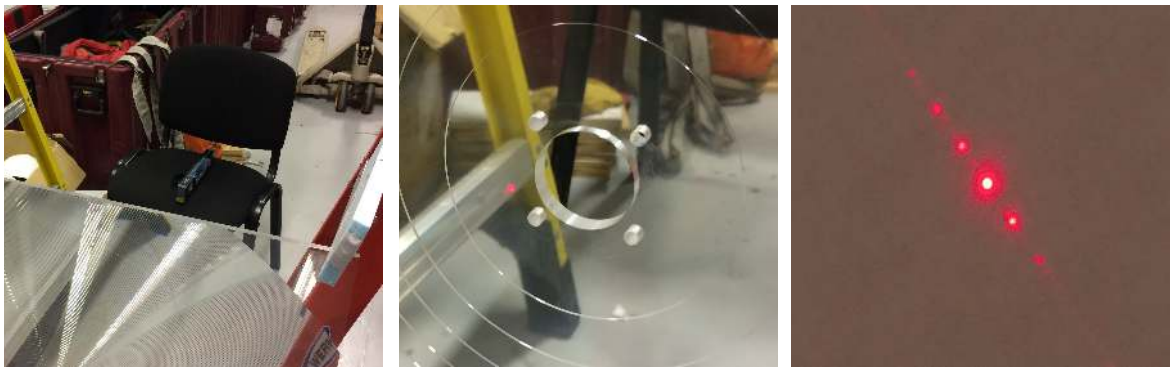

Figure 3.19: Improvised test to verify diffraction produced by individual Fresnel zones. *Left:* A red alignment laser used as pointer. *Center:* Laser dot visible on the first Fresnel zone. *Right:* The diffraction pattern produced when the laser beam goes through the lens.

Testing the diffraction effect more extensively would require some time. At the time of the dispersed white light observation the lenses were taken as back-up for the EUSO-SPB1 preparation campaign and were unavailable. However, during the launch campaign a second chance to observe the diffraction effects arose and was promptly seized. An improvised setup was put in place, it consisted in simply shooting a laser through the lens. Care was taken to do it in the center of a Fresnel zone and avoiding the edges. The result was a diffraction pattern with multiple diffraction orders clearly visible, this proved that the refractive zones of the lenses were also acting as diffractive elements. The improvised setup is shown in fig. 3.19. The tested Fresnel zone shown in the central panel of fig.3.19 is not necessarily the most representative for the whole optics and most of it is covered by the spider frames, but the laser was also shot through other zones and the same effect was observed. Although the whole setup was improvised and the observation was not quantitative, it provided an explanation for the diffused light.

3.8 Scattering of light by small-scale structure of the lens surface

Diffraction patterns like the one observed in the right panel of fig.3.19 can be produced by diffraction gratings. In a similar way the diffusion effects observed on the results can be traced back to microscopic irregularities on the surface of the lenses. This is because of the reality of optical fabrication methods, which produces surfaces that deviate from the ideal smooth surface profiles that optical models generally assume.

As the lenses are turned on a lathe, it is natural that some of these deviations are periodic undulations across the topography of the lenses [86]. Typically these features are classified according to their spatial frequency content as follows [87]:

- Low Spatial Frequency (LSF): These are macroscopic figure deviations. They lead to conventional aberrations, which scatter light out of the PSF core.

- Medium Spatial Frequency (MSF): Features in these regime affect the performance through scattering at small angles. This smears out the PSF core, reducing the image resolution.

- High Spatial Frequency (HSF): Features in this regime scatter the light at wide angles. This removes light from the PSF core, reducing the image contrast. The typical surface roughness parameter is in this regime.

The borderline between each regime is loosely defined in the literature as it varies as a function of the wavelength, one practical definition can be found in [86].

During manufacturing of the lenses, the rotational motion of the tool bite along the radius of the lens produces concentric undulations (henceforth called grooves). As the period of the grooves approaches the wavelength it can modulate the wavefront through diffraction. Therefore, the diffusion observed on the EE plots can be explained by residual fabrication features in the HSF and MSF regimes. The cross section of these two features is depicted in figure 3.20(a) and 3.20(b).

Another fabrication feature is derived from finite radius of the tool bite. This poses a limit in the cutting depth of the Fresnel zones valleys. Therefore, the valleys are rounded and have a radius roughly equal to the radius of the smaller tool bite (50 μm). This scatters light at different directions compared to the baseline design, reducing the useful area of the lenses. This feature is depicted in figure 3.20(c).

After the fabrication of the lenses was completed, the surface roughness of both was measured with an atomic force microscope (AFM) and deemed satisfactory [84]. The AFM offers very high resolution capabilities in the order of nanometers and is ideal for probing the surface profile at very high spatial frequencies. For JEM-EUSO telescopes, the surface quality specification of the optics is a root mean squared surface roughness (R_q) of 20 nm. Due to the large size of the lenses and the tight schedule imposed by the balloon launch only a few sample points were tested for each lens: seven points for L1 and four for L3. Figure 3.21 shows the AFM scans of three Fresnel zones per lens.

However, despite the precisions of an AFM scan, the lenses were only tested on a small spatial scale (< 80 μm). This does not give a complete view of the surface topography at different spatial regimes. As neither the HSF nor the MSF features were taken into account by the simple ray tracing simulation, it was decided to re-test the lenses by performing an experiment to study the transmission of light through the lenses in detail. The experiment and results are described in sec. 3.9.

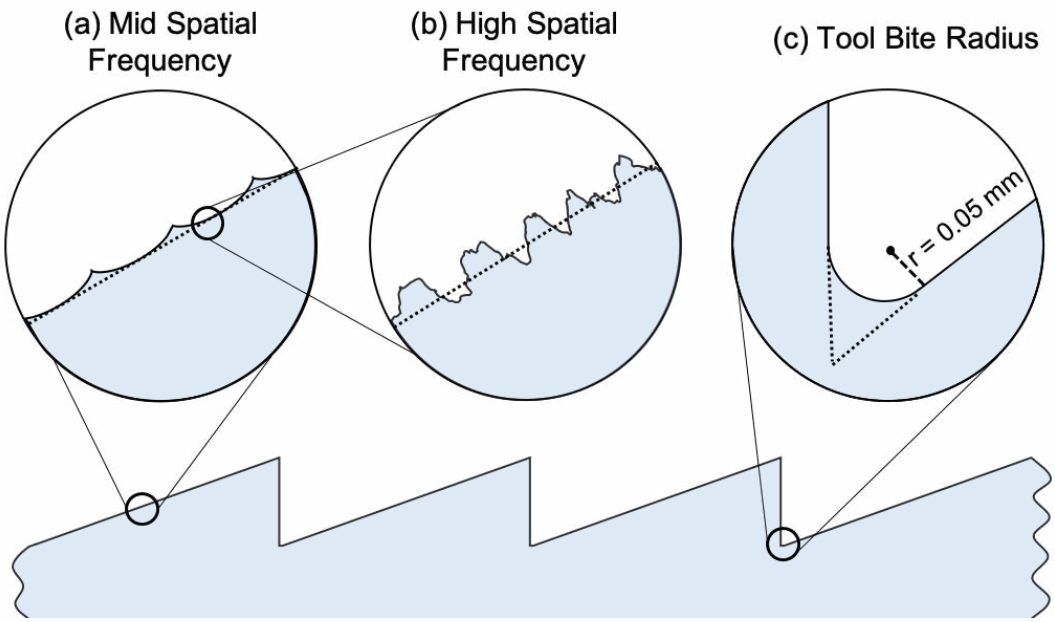

Figure 3.20: Cross section of a Fresnel lens depicting the tooling residues affecting the performance. The dotted lines in the close ups represent the ideal surface profile. *a)* Mid spatial frequency ripples. *b)* High spatial frequency roughness. *c)* Tool peak rounding limit.

3.9 Fresnel lens diffusion experiment

We performed an experiment based on our previous experiences to test and quantify the diffraction provoked by the lenses and determine it's significance in the optics performance. The experiment consists in shooting a laser beam through single Fresnel zones of each lens and measure in an automated manner how the beam intensity is distributed on both sides of the lenses (transmission and reflection), fig. 3.22 shows a schematic representation of the experiment.

3.9.1 Experiment setup

The light source was a 405 nm laser with an elliptical beam (3.8 x 1.8 mm), this offers a direct comparison with the same wavelength tested during the characterization campaign of EUSO-Balloon. The detector is a NIST Traceable photodiode (PD) (200 to 1100 nm range) with an aperture of 10×10 mm^2. To read the data a compatible power meter is used. To move the detector two linear motion stages are set in a 2D configuration (henceforth called XY scanner). The motors are driven by a controller which can be operated through a serial connection. Additionally, different sized pinholes and slits were used to block the sensitive area of the PD and create smaller pixels to obtain a finer resolution. The slit used depends on the type of scan performed (see sec. 3.9.2 for details). The list of equipment is shown in

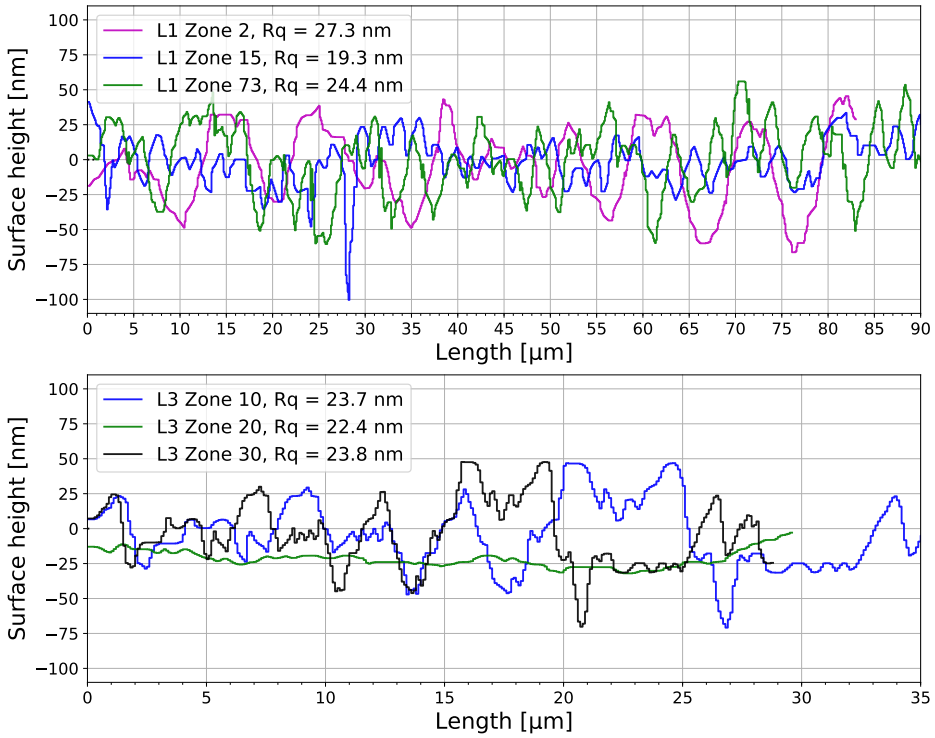

Figure 3.21: Atomic force microscope scans of L1 and L3, Rq is the root mean squared surface roughness. *Up:* L1 scans of Fresnel zones 2, 15 and 73. *Down:* L3 scans of Fresnel zones 10, 20 and 30.

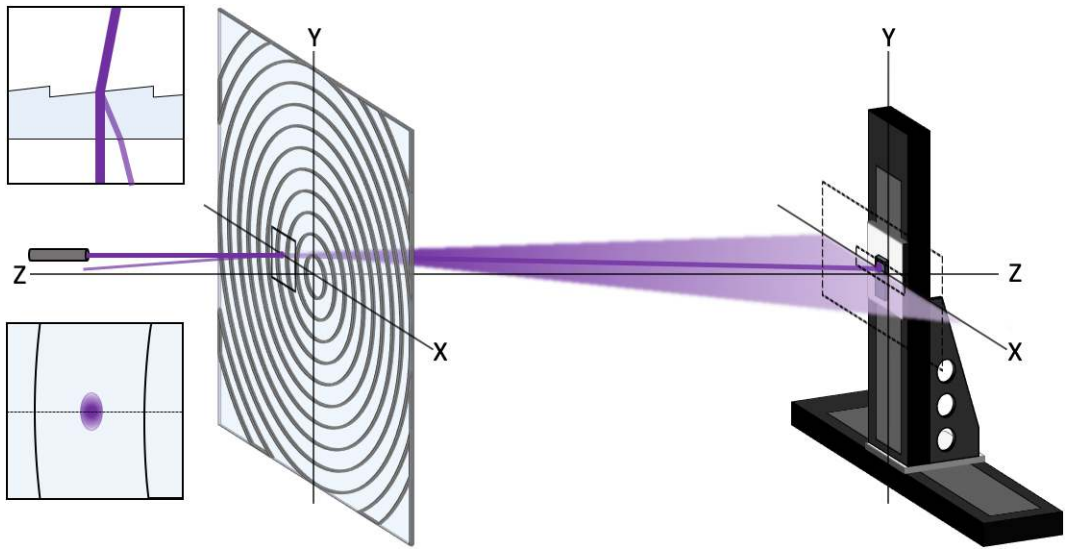

Figure 3.22: Schematic representation of the Fresnel lens localized diffusion experiment. A laser is shot through one Fresnel zone, the diffused pattern is measured using a NIST traceable Photodiode mounted on a 2D motion platform to perform automated measurements.

Table 3.7: List of equipment used for the diffusion experiment campaign.

Equipment	**Qty**	**Model**	**Manufacturer**
Fresnel Lens	2	L1, L3	RIKEN
Diode laser (405 nm)	1	CPS405	Thorlabs
Linear Stage	1	M-ILS100PP (100 mm)	Newport Instruments
Linear Stage	1	M-IMS300PP (300 mm)	Newport Instruments
Motion controller	1	ESP300	Newport Instruments
NIST Photodiode	1	PD300-UV	Ophir Photonics
Powermeter	1	Vega	Ophir Photonics
Rectangular slit	1	S100RD	Thorlabs

table 3.7

The experiment was set up in a conference room at IRAP. The room was not suited to be used as an experimental dark room, therefore it had to be carefully adapted. All light exterior light sources (windows, door) were blocked and the darkness level of the room was measured using the PD. The measurements were performed at various positions in the room and also in the same plane were the data would be taken. We measured average darkness level of 33 pW. This was satisfactory for the experiment since the power of the laser is eight orders of magnitude higher (4.5 mW). Figure 3.23 shows pictures of the experimental setup.

To measure the diffuse light an automated routine was created using the python language that controls the motion and measurement equipment. The axes of the XY scanner are connected to the motion controller, the powermeter and motion controller are connected to a personal computer and communicate through the RS232 protocol. To encapsulate the serial port access and be able to communicate with the devices the `pySerial` python package [88] is used. The commands to operate the powermeter and controller are encapsulated in a custom made python library. A flux diagram of the scan routine is shown in fig. 3.24.

3.9.2 Scan procedure

Before starting each scan the laser was turned on for 30 minutes to let the power stabilize. When setting the laser position care is taken so that the beam illuminates a single Fresnel zone, avoiding the crests and valleys of contiguous zones (see fig. 3.22). The transmitted pattern is then measured using different type of 2D scans as follows:

- **Fine Scan:** This was performed by placing a rectangular aperture (0.1 x 3 mm^2) on top of the PD. This allowed to obtain a finer granularity in the X axis and resolve better the diffraction pattern along this axis. The beam is shot at 0° incidence along the X axis of the lenses, this way the beam is also refracted along the same axis. An area of 150×15 mm^2 was scanned and the distance between the PD and the lenses was 2900 mm for L1 and 431 mm from L3.

Figure 3.23: Pictures of the Fresnel lens localized diffusion experiment setup. *Top left:* A Fresnel lens is standing on the front and in the back is the XY scanner. *Bottom left:* A close up view of the XY scanner holding the photodiode, the black cover on the back shows the diffracted beam of the laser. *Right:* The door is carefully covered from outside, the instrument cables are passed through a door shaft carefully isolated from exterior light and the cables are connected to the motion controller and powermeter (not visible).

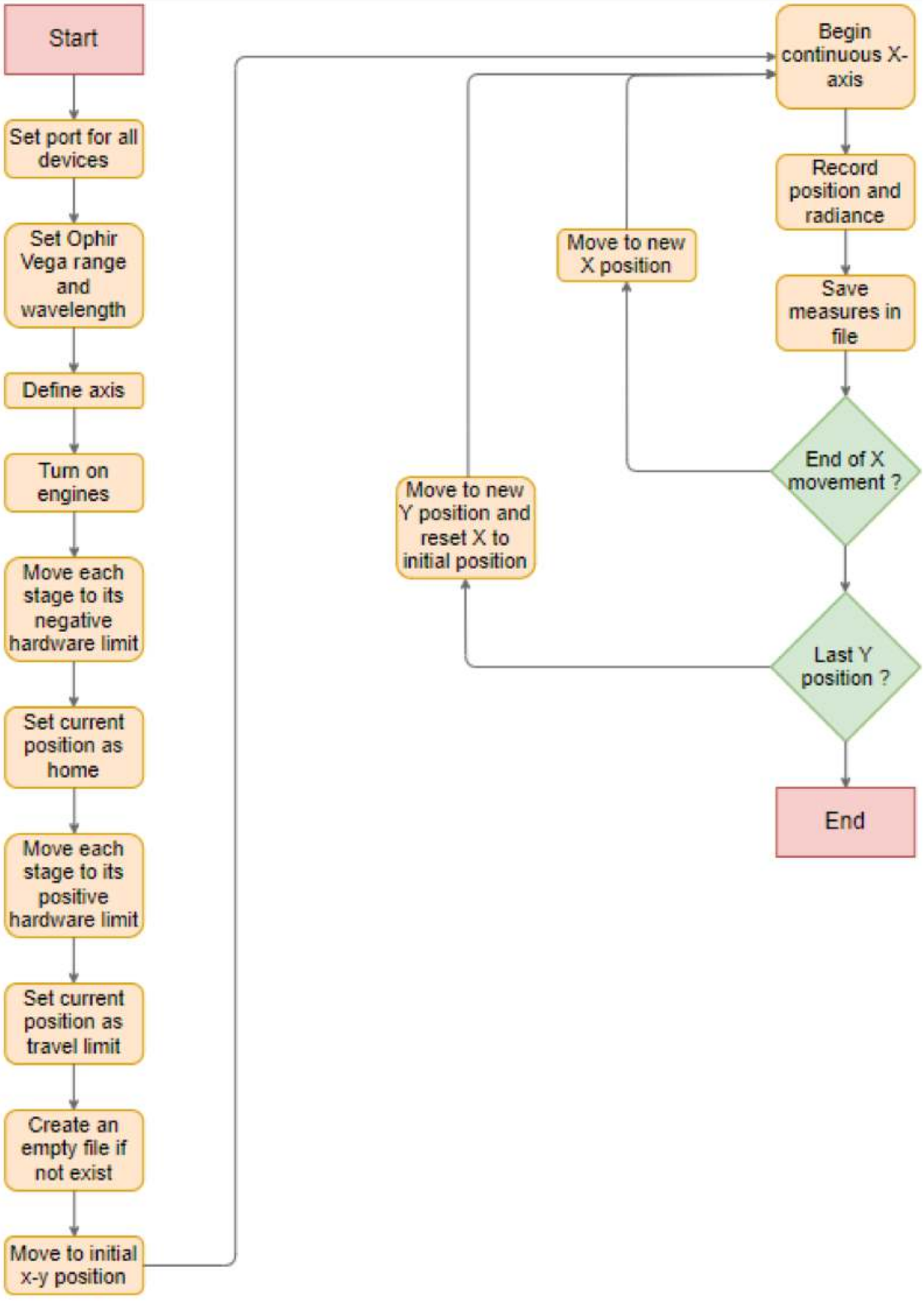

Figure 3.24: Flux diagram of data acquisition scan routine

Table 3.8: Lens diffusion test results

Laser beam = 4.85 mW = 100%							
Lens	Fresnel zone	Diffusion (%)				Reflection (%)	Total (%)
		m=-1	m=0	m=1	total		
1	3	8.5 ± 0.2	40.4 ± 1.2	10.2 ± 0.3	82.1 ± 2.5	7.2 ± 0.2	89.3 ± 2.7
3	2	-	67.5 ± 2	-	83.5 ± 2.5	7.0 ± 0.2	90.5 ± 2.7

- **Coarse Scan:** This scan was performed using the whole PD aperture, the purpose was measure how much light was diffused at a larger area than the fine scans. A 300×100 mm^2 (maximum travel limit of the axes) area was scanned.

- **Reflection scan:** This is a type of coarse scan where the laser is positioned between the lens and the XY scanner in order to measure the laser beam reflection on both surfaces of the lens. A 300×100 mm^2 area was scanned and both lenses were placed 350 mm away from the PD. In this scan the bean is shot at 3° incidence to avoid blocking the reflection of the lens flat side with the laser frame and stand.

To simplify the analysis of the scans it is assumed that the light is diffused only along the X axis i.e. perpendicular to the residual grooves of the lenses. To account for the height of the laser beam the Y axis columns of the grid are integrated into a single dimension.. This produces a 1D row of measurements on the X axis. The light diffused outside of the measurement range of the 2D scan is considered to be lost at wider angles. Figure 3.25 shows an example of a fine and reflection scan in 2D and in reduced 1D form.

3.9.3 Results of the localized diffusion experiment

The transmitted and reflected pattern of one Fresnel zone per lens was scanned: zone 3 (from center to edge) of L1 and zone 2 of L3. Figure 3.25 shows fine and reflection scan examples in 2D and simplified 1D plot. The result of both scans are illustrated schematically in fig. 3.26 and summarized in 3.8, these results clearly show how the beam intensity is progressively reduced after passing through each lens. To understand the angular dispersion provoked by each lens, the diffused pattern of L1 and L3 is shown in fig. 3.27 with the intensity converted as a function of angle and centered on the 0^{th} diffraction order.

L1 Produces an interference pattern with a beam core containing about 40% of the beam intensity. It has a $\pm 1^{st}$ diffraction order peaks at ≈0.07°which contain 8 to 10% of the total intensity. Higher diffraction orders can be observed in the logarithmic plot of the diffused pattern. A simple analysis using the diffraction grating equation $d(\sin\theta_m - \sin\theta_i) = m\lambda$ shows that the groove period d is $\approx$ 320 μm. Since this groove period is bigger than the radius of the fine diamond tool bite, it means it's a residue of the coarse tool bite (0.5 mm) milling.

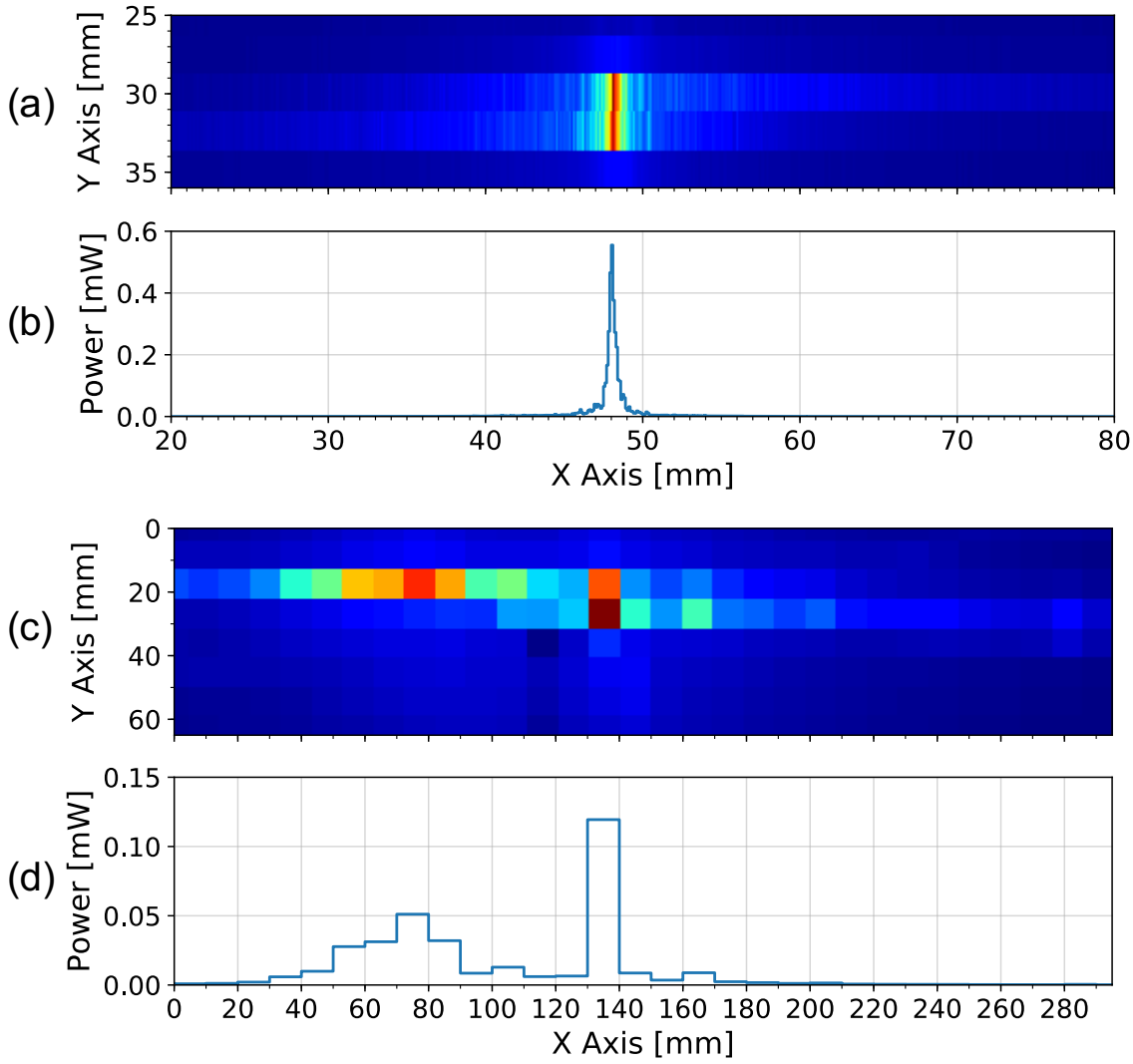

Figure 3.25: Plots of the scanned diffusion patterns produced by the Fresnel lenses. *(a):* Fine scan of L3, Fresnel zone 2 with a 0.1×3 mm^2 grid size. *(b):* 1D plot with integrated columns of plot (a). *(c):* 2D coarse reflection scan of L1 Fresnel zone 3. The reflections from each lens surface are visible, the laser stand casts a shadow between 110 and 120 mm in the X axis. *(d):* Integrated columns of plot (c), the beam reflected of the flat side of the lenses is narrower while the Fresnel zone reflected beam is broader due to diffusion.

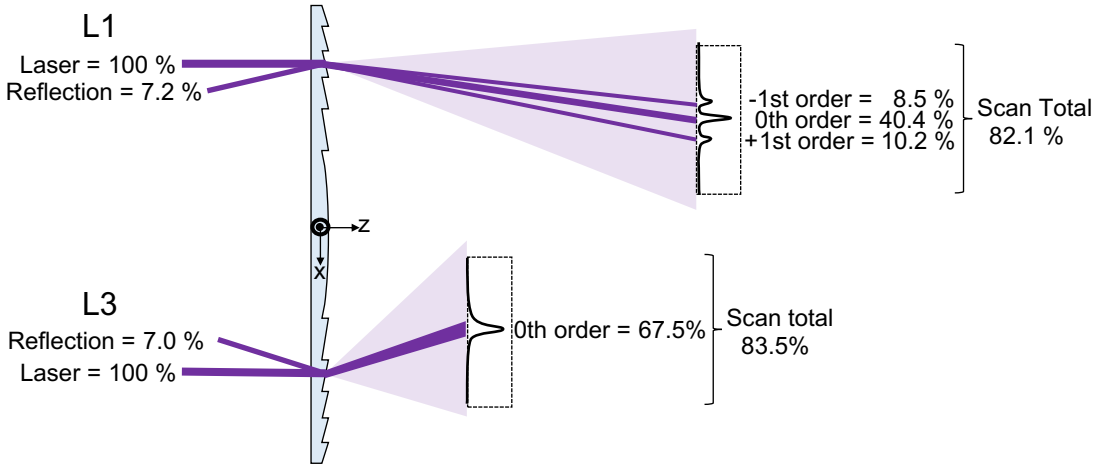

Figure 3.26: Schematic representation of the laser beam intensity branching ratio. *Top:* Distribution of L1 Fresnel zone 2, the pattern shows the 0^{th} and $\pm 1^{st}$ diffraction orders. *Bottom:* Distribution of L3 Fresnel zone 3, there is a single order with $\approx$ 60% of the beam intensity. In both cases about 7% of the intensity is reflected.

L3 produces a single lobe pattern with a core containing ≈68% of the beam intensity. It has a lower maximum compared to the L1 pattern and is spread over ±0.1°, the rest is scattered at higher angles. This pattern doesn't show diffraction peaks, however it was scanned at a closer distance (in the near field), approximately equal to the distance between L3 and the detector.

The reflection scans show that about 7.2% and 7.0% of the beam intensity are back-reflected by L1 and L3 respectively. If we integrate the measurements of the fine and reflection scans we get an intensity fraction of 89.3% for L1 and 90.5% for L3. The transmission efficiency for 405 nm in one 8 mm sheet of PMMA is about 92% (see fig. 3.4). Hence from the remaining ≈10% of intensity about 2% is absorbed and the rest is considered lost as it is diffused at very wide angles.

3.10 Model of the EUSO-Balloon optics

To model the optics taking into account the diffraction effects caused by small scale surface irregularities, it is necessary to know the surface profile at all spatial regimes and to use a physical optics model in order to propagate a simulated wavefront. Additionally, the sampling requirements for the microscopic surface structures demand a lot of computational resources and memory, making it complex to simulate large aperture optics.

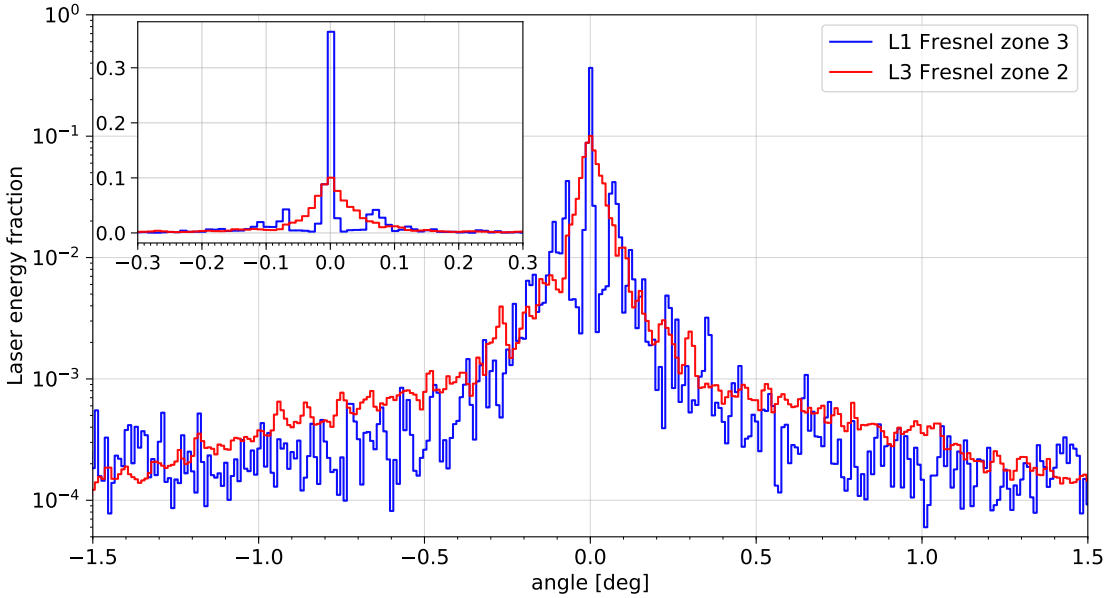

Figure 3.27: Diffusion pattern of the 405 nm laser beam after being transmitted through each lens, the measurement are re-sampled using 0.1°bins. *Top left:* Inset showing a zoomed portion in linear scale. *Blue:* Diffusion pattern of L1 Fresnel zone 3, two diffraction peaks are visible at $\approx \pm 0.07°$. *Red:* Diffusion pattern of L3 Fresnel zone 2, the scanned pattern shows a single lobe.

3.10.1 Diffusion ray tracing (DRT) model

To simplify and overcome the modeling constraints, the model used for the EUSO-Balloon optics consists of a ray tracing code that incorporates an empirical diffusion extension. The extension works by using the single photon interference effect. Let's say we have a diffraction grating, we shoot a laser through it and measure the intensity at the far field. The result would be the diffraction/interference pattern we're familiar with. Now lets say we shoot a single photon through the same grating and measure it's position at the same distance. We would observe the position of the photon but nothing else in particular. However, if we keep shooting photons at some point the same diffraction pattern formed by the diffracted laser beam would begin to emerge. The rate of photons arriving at a given position in the pattern is correlated by the relative intensity of the pattern at such position. Therefore, if we discretize the relative intensity of the diffraction pattern, then it can be considered as a discrete probability distribution. The probability of a photon arriving at a given position in the pattern is given by the relative intensity at such position. Using this principle, then the relative intensity of our discrete diffusion measurements can be used to randomly sample propagation angles. We can use these angles to trace individual rays and as more rays are traced, the observed pattern will begin to emerge.

Using this approach the diffusion can be simulated without knowing in detail the microscopic profile of the lenses. We only need to have a measured sample of the diffusion at one

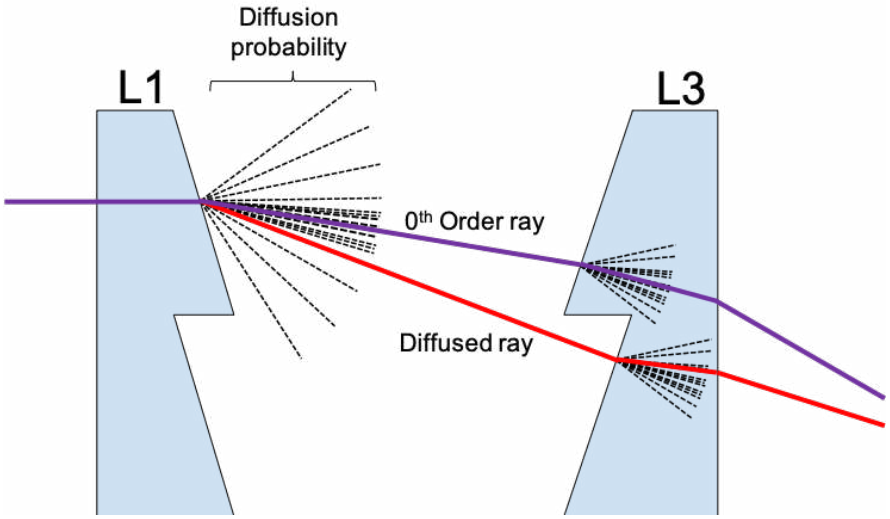

Figure 3.28: Principle of the Diffusion-Ray-Tracing simulation. The violet ray represents a refracted ray that corresponds to the 0^{th} order of diffraction. The red track represents one possible diffused ray, the offset angle with respect to the 0^{th} order is randomly drawn from the angular distribution of the diffusion measurements.

position in the lens. For this "Diffusion Ray Tracing" (DRT) model the diffusion of a single Fresnel zone per lens is extrapolated into all the other zones. This might not necessarily be representative of the whole lens but the main goal was to get a basic understanding the performance due to diffusion effects and obtain the best possible approximation.

The DRT model of the EUSO-Balloon optics works as follows:

1. Diffusion is assumed to occur only in the Fresnel zones. Therefore, in Air-PMMA interfaces on the flat side of the lenses the refraction angle is calculated and the ray propagated to the next interface.
2. In Air-PMMA interfaces on the diffusing (Fresnel zone) side of the lenses the refraction angle is calculated, this corresponds to the 0^{th} diffraction order angle. An offset angle is randomly drawn from the discrete distribution of L1 and L3 (from fig. 3.27), this angle is added to the 0^{th} order angle and then the ray is propagated to the next optical interface.
3. Each ray has a probability of being reflected, absorbed or scattered at a wide angle based on the intensity percentages of the experimental results. This stops the tracing and the ray is considered lost.
4. The tool peak rounding limit is implemented in the digital model of the lenses topography as seen in figure 3.20(c).

Figure 3.28 illustrates schematically the working principle of the DRT simulation.

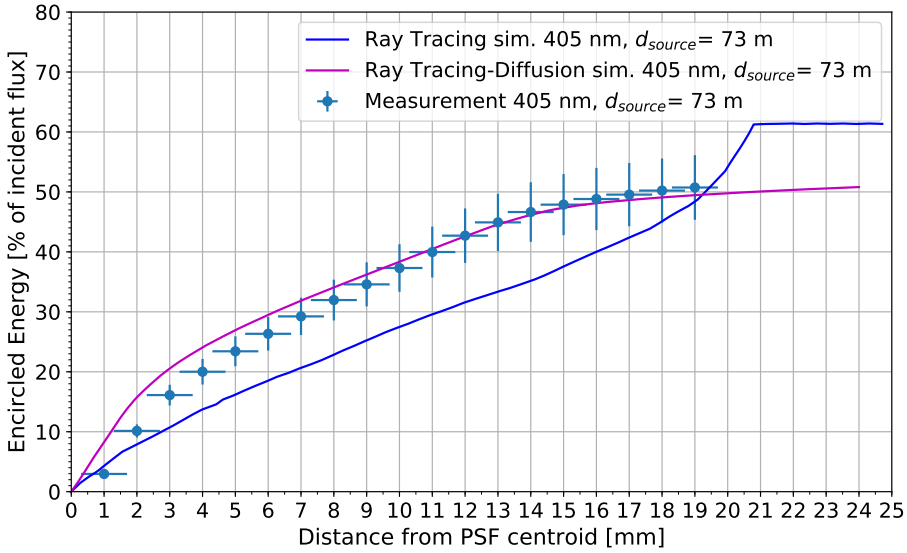

Figure 3.29: Encircled Energy plots of characterization measurements (405 nm wavelength at 0.1°incidence and 73 m away from the source) and the DRT and RT simulations

3.10.2 DRT Model Results

Figure 3.29 shows a plot comparing the characterization measurements against the DRT and RT simulations using a wavelength of 405 nm and incidence angle of 0.1°. Although there is some discrepancy at a radius lower than 7 mm the DRT model plot approaches more agreeably the profile of the measurement data, this was not possible with a pure RT approach which only simulates refraction and specular reflection. The residual discrepancy can be explained because the diffusion distribution is based only the measurements of one Fresnel zone per lens and interpolated into all other zones. This is a gross approximation and in reality we ignore if there are significant microscopic and macroscopic deviations of the numerical lenses with respect to the real ones.

If we compare the plots, the RT simulation has a lower efficiency up to a distance of about 19.5 mm and afterwards it surpasses the DRT and measurement plots and achieves a plateau at about 21 mm which means that all the transmitted light is contained at this point. This result seems confusing since it implies that the RT produces a less concentrated spot than the diffused measurements. This happens for two reasons, first we have to remember that the wavelength at the best focus in EUSO-Balloon is 365 nm, meaning that the 405 nm light is still converging, so it is out of focus and has a larger spot size. Second, figure 3.26 shows that a fraction of the light is diffused inwards (towards the center of the PSF) in the $+1^{st}$ diffraction order and outwards in the -1^{st} order of L1, then it's further diffused by L3. If we consider light incident at 0° and using the aid of a schematic depiction shown in figure 3.30,

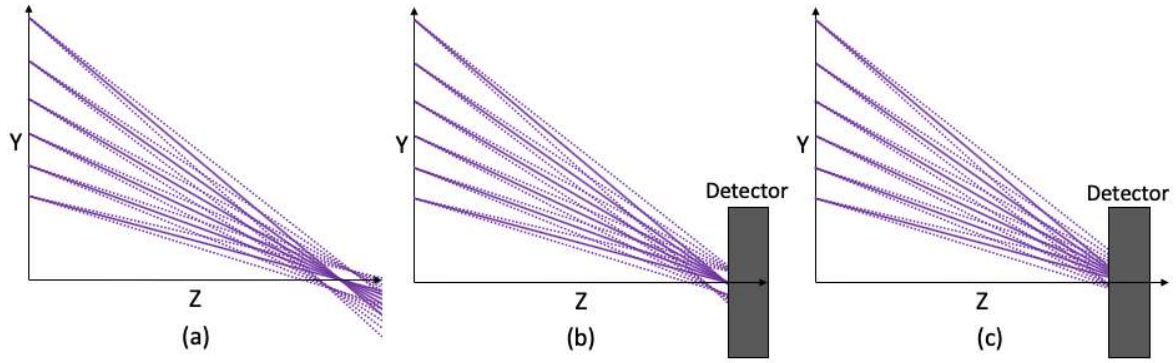

Figure 3.30: Effects of diffused light on the PSF of the optics. *a):* The $+1^{st}$ and -1^{st} diffraction order rays form different foci with respect to the 0^{th} order rays. *b):* If we place the detector at the best focus of the 0th order, the diffused light will form a halo around the PSF. *c):* If the detector is placed out of focus for a particular wavelength, the $+1^{st}$ order rays will be closer to the center than the 0^{th} order rays, resulting in more efficiency at a shorter radius compared to the pure RT approach.

	RMS spot size (mm)	Avg. efficiency in 9 mm diam.
Measurements	11	20.5 ± 2.2 %
DRT	10	21.5
RT	21	16.0

Table 3.9: Comparison of the EUSO-Balloon optics characterization measurements RMS spot size and average efficiency in 9 mm diam. of the four incidence angles against the DRT and RT simulation results. Only the 405 nm wavelength results are considered.

we can see in panel (a) that the $+1^{st}$ order light converges at a shorter distance than the 0^{th} order. Panel (b) shows the 0^{th} order light in focus on the detector, here the $\pm 1^{st}$ orders form a diffuse light halo around the PSF core. In panel (c) the 0^{th} order light out of focus on the detector, here it's evident that the $+1^{st}$ order diffused light is the most centered and thus it increases the efficiency at a shorter radius compared to a pure RT approach. On the other hand the light diffused outwards will either be further away from the PSF core or blocked by the exit pupil of the optics, leading to a lower efficiency at a larger radius.

Given the semi-empirical nature of the DRT model, the results could only be compared for the 405 nm wavelength, which is not the most significant in the optics configuration. Nevertheless, the DRT model results show a better agreement with the measurements, as shown in table 3.9. Therefore, the DRT model can explain the measured performance of the lenses for the 405 nm wavelength and shows that the diffusion effects caused by the fabrication features of the lenses are the culprit for the deviation from the expected performance of the EUSO-balloon optics.

3.11 Improvement of the Fresnel optics

It is clear that the surface quality of the Fresnel lenses plays an important part in the global performance of the EUSO-Balloon and SPB1 telescopes. To conclude the chapter we will review an improvement in production and post-production of the lenses that could lead to an improved optics performance and to meet the expected optical efficiency in future projects.

3.11.1 Optimization of manufacturing parameters

Although the diamond turning process is very precise and produces very smooth surfaces, the fabrication parameters and mechanical properties of the material can have an important effect on the finished product. The main parameters of the turning process include: the size of the tool bite, the spindle speed, the angle of the tool with respect to the surface (tool angle), the feed rate (i.e. amount of material traversed by the tool per unit time, typically in mm / min), the step over (material traversed by the tool per revolution of the spindle) and the depth of cut.

Research done Jiao and Cheng [89] has shown that the variation of certain parameters of the turning process of PMMA can produce diverse results in the surface roughness of PMMA samples. In their experiment they varied the tool angle and the step over of the tool while other parameters remained constant. They produced samples with a surface roughness varying from 8.7 to 79.5 nm RMS. One of the highlights of this work is the predominance of the step over parameter in the resulting surface quality. If the step over is too large, then the tooling cusps are more prominent since there is more spacing between each tool pass resulting in a bad surface roughness. On the other hand, if the step over is too short the chip formation of the cutting process will not be optimal due to the minimum chip thickness of the material. This results in chip not forming during each tool pass and accumulating until the minimum chip thickness is achieved. This changes the material cutting mechanism into rubbing and plowing and could produce vibrations in the tool that deteriorate the surface roughness. Therefore, to produce quality Fresnel optics in a future project, then some experimental work needs to be performed to optimize the fabrication parameters for each of the diamond tools used to cut the lenses.

3.11.2 Magnetorheological finishing

Magnetorheological finishing (MRF) is a deterministic polishing technique capable of producing complex and very smooth surfaces with a micro roughness below 1 nm RMS and a form accuracy below 50 nm [90]. The method consists in using a magnetorheological (MR) fluid, a polishing solution formed by abrasive and iron particles whose stiffness can be controlled in real time by manipulating a magnetic field.

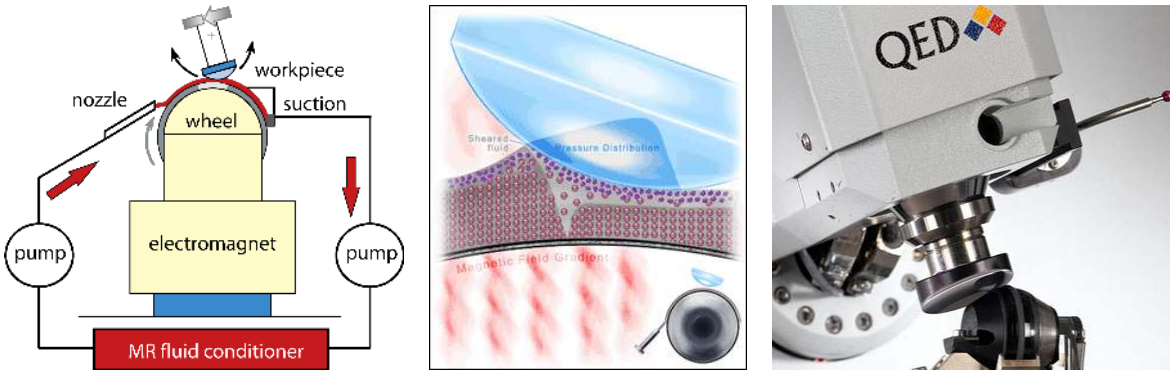

Figure 3.31: Magnetorheological finishing process. *Left:* Schematic of an MRF machine. *Center:* Picture showing MRF wheel polishing a workpiece. *Right:* MRF machine from QED Technologies 2016 QED Technologies Inc. polishing a workpiece [91]

The method works by feeding the MR fluid into a rotating wheel that transports the MR fluid. When the magnetic field is activated the iron particles align with the wheel while the abrasive particles are concentrated on the surface of the fluid; the so called "ribbon". Then, the work piece is immersed in the ribbon where the material removal process begins. The MR fluid is then recollected and recirculated. The left panel of figure 3.31 shows the schematic of a MRF machine, the center panel shows the working principle and the right panel shows a lens being polished by a MRF machine produced by QED Technologies Inc., the developer of the technique and main supplier of MRF machines.

The MRF method achieves excellent surface qualities highly suitable for the requirements of the JEM-EUSO optics. However, the effectiveness of the method is limited by the discontinous profile of the Fresnel lenses and the Fresnel zones becoming narrower at a larger radius from the center. As a consequence, the MRF wheel can't polish the entirety of a Fresnel zone due to geometrical restrictions and at a larger radius the Fresnel zones are so narrow (< 3 mm) that it becomes inviable to polish the surface. Therefore, although the method is effective, it is also limited to the innermost Fresnel zones where the geometries of the MRF tool and the workpiece allow to polish the surface.

Chapter 4

The EUSO-SPB1 campaign

4.1 Introduction

The very beggining of my PhD work started in a critical phase during the EUSO-SPB1 launch campaign, just a few months before the projected balloon launch. Participating in such a campaign was a very enriching experience and provided a lot of knowledge about how a small scale space mission is planned and developed. In this chapter I describe the work done before and during the balloon launch campaign of EUSO-SPB1, with a main focus on the activities performed regarding the optics of the instrument. It starts with the description of the characterization work of the optical system in which I contributed, the test campaign performed by my colleagues in Utah, the activities performed during the launch campaign in Wanaka New Zealand and the activities during the balloon flight.

4.2 EUSO-SPB1 optics characterization and end to end tests

The characterization of the EUSO-SPB1 optics was performed in the Colorado School of Mines (CSU) in Golden, USA. The Toulouse team collaborated in this task due to the previous experience in the characterization of the EUSO-Balloon optics. The goal of the optics characterization was to determine the best efficiency performance configuration for the balloon flight. This was achieved by optimizing efficiency of the PSF which required testing different optical component configurations and analyzing the results of each run. A detailed description of the characterization is given in chapter 3.

4.2.1 Utah calibration campaign

Following the optics characterization, the instrument went into an integration phase and later an experimental campaign in the Telescope Array site in Black Rock Mesa, Utah, USA. The work was coordinated by the CSM team and various members of the collaboration took part in the activities. The objective of the campaign was to perform an end to end field test of the integrated instrument to understand it's performance and capabilities. This section will focus on briefly describing the campaign aspects related to the end to end optics performance

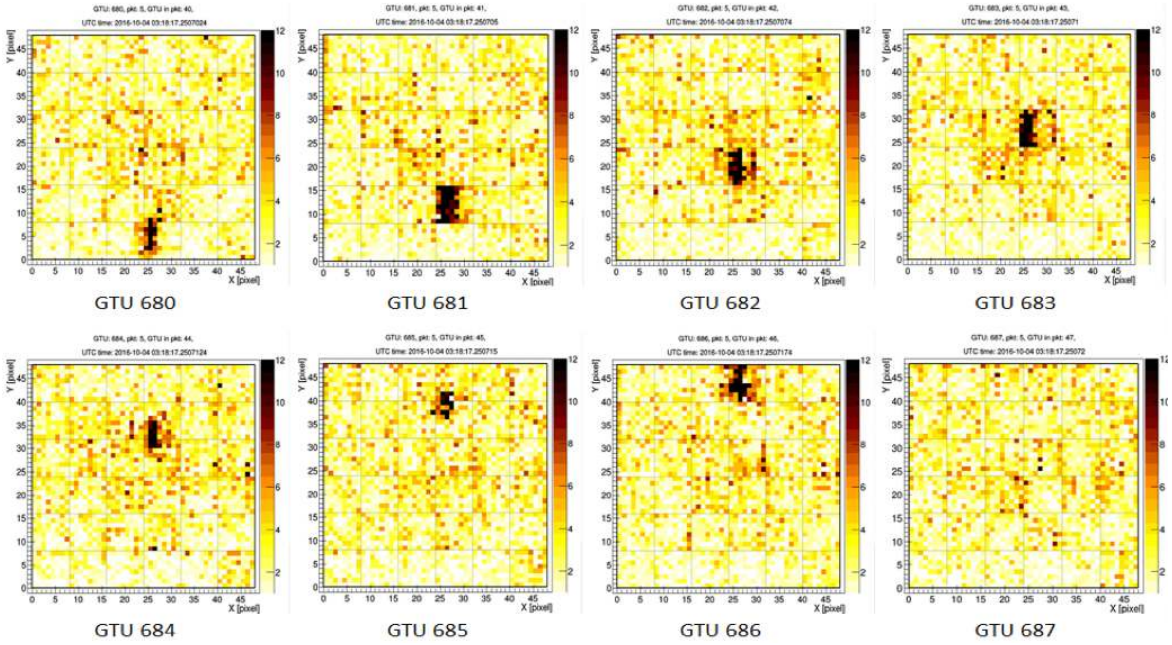

Figure 4.1: GTU frames of a GLS laser shot in the Utah desert. Each frame shows the scattered photons of the vertical laser track propagating across the FoV of the instrument. Plot from [94]

and differences between the two configurations. A more extensive detail of the work done and results obtained in the campaign can be found in [92] and [85].

4.2.2 Measurement of EAS like events

To test the capabilities and efficiency in detecting EAS like events, EUSO-SPB1 was tested with thousands of laser shots from the Central Laser Facility (CLF) located in the Telescope Array site [93] and the Global Light System (GLS), a mobile laser platform developed by the CSM to produce EAS like signatures with well known characteristics [85].

The instrument was first tested with the CLF using the 2L and 3L configuration. The CLF laser has a wavelength of 355 nm, it fires 300 vertical shots every 30 minutes with an energy of 3 mJ and is located 21 km away from the instrument. The laser shot from CLF helps to determine the observation capabilities of the instrument using a distant source. Figure 4.1 shows a typical laser event as seen by EUSO-SPB1 in 2L configuration, each GTU frame shows the scattered photons of the laser shot propagating across the field of view. Figure 4.2 shows the brightness distribution measured by the two and three lens configuration using 272 and 291 CLF shots respectively. The distributions show a mean value of 3269 and 1304 photon counts for the two and three lens scenario respectively.

The telescope was also tested with the GLS system prototype, this mobile laser platform

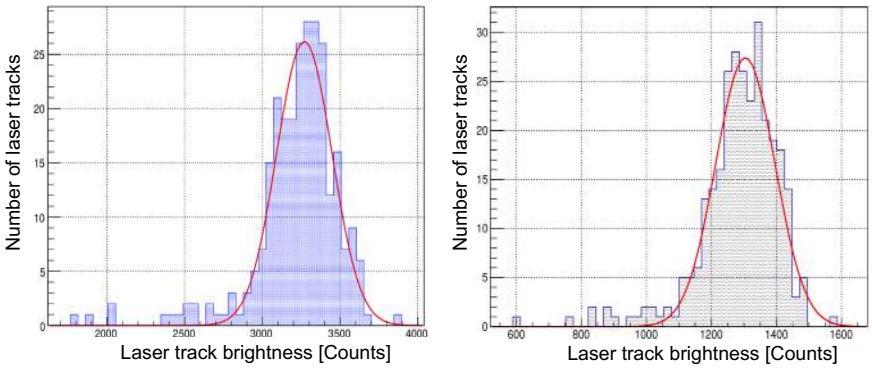

Figure 4.2: Number of laser tracks as a function of the laser track brightness. The 2 lens configuration shows a higher count distribution depending on the number of tracks.

is designed to provide a known signature based on a given energy input, this makes the system useful to mimic EAS events and test the response of the system for an air shower of a given energy. The GLS was placed 24 km away from the telescope, it is steerable allowing more flexibility for the track geometry scenarios and it generates UV light tracks (355 nm) with an energy per pulse ranging from 0.5 mJ to 90 mJ. This energy range corresponds to an EAS of 10^{17} to 10^{20} eV, this correspondence is based on the intrinsic luminosity of the photons scattered out of the laser beam compared to the photons produced by an EAS. The GLS capabilities allowed to test the trigger efficiency of the instrument for both configurations and determine the energy threshold of the instrument. Figure 4.3 shows the trigger efficiency results of both configurations as a function of the laser energy. The results show the performance of the two lens system which achieves a 100% trigger efficiency at ≈1.5 mJ compared to the ≈2.5 mJ of the three lens system. The results from these tests were compared with simulations and showed that the laser energy of about 0.8 mJ which achieved 50% trigger efficiency in the tests is equivalent to an EAS of $\approx 3\times10^{18}$ eV, assuming an EAS with an inclination of 45°observed from an altitude of 33 km [64]. Overall the results show that the two lens configuration, despite having a larger spot size, is the better performing in terms of optical throughput and trigger efficiency. This configuration was selected for the EUSO-SPB1 flight.

4.2.3 Field of View determination

The FoV of the instrument was determined using two different methods to corroborate each other results. The first one consisted in observing a reference bright star and measuring the change in position from edge to edge of the FoV over time, because the stellar motion is known precisely, it becomes easy to convert the elapsed time into an accurate field of view. This process was repeated for five stars and gave an estimated FoV of 11.10±0.15°

The second method consisted in shooting a laser in a sweeping motion along the FOV in 2°intervals. The laser angle has a precision of 0.2°and the laser position is known within

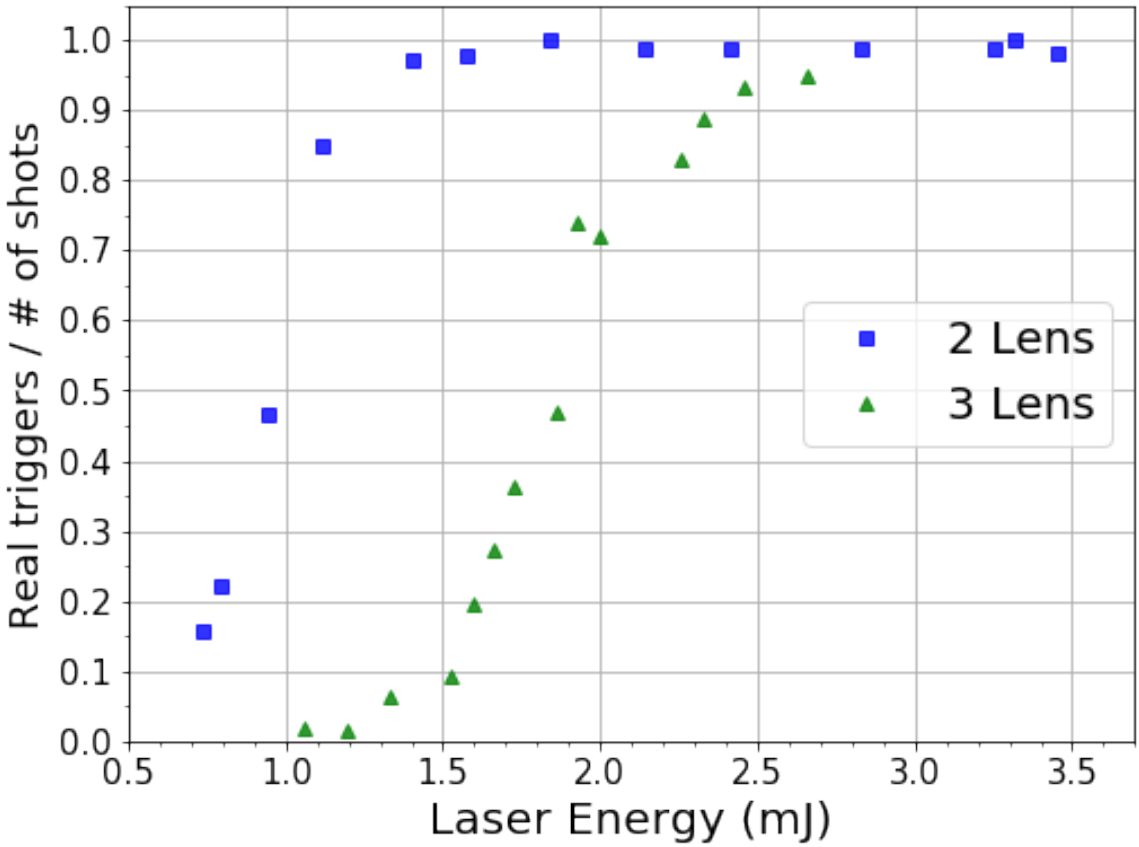

Figure 4.3: Trigger efficiency of EUSO-SPB1 as a function of the laser energy, 100 shots were fired per energy setting. The two lens configuration achieves almost a 100% efficiency at about 1.5 mJ demonstrating a better performance compared to the three lens configuration

Table 4.1: Mean latitude ranges for balloons launched from Wanaka as a function of flight duration. From [96]

Flight duration	**+30 Days**	**+ 60 Days**	**+100 Days**
Average Latitude Range	-34.5 – -58	-33.5 – -60	-29 – -65

GPS uncertainties. This method provided a FOV of 11.2±0.1°which is consistent with the previous method.

4.3 Wanaka balloon launch campaign

After the end of the calibration campaign and final validation tests required for the instrument, it was shipped to New Zealand (NZ) for the balloon launch campaign. The balloon base was installed at the airport of Wanaka, a city in the south island of NZ and one of the two locations selected for NASA's ultra long duration balloon (ULDB) program. EUSO-SPB1 was the third balloon project to be launched from this location, as the city had already been the base for two other projects: an engineering flight conducted by NASA to test the SPB and the Compton Spectrometer and Imager (COSI) instrument [95]. These flights had a duration of 32 and 46 days respectively which gave EUSO-SPB1 high hopes for a long duration flight.

Wanaka was selected for it's key characteristics which make it a very suitable location for the ULDB program. At it's mid-latitude location (≈45°S) the austral fall/winter stratospheric winds produce a stable clock-wise circulation pattern from march through august of each year. The balloon trajectory can have latitude excursions up to +15/-20°depending on the flight duration (see table 4.1) and a complete circumnavigation can take between 4 to 20 days depending on the time of the year [96]. Moreover the low population density and proximity to the ocean, make Wanaka a relatively safe location for balloon launch and flight operations. For these reasons NASA made an investment to continue it's Wanaka operations, in early 2017 it signed a 10 year lease with the Queenstown Airport Corporation (which manages the Wanaka airport) and acquired a plot of land for the construction of a new balloon launch pad which was used for the first time for the EUSO-SPB1 launch [97], the launch pad is shown in figure 4.4.

During the campaign the balloon operation services are provided by the Columbia Scientific Balloon Facility (CSBF), an entity under the sponsorship of NASA which is headquartered in Palestine, Texas but also operates other balloon launch facilities around the world, including Wanaka [98]. The CSBF team provided support and work space to the science team, it took care of the gondola, the telemetry and the balloon launch and flight operations.

Figure 4.4: Balloon launch pad in the Wanaka airport

4.3.0.1 NASA's Super Pressure Balloon

The Super Pressure Balloon is the harbinger of NASA's ULDB program which aims at performing stratospheric balloon flights carrying a heavy payload of ≈2700 kg up to a constant altitude of 33.5 km for a duration of 100 days or more. The program was established in 1998 and has since then performed many deployment tests and flights necessary for the maturation of the SPB technology [99]. The SPB is a pumpkin shaped balloon with a mass varying between 2400 and 2800 kg. It's skin is made with a layer of 0.038 mm low density polyethylene with UV shielded polybenzoxazole (PBO) and load bearing members which act as longitudinally aligned tendons that separate the balloon into sub-sections called gores. Upon reaching float altitude the balloon's internal pressure reaches 180 Pa. The super pressure balloon size then reaches widths from 115 to 130 m wide, it is 70 to 80 m tall and the total volume is between 532,000 and 740,000 m^3 [96]. Figure 4.5 shows a fully inflated super pressure balloon.

Other components of the SPB system include the gondola structure and the parachute. The gondola is a steel and aluminum exoskeleton which holds the instrument. It's width and length can range between a 1.5 to 3 m and it's height between 3 and 8 meters. The gondola is equipped with ballast hoppers containing between 500 and 700 kg of steel shot and silica sand which can be released in order to control the ascent and maintain a stable altitude. In total the gondola has a mass that ranges between 800 and 1800 kg. The parachute assembly contains a nylon canopy of 37 to 40 m in diameter. An aluminum coupler that contains small explosive charges used to separate the parachute from the gondola. The coupler is connected to a steel cable ladder of 26 m long which in turn is connected to a coupling device linking the flight train to the gondola. All these components amount to a total mass ranging between 400 to 450 kg. The complete flight train is shown in figure 4.6

Figure 4.5: Fully inflated super pressure balloon, the vertical lines running from top to bottom of the balloon are the PBO tendons and the space delimited between each one is a gore.

4.3.1 Campaign Activities

During the campaign the scientific instrument and gondola were integrated to test the complete flight payload and give it a green light for launch. Even if the instrument was thoroughly tested and characterized in Utah, it had to be re-assembled and retested. Any remaining issues had to be resolved to assure the correct operation and smooth integration with the rest of the flight train. In this section I describe my activities during the campaign. Besides cleaning and integrating the optics, I participated in most of the activities of the science team to reach "launch ready" status.

4.3.1.1 Optics cleaning

The tight biosecurity laws of New Zealand require that all shipping containers are fumigated to prevent any form of unwanted organism from entering the country and affecting the agriculture and biodiversity. This resulted in contamination of the lenses with residues of the fumigation agent. To prevent these residues from affecting the performance of the optics, the lenses had to be carefully cleaned by using a procedure similar to the one used to clean the lenses of EUSO-Balloon [81]. The procedure to wash the lenses is the following:

- The lenses are blown with nitrogen gas to de-dust the lenses as much as possible
- A basin larger than the lenses (1x1 m^2) is prepared and filled with deionized water.

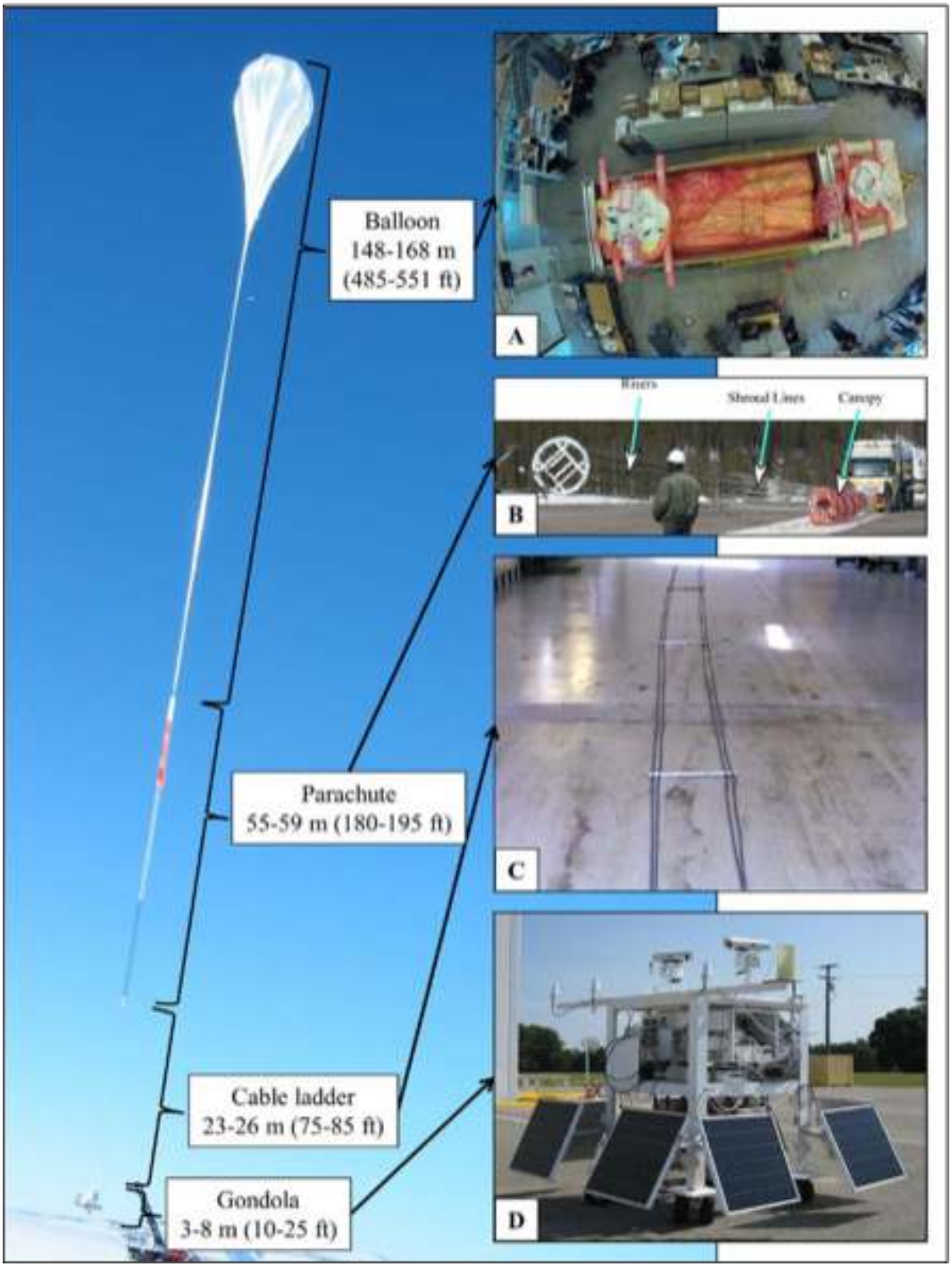

Figure 4.6: Flight train of the SPB system. *A)* The balloon furled inside it's box. *B)* The unfurled parachute and it's components. *C)* The steel cable ladder. *D)* The gondola structure, including solar panels and telemetry instruments

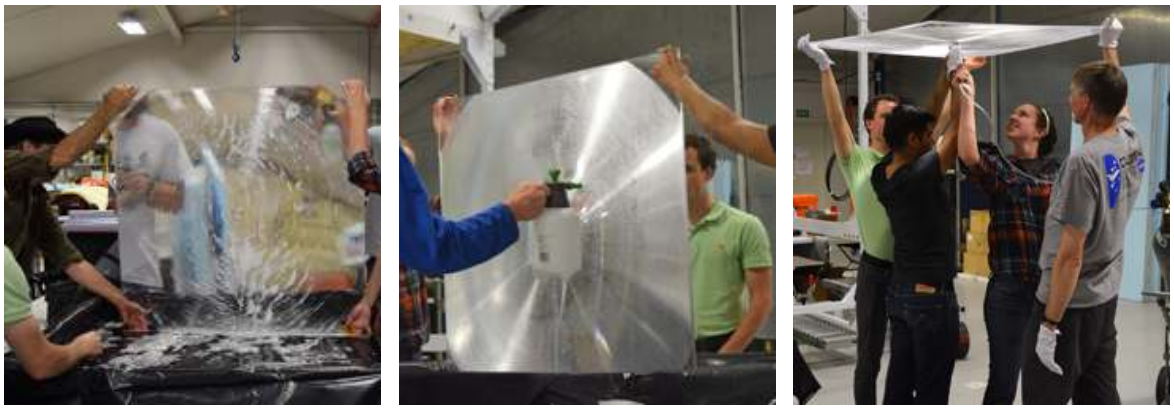

Figure 4.7: Cleaning of the EUSO-SPB1 Fresnel lenses. *Left:* The lenses being removed out of the basin with the cleaning solution. *Center:* The lenses being sprayed with water to remove excess foam. *Right:* Blowing the lenses with nitrogen to remove excess residues and humidity. Credits for all images: R. Gregg [100]

- The industrial detergent Liquinox® is added to the water to create a cleaning solution. Although the manufacturer recommends a 1:100 solution this was found to be extremely foamy and after some tests it was found that 0.1:100 solution was enough for the task.

- Once the water/detergent solution was prepared each lens was submerged in it and left inside for about five minutes. Then the lenses are shaken to remove lose particles. It's important to not leave the lenses too long in the solution to prevent swelling of the PMMA.

- The lenses are carefully removed from the basin and held up at least two people. Care was taken to prevent further contamination or damage by holding the lenses only from the corner edges which are not milled.

- A low pressure small water pump is used to spray deionized water on the lenses and remove foam residues, this is done until there is no more foam visible and the lenses look clear.

- The lenses are blown again with nitrogen to remove any remaining residues and moisture.

- The lenses are left to dry by placing them in a safe upright position.

Once the flight lenses were cleaned, they were installed in the optical box and sealed to prevent further contamination from the environment. Figure 4.7 shows some pictures of the lenses being cleaned during the launch campaign.

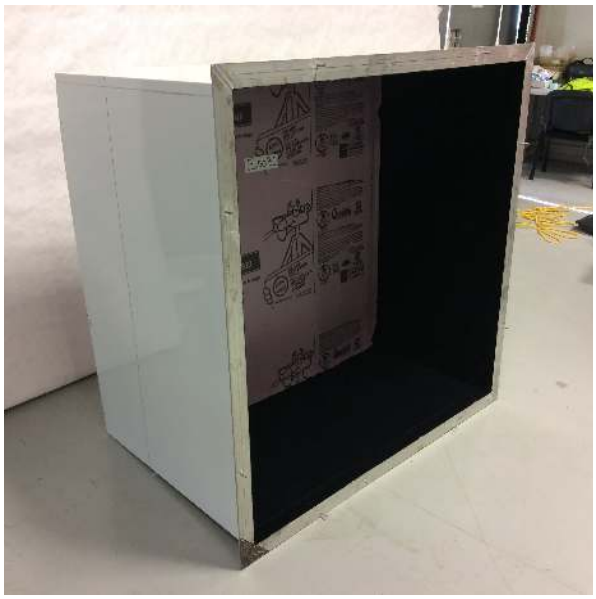

Figure 4.8: Detachable baffle used on the EUSO-SPB1 optics. It was made of a similar length to the section of the optics box that was trimmed. The installed baffle can be seen in fig. 4.9

4.3.1.2 Re-baffling of the optics

The mechanical structure of EUSO-SPB1 is the same box used to house the optics and electronics of EUSO-Balloon. However, as the gate of the hangar in Wanaka was not tall enough to allow passage of the entire instrument, the baffle had to be trimmed. Cutting the baffle meant that the front lens was more exposed to stray light from angles larger than the FOV. I dimensioned a new detachable baffle (shown in figure 4.8) which was built by the CSM team. It was be attached to the rest of the instrument every time it was tested outside of the hangar and for the launch (figure 4.8).

4.3.1.3 Flat Field Correction

Flat fielding corrects the non-uniformities of the optics and pixel to pixel variations to obtain a more uniform (flat) pixel variations. It is done by imaging a uniform light source with the telescope at close range. EUSO-SPB1 was flat fielded on two occasions: first during the test campaign in the Utah desert and second during the balloon launch campaign in Wanaka.

The flat fielding in Wanaka was done by hanging the telescope from a crane and placing it 5 m above a white screen made from Tyvek. A 365 nm LED was placed at the center of the L1 spider frame to emit light pulses which illuminate the Tyvek screen and then are diffusely reflected (see figure 4.9). The LED pulses were emitted at different intensities covering the dynamic range of the instrument. The frames were taken at four angular positions by rotating the telescope in 90° intervals, i.e. four different positions. The flat field frame is computed

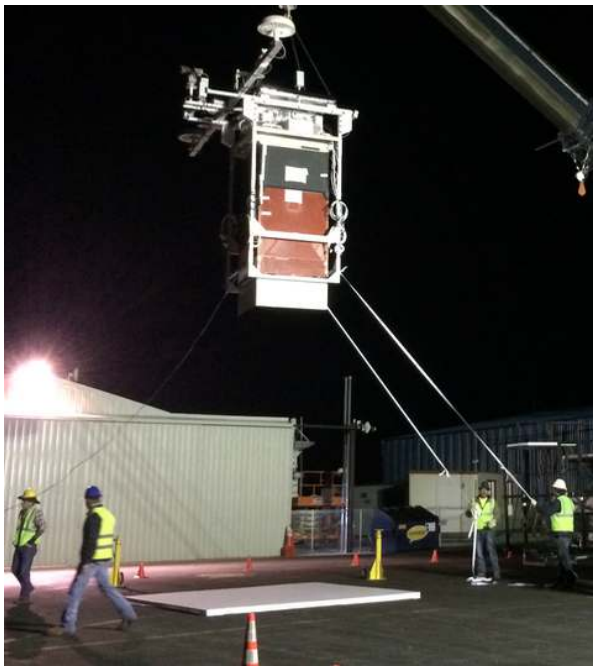

Figure 4.9: EUSO-SPB1 Flat fielding procedure at the Wanaka airport. The Tyvek screen is below the EUSO-SPB1 telescope pointing downwards.

by:

$$FF = \frac{1}{4}\sum_{i=1}^{4}\frac{F_i}{F_{i\ max}} \tag{4.1}$$

Where, FF is the flat field frame and F_i are each of the frames taken at each position. The flat field correction on a data frame is then given by:

$$F_{FF} = \frac{F}{FF} \tag{4.2}$$

Where F is any data acquisition frame and F_{FF} is the frame corrected by the flat field. In practice flat fielding a single GTU frame has little impact on the image, but it becomes more significant when applied to the integrated counts of one or multiple data packets.

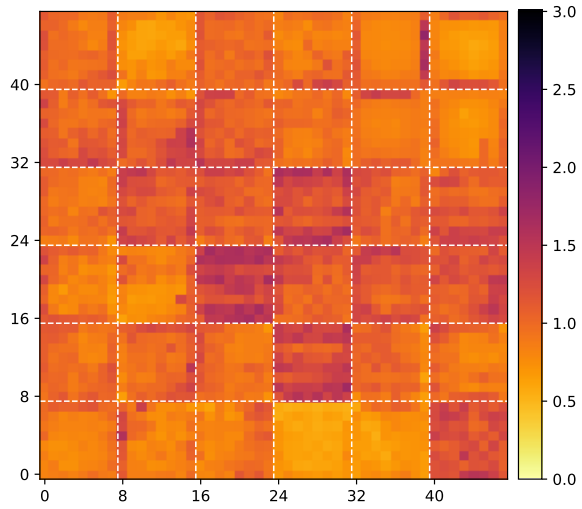

Figure 4.10: Flat field frame of EUSO-SPB1

4.3.2 Launch preparation

4.3.2.1 Compatibility tests and launch readiness review

The compatibility test, also called "hang test" (because the flight payload is suspended from a crane) is a test and milestone necessary to achieve the flight readiness status for the mission. It involves the science team and the CSBF technicians, both in Wanaka and in the operations control center in Palestine. The test, shown in figure 4.11, consists in testing the complete flight payload to ensure that the balloon and science instruments are fully compatible and working according to specifications and to verify if the telemetry chain is reliable.

Once suspended from a crane, the payload is completely wired up as if it was ready for flight. During the test the team verifies if the telescope and it's subsystems are capable of taking data and are compatible with the gondola instruments, if the payload is capable of sending and receiving information to and from the operations center through relay satellites, and if the payload is self-sufficient energy-wise Also during this time the launch technicians figure out the mechanical details for attaching the payload and determine the amount of ballast appropriate for flight. The test can take a whole day since it involves going through tedious procedures, checking many systems and fixing minor problems that could show up. Once every step in the is completed and no major issues are identified during the test, then the payload is one step closer to be launch ready.

After the compatibility test, the last step is to conduct a launch readiness review meeting in order to verify that the test was correctly performed and that there are no major issues that could hinder the launch and flight. The EUSO-SPB1 compatibility test was successfully performed the 23rd of march 2017. The payload declared flight ready the next day. This event was a milestone for the mission and the collaboration. From this point onward the

Figure 4.11: Hang test of EUSO-SPB1. The complete balloon payload (Instrument and Gondola) is integrated and hanged in order to be thoroughly tested and assess the launch readiness of the instrument.

mission enters in a phase with a new type of uncertainty as appropriate meteorological and safety conditions are necessary for launch. This can take days or months. The next section describes the process conducted to find a suitable day to attempt the launch.

4.3.2.2 Flight safety risk Assessment

Once the instrument is declared launch ready, the mission has to go through a flight safety risk assessment procedure in order to evaluate if the flight can be conducted within an acceptable risk margin and hence, if a launch will be attempted the next day. Every morning, the NASA team conducted a briefing to inform whether the following night would be a "Show" or "No show". This means that the teams show up to prepare for launch or not. To evaluate the risk the NASA team uses models that take into account the weather, wind conditions, payload weight and balloon inflation to predict the balloon trajectory. This allows to evaluate the overall risk that the balloon (and it's heavy payload) poses to the local community and environment in case of an aborted launch/flight. This risk is parametrized by dividing the map of the area into a squared grid and assigning a risk score to each element of the grid that depends on various factors such as the population density. If the balloon flies above a grid square then it's score is accumulated in an overall risk score. Moreover, if the balloon flies very slowly over a particular zone the risk is increased. If it becomes fully inflated (super pressurized) then the risk is increased even more, because at this point all the balloon joints are stressed uniformly for the first time and there is the small possibility of failure. If the risk score is above a threshold of $100/10^6$ (100 per million) then the verdict is a "no show", otherwise it's a "show". This result is under the discretion of the safety officer.

Ideally, a swift ascent towards the coast, flying above non or sparsely populated areas is desired, since this would result in a low overall risk. In the case of a "show", then the launch team and the science team would begin preparations that same night in order to have the instrument gondola and balloon ready for a possible launch the next morning. Unfortunately, having everything ready does not guarantee a launch, it is very common perform several launch attempts before a successful launch. In total eight attempts were made to launch EUSO-SPB1, the first seven attempts were called off due to unfavorable weather, a high risk trajectory or mechanical problems. The eighth attempt was successful. A list of the attempted launches and reasons for calling them of are listed in table 4.2.

4.3.2.3 EUSO-SPB1 flight operations shifting

Initially the most optimist expectation for the flight duration was 100 days. Such a long flight required a tight planning and work force to have the instrument under surveillance at all times. Certain members of the collaboration were trained to operate the instrument. These "experts", took the role of training other members in basic operations of the instrument in order to become "shifters" and a 24/7 shifting schedule was set up. The shifters task consisted

Table 4.2: List of launch attempts for EUSO-SPB1 and reasons for failed attempts

Attempt	Date	Comments
1	07/04/2017	Scrubbed for mechanical issues with the crane and risky trajectory.
2	08/04/2017	Show was planned but canceled due to remaining issue with the crane.
3	09/04/2017	Scrubbed due to high winds and chance of precipitation.
4	16/04/2017	Scrubbed due to weather and safety issues.
5	17/04/2017	Scrubbed due to wind trajectory reversal.
6	21/04/2017	Scrubbed due to high low-level winds.
7	22/04/2017	Scrubbed due to safety concerns over the trajectory.
8	24/04/2017	Balloon launched.

in monitoring the overall status of the instrument, change the operation mode of the detector when starting and stopping observations. They would check and report high level alarms of the instrument and if necessary call an expert on duty to help solve any problem that arose during flight. More delicate tasks like rebooting the instrument and changing flight settings were done only by experts. Since the JEM-EUSO collaboration had members all around the world, it was convenient to set up a shift schedule where the shift was handed over from one continent to another. This way the shift was performed during the morning to afternoon in all locations. In Europe, Toulouse took the shifting responsibility of the French part of the collaboration. Ground stations were set in Golden in the United States; Tübingen, Toulouse and Turin in Europe; and Wako in Japan.

The most interesting shifts were definitely in Europe. New Zealand is the antipode of western Europe so during the shifts of European ground stations it was night at the balloon position. Normally at the start of a shift it was already dark but the observations could only begin after moonset because the background light was still too high and dangerous for the instrument. The background light was monitored with two PD placed next to the PDM. They were set to maintain an artificial reading threshold if the background was too high. Once the PD readings started to descend it was the signal that the ideal darkness conditions were approaching. As shifters we had to choose the appropriate moment to start the observation mode. Likewise when the twilight was approaching we had to prepare to make the transition into "day mode", otherwise we risked burning instrument. A safe approach was to perform the transition just before Nautical twilight. Typically the command is relayed almost instantaneously to the instrument. However, sometimes it could take up to a minute so some precaution was prudent.

4.3.3 Balloon Launch and flight

EUSO-SPB1 was successfully launched the 24th of April, 2017 at 23:51 UTC. It performed a swift and almost vertical ascent and slowly drifted off towards the north-east and arrived

Figure 4.12: Flight path of EUSO-SPB1. The balloon flew for 12 days before the termination of the mission. The complete payload splashed down in the pacific ocean almost 400 km away from the Easter Island.

at the east coast of the south island of New Zealand. The first two days of flight showed a very stable altitude, however upon the start of the third night the balloon experienced an altitude loss which indicated some sort of problem. To compensate for this the SPB operators released ballast and the balloon regained the normal flight altitude which remained constant throughout the day. However, upon the arrival of the fourth night there was again an altitude loss which was only aggravated the following nights reaching the minimum flight altitude of about 17 km on the sixth night. At this point it became clear that the balloon had a leak it was kept afloat by the periodic release of ballast. After the twelfth day of flight the gondola had very little ballast left and the instrument was still very far from south America to attempt a descent over land. Due to the circumstances and following NASA's protocol it was decided to terminate the mission and an oceanic landing procedure was started. The mission was then concluded on May 6th, 2017 at 3:40 UTC and EUSO-SPB1 splashed down on the pacific ocean, about 400 km from Easter island. Figure 4.12 shows the flight path of the instrument from the launch until the splash down.

Chapter 5

Data analysis of EUSO-SPB1

5.1 Introduction

The EUSO-SPB1 mission flew for 12 continuous days, with multiple altitude excursions in the stratosphere before being terminated due to a leak in the SPB. Despite this setback about two thirds of data ($\approx$ 60 GB) were successfully downloaded and ready for analysis. The overall data analysis is not only concerned with finding EAS candidates, but also studying the night-time emission of earth, the environmental factors that affect the instrument's performance (such as cloud cover) and proving the capabilities of the telescope. This effort was guided through an analysis group formed within the collaboration with the purpose of providing a platform to present analysis methods, results and updates as well as discussion between team members and valuable feedback which was helpful for improvement.

In this chapter I present the method used to analyze the flight data and its results. The preliminary analysis of the data didn't produce EAS candidates by using already developed offline triggers. Therefore, our method is motivated by the need to understand what kind of events are present in the triggered data, to understand their spatial and temporal features, catalog them and potentially find EAS candidates from the database of extracted events. Our method is an exploratory analysis that uses a mixed approach consisting first in a visual inspection and manual categorization of the data in order to provide the feedback necessary for the development of an automated method capable of processing all the flight data.

We start the chapter by briefly reviewing some of the instrumental aspects of the flight that are directly involved with the quality of data taking. Then the analysis method is presented followed by the results. We then proceed to discuss the results.

5.2 Instrument flight performance

5.2.1 Balloon performance

Figure 5.1 shows the altitude profile as a function of time and the saved and downloaded data before the termination of the mission. The first two nights of flight showed a smooth

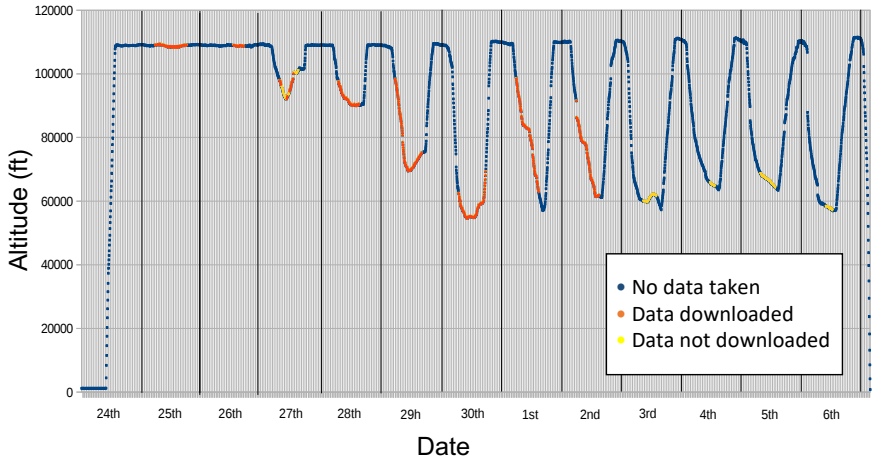

Figure 5.1: Flight altitude profile of the balloon-craft as a function of time. Points in orange and yellow represent observations performed by the instrument. Orange points are downloaded data and yellow ones are data that could not be downloaded due to malfunction. Plot by S. Bacholle.

and stable altitude. However, during this time the PDM was not fully operational since some ECs weren't active, as described in the next section. Starting on the third night a small altitude loss is seen and on the following days the balloon starts to descend more steeply. This was caused by a leak and at this point the balloon was kept afloat by dropping ballast from the gondola. The effect caused by the excursions in altitude results in a variation of area projected by the FoV and volume of atmosphere monitored. Hence, lower altitudes results in a smaller volume of atmosphere monitored and hence lower chances of detecting an event.

5.2.2 PDM Performance

Early stages of the flight were affected by ECs that weren't properly functioning. It's not clearly understood what were the underlying causes, but some corrections performed remotely and power cycling of the instrument solved the issue. Figure 5.2 shows the number of working ECs during the flight. During the first day the instrument ran mostly with 2 ECs, the second day the situation improved achieving up to 7 ECs and from the third day onwards all ECs were functional most of the time, with some occasional setbacks, particularly on the third day.

5.2.3 Trigger Performance

EUSO-SPB1 provided for the first time the opportunity to test in flight a First Level Trigger (FLT) logic comparable to the one envisioned for JEM-EUSO. Before EUSO-SPB1 the FLT was only tested offline in simulations, data from other projects (EUSO-Balloon, EUSO-

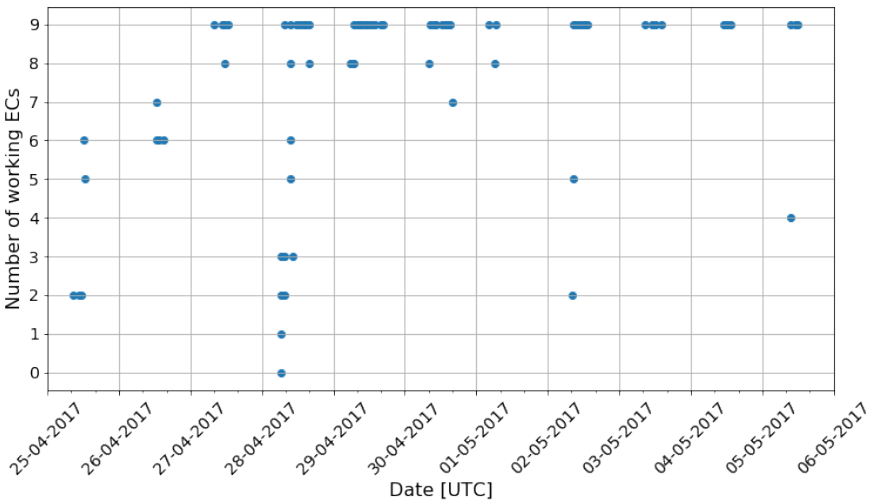

Figure 5.2: Active elementary cells during the flight

TA) and experimental campaigns on ground. All the flight data was triggered[1] therefore understanding the trigger performance during flight is also important for understanding the observed events in the data. The FLT is explained in sec. 2.1.6.1

The trigger rate and average count per pixel during the flight in different configurations can be seen in figure 5.3 [64]. During the first three days of the flight (P=0, R=0) the trigger rate was typically between 1 to 10 Hz/EC (The JEM-EUSO requirement) with some peaks above 10 Hz, this initially high trigger rate and other peaks during the flight are attributed to electronic disturbances in the top right EC and interference with the SiECA instrument adjacent to the detector (see sec. 2.2.2.1). After shutting down SiECA and a change in configuration (P=1, R=1), the trigger rate was significantly lowered until it reached levels of <1 Hz/EC for the remainder of the flight. Additionally, the trigger was tested for one day using a configuration optimal for JEM-EUSO (P=4, R=2) obtaining similar trigger rates below 1 Hz/EC, unfortunately the data saved using this configuration could not be downloaded.

5.3 Data Structure

The data of EUSO-SPB1 and other EUSO projects is encoded in the ROOT format, a data analysis framework developed by CERN (Conseil Européen pour la Recherche Nucléaire)[2] commonly used in high energy physics experiments [101]. The data is acquired in nominal runs of 120 seconds. Each data file contains thousands of entries, where each entry corresponds to one Gate Time Unit (GTU). Each entry contains the photon count per pixel, as well as

[1] With exception of periodic files used to monitor the status of the instrument
[2] European Organization for Nuclear Research

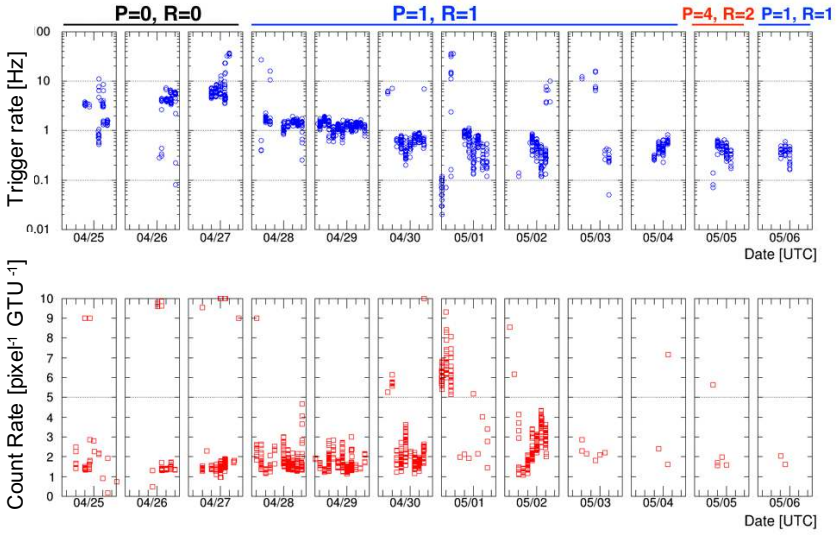

Figure 5.3: Performance of the First Level Trigger during flight. *Top:* Trigger rate as a function of the flight date. *Bottom:* Average count rate per pixel. The trigger was tested in difference configurations optimal for a Balloon flight ({P=0,R=0}, {P=1, R=1}) and for JEM-EUSO ({P=4, R=2}). Plot from [64]

associated flight information including the time of the acquisition, GPS attitude and triggered pixel cells among others. The data is temporally organized in units called packets which contain 128 continuous GTU, making one packet 320 μs long. Each packet is saved after a trigger is issued, it is assembled by placing the first triggered GTU between the GTU slot 38 to 40 of the packet, then the rest of the packet is filled with the previous and subsequent GTUs in order to fill the 128 slots. This is schematically depicted in figure 5.4.

5.3.1 Squeezed files

During flight one of the two Iridium antennas of the balloon platform failed, reducing the data transmission rate by half. This event combined with the constant altitude variations prompted the team to devise a maneuver to accelerate the data download, this resulted in the creation of squeezed files. These files are compressed data files which remove redundant GTUs in a packet, keeping only the relevant part of a packet, around the triggered GTU. This allowed to download more data files before the mission was terminated. These files are in principle the same as regular files, only a small difference is made when processing them to account for the number of active GTUs in the packet (see sec. 5.4.3.1).

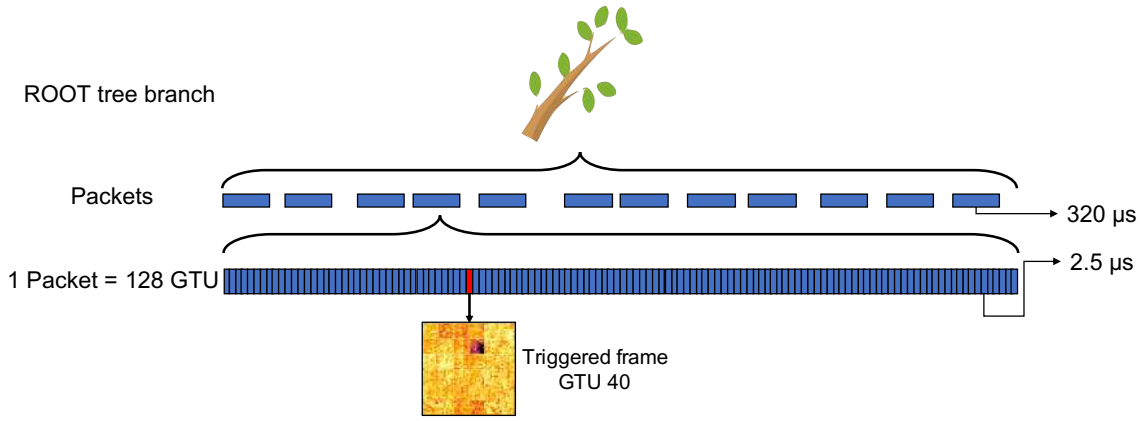

Figure 5.4: Data structure of the EUSO-SPB1 data. The ROOT branch that contains the photon count data and associated information is composed of multiple packets taken during runs of ≈120 seconds. Each packet is 320 μs long and is composed of 128 GTUs of 2.5 μs each. The packets are assembled and saved once a trigger condition is issued. The triggered GTU is placed in the slot 40 of each packet.

5.4 Analysis method of the EUSO-SPB1 data

5.4.1 Visual Inspection

The initial goal of the analysis consisted in understanding better what kind of events were triggered during flight. The first approach taken was to visually inspect the data to make a qualitative analysis of the events. Since there are thousands of GTU frames to observe, I developed a graphical user interface application to rapidly visualize and navigate through the data frames (see fig. 5.5). It allowed to step through single or multiple frames, to display frames in a "movie" mode and provided multiple visualization options to make it user friendly. As the visual analysis of the data progressed, the application was updated to include a classification option and to save the classified events into a database.

5.4.2 Event categories found

The visual inspection process showed that the events consisted in pixel excesses of different sizes and shapes. The observed events are typically 1 GTU long, however in some cases the signal persists longer. The main events found include single pixels peaks called "hot pixels", pixel groups of varying sizes called "blobs" and linear "track" features. The blobs were categorized as a function of their size with respect to the point spread function (PSF) of the instrument (3x3 pixels). Additionally, many of these events were frequently located and constrained in the edge pixels of an MAPMT, because of this they were considered as a category of their own. In total the following categories of events were identified: (a) tracks, (b) small blob (< PSF), (c) PSF blob, (d) big blob (> PSF), (e) edge effect and (f) hot pixels.

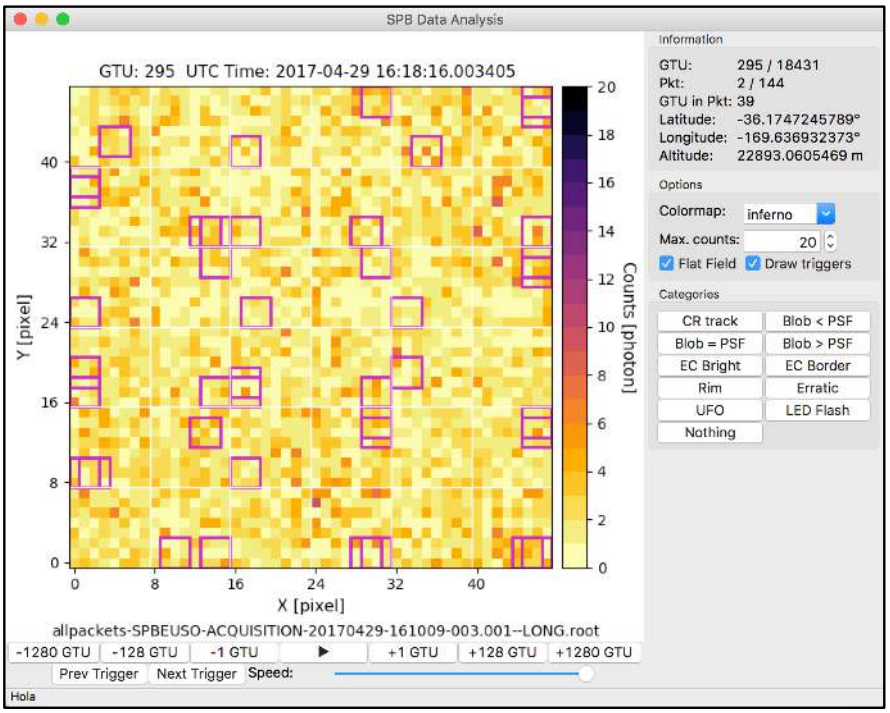

Figure 5.5: Application developed for visualization and preliminary categorization of the EUSO-SPB1 data. It allows to display the data in "movie mode" (continuous frames in succession) and quick navigation of the frames. The Purple squares in the frame indicate the triggered cells.

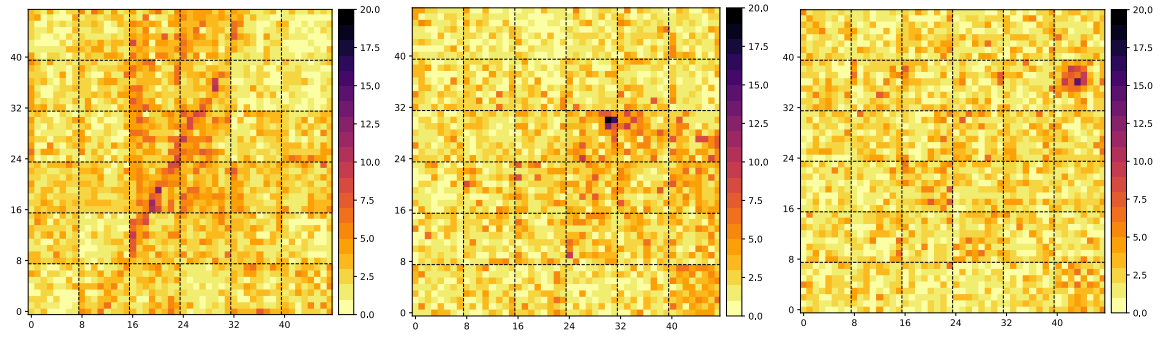

(a) Track (b) Small blob (c) PSF blob

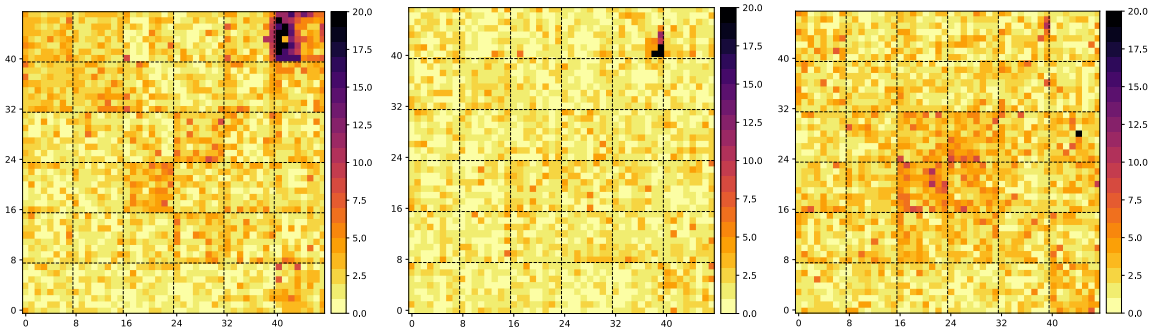

(d) Big blob (e) Edge effect (f) Hot Pixel

Figure 5.6: Categories of observed events. From top left to bottom right: track, small blob, PSF blob, big blob, edge effect, hot pixel. The colorbar indicates the number of photon counts.

An example of each category of "event zoo" is shown in figure 5.6. Other events were also identified during the visual analysis, however they were excluded because they were either artificial (LED Flashes) or were observed only a few times and depicted erratic behavior in the detector. The events are described in more detail in the next sections.

5.4.2.1 Tracks

Track events were first observed during the status checks of the instrument during flight. Initially it seemed like a unique type of event, but after inspecting more data, more track events were found. The origin of these events is attributed to direct cosmic ray hits on the detector, given their linearity and short duration of 1 GTU. This seems plausible since it is known that cosmic ray muons produce similar linear features in Charged Couple Device (CCD) detectors [102]. However, the physical nature of the interaction is not necessarily the same since the construction of a CCD and MAPMT is different. In CCDs ionization induces charge generation along path of the striking particle and produces a track that may cross multiple pixels. In the case of MAPMTs it's not entirely clear how the tracks are produced.

5.4.2.2 Blobs

The most simple type of event are the pixel blobs. Since they vary in size it was decided to split them into different size categories as a function of the PSF size on the PDM (3x3 px) to facilitate the search for possible point sources of light. Blobs were the events more commonly observed during the visual inspection phase and initially they didn't seem to be very significant. It was only after the observation of multiple tracks that it was hypothesized that some of these blobs might share a common origin with the tracks, i.e., they're the product of a cosmic ray interaction with the detector. The difference is that the cosmic ray hit occurs at an almost perpendicular angle with respect to the focal surface so that it produces a more punctual interaction. This is also discussed in section 5.5.4.1.

5.4.2.3 Hot pixels

These events are single high excess pixels and seem to be related to blobs. They have also a typical 1 GTU duration and weren't observed as often as the larger sized blobs. They were made a category of their own due to their particularity, they are the smallest type of event possible.

5.4.2.4 Edge efects

During the visual inspection it was notorious that a particular EC triggered very often, specially in the border cells. This behavior was also present in other ECs and wasn't observed before during tests on the PDM. Due to the particularity of this event type it was made a category of it's own. Just like the other events, edge effects typically last 1 GTU but this varies depending on the trigger setting. To get a preliminary idea of the prominence of this effect I created a heat map with the trigger counts per cell, the result is shown in figure 5.7. It can be seen in the plot of the 27^{th} of April that indeed, by a large margin, most of the triggered cells are in the EC7 (upper left) and particularly in the border cells. This day featured a particularly high trigger rate (see fig. 5.3) and it is now known that this happened due to electronic disturbances caused by the SiECA instrument located next to PDM. After this problem was dealt with and the trigger setting changed, the difference is remarkable as shown in the sub-plot of the 29^{th} of April This day features a more evenly distributed trigger count on the detector but the edges of the MAPMTs are still dominant. The causes for this effect are discussed in sec. 5.5.4.2.

5.4.2.5 Other Events

Another type of event which happens on certain occasions, is a bright flash that completely illuminates one or multiple ECs, this event creates a very defined border at the EC level or

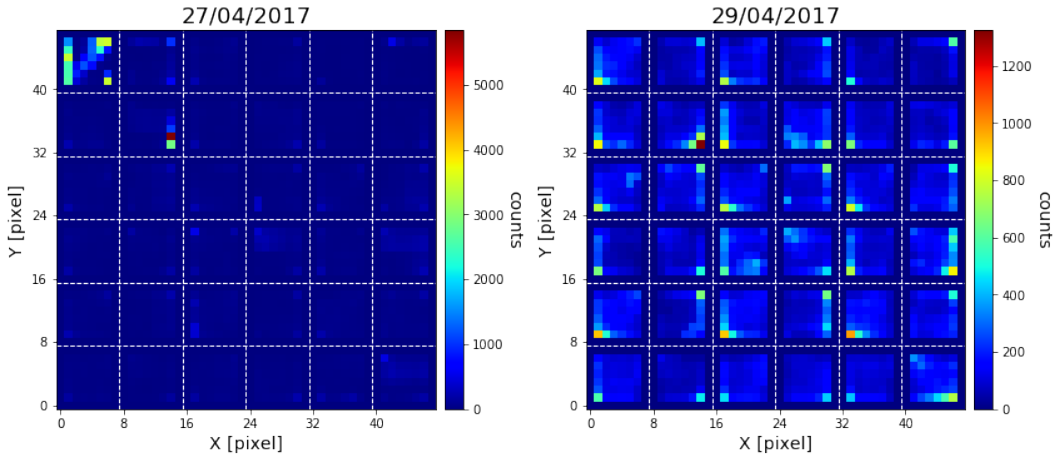

Figure 5.7: Map of the triggered cell counts on the MAPMT during two days of the flight. *Left:* Trigger map of the 27$^{\text{th}}$ of April Most of the triggers are concentrated in the borders of the upper left EC. *Right:* Trigger map of the 30$^{\text{th}}$ of April The trigger distribution is more evenly distributed along the detector but there are still hot-spots in the MAPMT edges.

even illuminates the whole detector. These "EC flashes" are not counted as a category of their own since they normally happen together with blobs and tracks but they are mentioned since there seems to be a relationship with the intensity of the primary event and the number of illuminated ECs Figure 5.8 shows two examples of an EC flash accompanying a big blob and small blob event, it can be seen that in the first case that most of the detector illuminates whereas in the second case, only the lower row ECs are illuminated and the rest of the ECs maintain a normal background level.

5.4.3 GTU data processing

About 1 million frames were visually inspected in order to build a basic understanding on the contents of the data. The next step consisted in the development of an automated method to process each data frame, extract the observed features from each frame and build a database that could be used for further analysis. Since the trigger, by definition, picks up localized excesses above the background level, the chosen approach was to use a technique that separates the pixels of interest from the background and obtaining quantitative features of the extracted feature. Many of the algorithms used for the analysis are available in the scikit-image package for python, which contains a library of image processing routines. The method consists of the following steps: background subtraction, smoothing the image, thresholding, pixel grouping and labeling, ellipse fitting, information extraction, classification and indexing into a database. The process is schematically explained in figure 5.9 and the steps are described in more detail in the following sections.

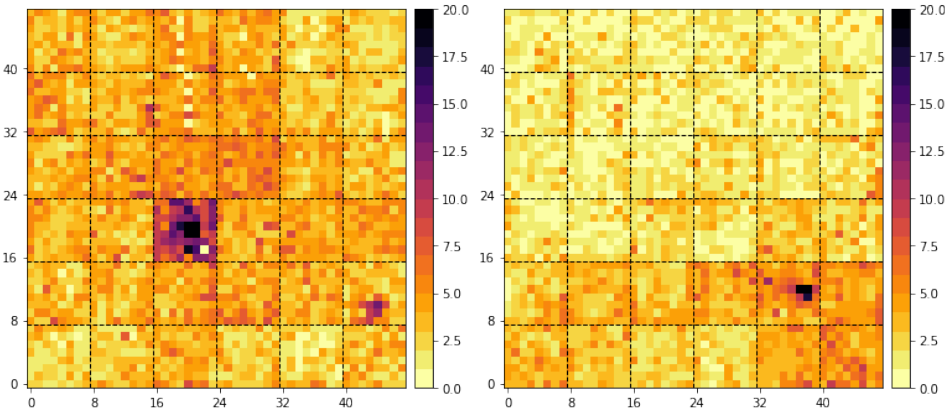

Figure 5.8: EC flash which accompanies a triggered event. *Left:* A big blob event in which the whole detector is illuminated. *Right:* A small blob event where only the EC where the event takes place and other MAPMTs are illuminated, denoting a sharp border between ECs. . The colorbar indicates the number of photon counts.

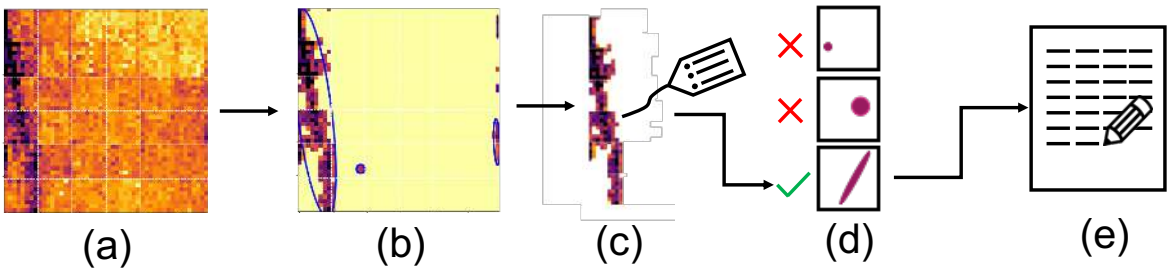

Figure 5.9: GTU frame processing method: (a) The raw GTU frame is processed by removing background noise and smoothing the image. (b) Background pixels are removed, neighboring pixels are grouped into regions and the region is fitted with an ellipse. (c) The properties of the region are extracted. (d) The region is classified and (e) saved into a data set for further analysis.

5.4.3.1 Background subtraction

The average background per pixel per packet is computed and subtracted from the frame that is being processed. Since the squeezed and non-squeezed files have a different structure (see sec. 5.3.1) each type of file is processed in a different manner. The background in non-squeezed files is estimated by calculating the mean of each pixel from GTU 1 to 35, this GTU range is behind the trigger position (GTU 38-40) and avoids any signal excesses above the FLT thresholds. In squeezed files the pixels from GTU 32 to 56 are averaged since this is all the information available per packet.

5.4.3.2 Low pass filtering and Thresholding

Some frames, specially triggered ones, tend to be noisy and make harder the process of separating the events of interest from the rest of the pixels in the grid. To ameliorate this the image is smoothed by using a low pass filter. This averages out rapid variations in pixel intensity, flattening noisy background zones while preserving pixel excesses.

To extract the events of interest it is necessary to separate the pixel from the background. To do this several fixed and dynamic thresholding methods were tested and Otsu's method [103] was selected. This method works by creating two classes of pixels (foreground and background) by setting an initial threshold from the value distribution of all the pixels. Then, different threshold values are iterated in order to minimize the within-class variance (σ_w^2) of the two classes. This is defined as the sum of the weighted variances of each class:

$$\sigma_W^2(t) = w_b(t)\sigma_b^2(t) + w_f(t)\sigma_f^2(t) \tag{5.1}$$

Where w_b and w_f are the probabilities (weights) of the two classes separated by threshold t, σ_b^2 and σ_f^2 are the variances of each class. In practice, a computationally faster approach is to maximize the between-class variance of the two groups. It is obtained by subtracting the within-class variance from the variance of the total distribution. This computation is simplified as follows:

$$\begin{aligned}
\sigma_B^2 &= \sigma^2 - \sigma_W^2 && (5.2)\\
&= w_b(\sigma_b - \mu)^2 + w_f(\mu_f - \mu)^2 && (5.3)\\
&= w_b(t)w_f(t)\ (\mu_b(t) - \mu_f(t))^2 && (5.4)
\end{aligned}$$

where the distribution mean $\mu = w_b\mu b + w_f\mu f$. μb and μf are the mean of each thresholded distribution. Applying the algorithm to a data frame yields a threshold value which is used to create a binary mask from the image, i.e., the pixels above and below the threshold get a

one and zero value respectively.

5.4.3.3 Pixel grouping and labeling

The next step is to run a connected component labeling algorithm on the binary mask. This algorithm groups adjacent pixels that have the same value (one) and assigns a unique numeric value to label each newly created "region" of connected pixels, the background pixels are ignored and are by default zero. To group the pixels together a connectivity setting of 2 is used, connectivity refers to the number of orthogonal hops required to arrive from one pixel to another. Therefore, for a connectivity of 1, only the pixels above, below and to the sides of another pixel are considered as connected, whereas for a connectivity of 2 also the corner pixels are considered. The algorithm is schematically explained in fig. 5.11. Ideally, after processing the image and labeling the pixels, only one pixel region should remain which makes it fairly simple to classify and index it in the database. In reality, this is not always the case since many frames produce more than one pixel region (see fig. 5.10), specially noisy frames where a few noisy pixels tend to remain after processing the frame. This is a problem since it would result in indexing a noisy pixel or group of pixels as false positives, to resolve this only the region with the most significant pixel is kept, so there is one event per GTU.

Another issue is that not all the GTUs in the packets contain events, i.e. pixel excesses, yet they are all processed to search for one. This means that when background frames are processed they produce an output of pixel regions which are a local maxima but don't have much significance. Indexing these events in the database would result in adding a lot of false positives. Fortunately, background frames as well as LED flashes have a more uniform value distribution across the pixel array compared to a real event, this results in a lower variance and therefore also a lower Otsu's threshold value. Due to the lower threshold value, multiple pixel regions are created after processing and labeling a background frame, typically 20 regions or more (see the bottom row of fig. 5.10). So, to avoid indexing insignificant regions of background frames in the database, a threshold is set in the number of maximum regions allowed. If the number of produced regions is above the threshold, then no regions from this GTU frame is added to the database. This solves the issue and automatically rejects background frames from the analysis, except for the ones with higher variance. However, if the threshold is too low it might omit real events in noisier frames and if it's too high it will include insignificant pixel regions with above average values from background frames. For this analysis a threshold of 10 pixel regions per GTU was found to be acceptable and was used for the analysis runs. Figure 5.10 shows an example of an event frame and a background frame to help make this point clear.

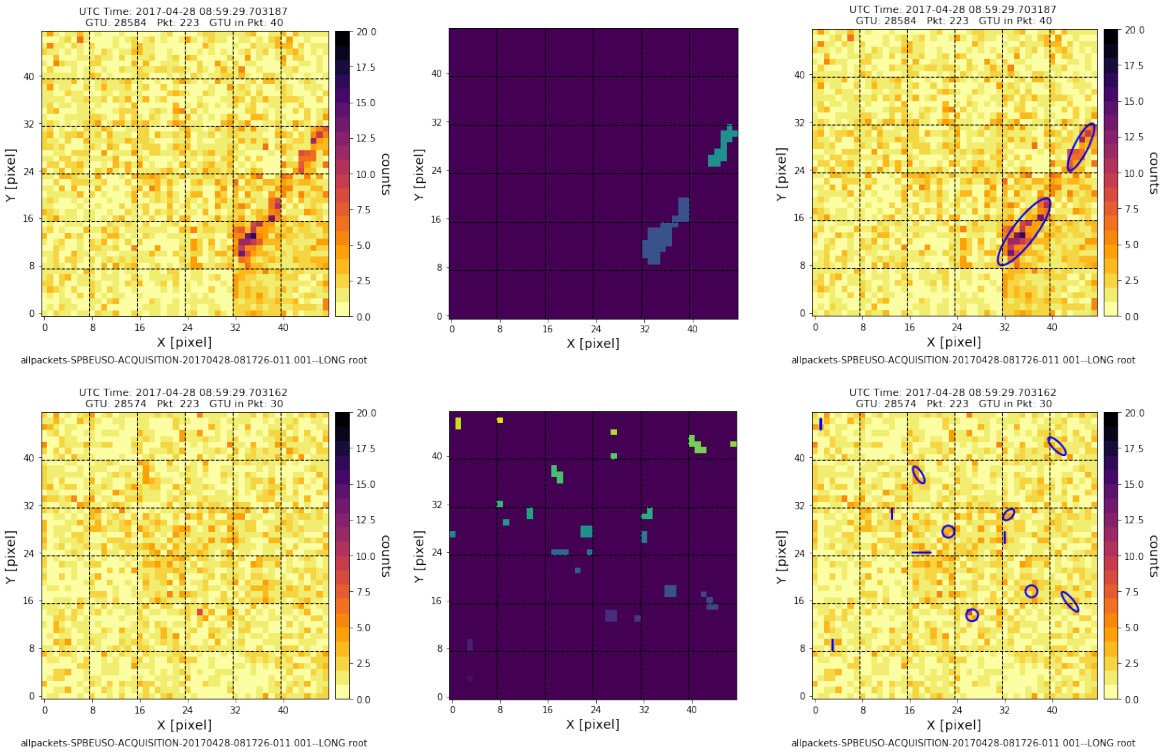

Figure 5.10: Processing result of an event and a background frame. *Top row:* GTU Processing of a frame with a track event. The left panel shows the raw frame with the event, the middle panel shows the two isolated pixel regions and the right panel shows the frame with the ellipse-fitted pixel regions. *Bottom row:* Processing of a background frame, the left panel is a regular background frame, the middle panel shows the small pixel regions created after the frame is processed and the right panel shows the ellipse-fitted regions (1 px regions are not fitted). Background frames topically produce many small pixel regions and are discarded from the analysis by setting a threshold on the maximum number of regions allowed.

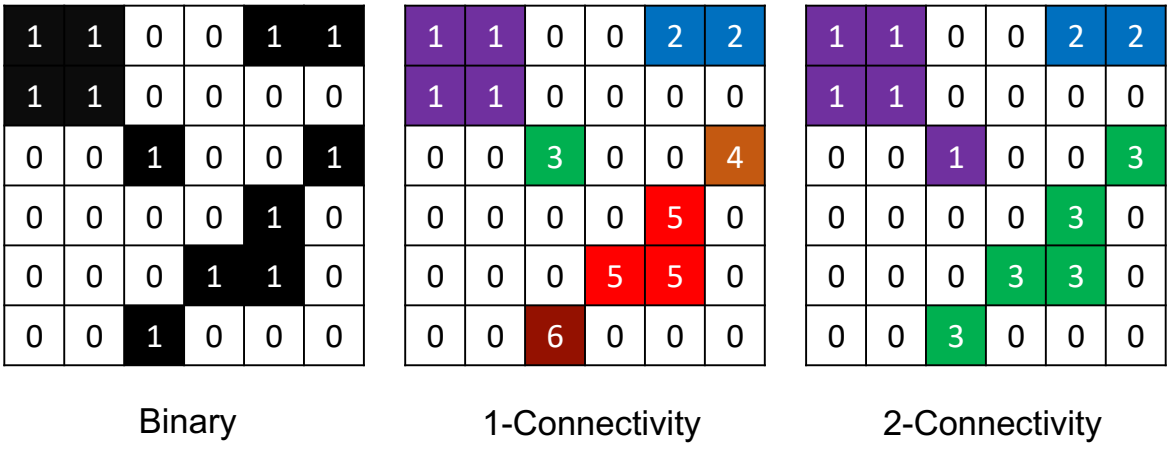

Figure 5.11: Pixel connectivity of the connected component labeling algorithm. *Left:*Binary image used as input for the algorithm. *Center:* Output of the algorithm using a 1-connectivity setting, the pixels positioned diagonally are not considered connected and are labeled separately, this results in a total of six pixel regions. *Right:* Output using a 2-connectivity setting, the diagonal pixels are considered connected and the result is three pixel regions.

5.4.3.4 Ellipse fitting

Once a pixel region has been isolated the corresponding pixels in the unprocessed image are analyzed and their parameters extracted. Another important piece of information is created by fitting the pixel region with an ellipse and saving the ellipse parameters. The eccentricity of the fitted ellipse allows to know how circular or elongated is the region and the major axis gives the pixel-wise length, these parameters are useful to discriminate between the circular blobs and the more elongated tracks in order to classify each category.

5.4.3.5 Classification of the events

The classification is done using simple conditions based on the morphology of the pixel region. Tracks are classified based on the eccentricity and major axis of the ellipse that encircles the region. Blobs on the number of pixel rows and columns with respect to the Point spread function of the instrument $\approx$ 3×3 pixel. Edge effects on the number of pixels located on the edge of the MAPMT with respect to the pixels not on the borders. The classification process also has a hierarchy because some events may have a similar morphology. Therefore, if an event is elongated enough it will be classified as a track and if it has more pixels on the MAPMT border it is classified as an edge effect even if they resemble blobs. The classification conditions and hierarchy are listed in table 5.1, figure shows an example of each type of event

Table 5.1: Table of parameters use to classify the pixel regions into different categories. n_{rows} and n_{cols} is the number of pixel rows and columns respectively, n_{px} is the total number of pixels in the region, $n_{px\ border}$ is the number of pixels on the MAPMT borders, the eccentricity and major axis correspond to the ellipse that fits the pixel region. Any region which is not bounded by this conditions is classified as unknown. The order of the elements also specify the hierarchy of classification in case some events have similar features.)

Category	n_{rows}	n_{cols}	n_{px}	**Eccentricity**	**Major Axis**
Track	—	—	—	>0.9	>5
Edge effect	—	—	$n_{px\ border} \geq n_{px}/2$	—	
Hot Pixel	1	1	1	—	—
Small blob	≤ 3	≤ 3	< 9	—	—
PSF blob	$3 \vee 4$	$3 \vee 4$	$9 \leq n_{px} \leq 16$	—	—
Big blob	>4	>4	$16 > n_{px} > 50$	—	—
Unknown			All Else		

5.4.3.6 Event indexing

After the event is extracted and classified, it is indexed into an event "zoo" database that is used for further exploratory analysis. Each entry in the database is a vector that contains information about the event, some of the parameters included are: the file and GTU of the event, time of the acquisition, GPS coordinates, statistical information about all pixels in the GTU, the shape of the event, fitted ellipse parameters, the pixel maximum, mean and sum of the event among others. This information can be sorted and filtered in order to look for properties of the dataset, look for consecutive events in the search for EAS and understand the population of the classified events. The next section shows the results obtained from this analysis.

5.5 Analysis results of the event database

5.5.1 Event detection

After pre-processing, the flight data was reduced to about 89k events of interest for further analysis and visual inspection. Figure 5.12 shows the distribution of detections per category per GTU. It can be seen that there is a detection peak for all categories that matches very well the trigger position in the packets (GTU 38 to 40). Following the peak there is a tail which decays at a rate which varies depending on the type of event, the most notable is the edge effect which has the most persistent detection rate after the trigger, indicating a signal persistence which favors the MAPMT edges. The sharp increase and cutoff at GTUs 32 and 57 is due to number of squeezed files analyzed which contain no information outside of this GTU range. The number of event detections outside of the GTU band between the trigger peak and it's tail (GTU 38 to 57) is about 50 per GTU except for the GTU 32 to 37 where

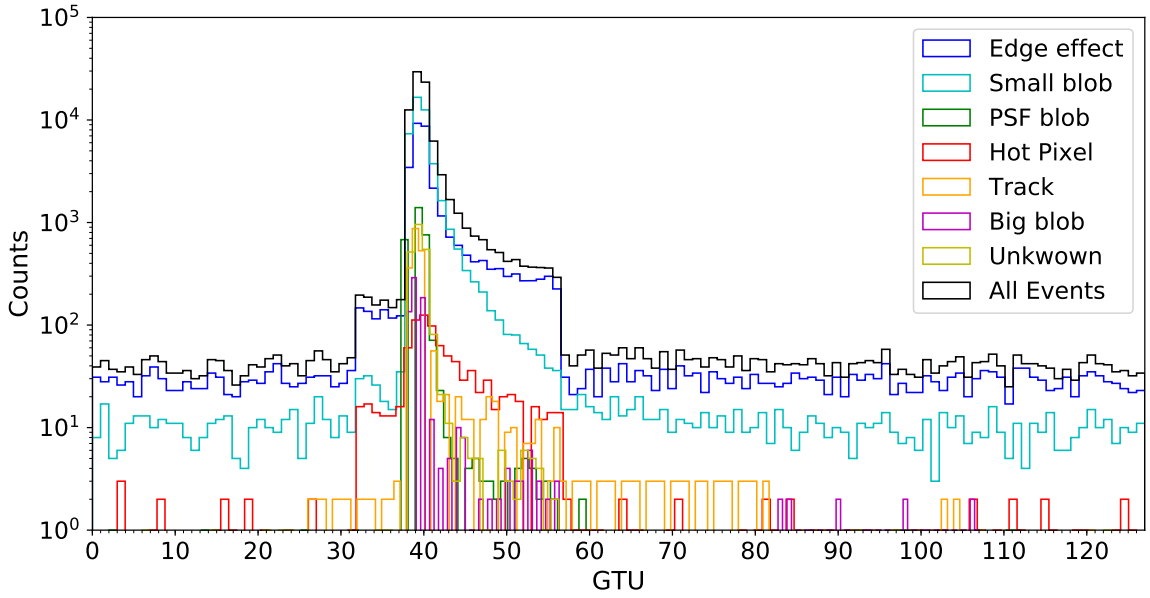

Figure 5.12: Number of detected events per category per GTU. The maximum number of detections matches well the trigger position within the packet (GTU 38 to 40) and after the peak there is a decaying tail with a significant amount of detections. The sudden step increase in GTU 32 and decrease in GTU 57 is due to the squeezed files.

it rises to ≈200. In total there are about 6000 detections outside of the trigger zone which is about 7% of all events, so the majority of detections are made between the start of the trigger and 20 GTUs after. Overall we can say that the method for extracting events is in good agreement with the trigger.

5.5.2 Search for Extensive Air Showers

EAS candidates were searched by joining consecutive events from the database with a duration ≥3 GTU. This produced 4128 multi-GTU events ranging from 3 to 40 GTU long (16236 GTU in total). For an EAS the signature we're looking for is a blob propagating across the detector during consecutive GTUs. All the multi-GTU events were visually inspected but no EAS signature was found. However, the observed events follow a recurring pattern: they are a static signal which typically starts as a big blob and then decays into an edge effect or small blob. They're localized in a single MAPMT and there is no movement across the detector. This is shown in figure 5.13 that features one event with an 8 GTU duration. Although an EAS signal not moving across detector is not impossible, it has to be aligned with the FoV line of a given EC, an extremely unlikely event. To be sure it's sufficient to look at the time profile of the packet containing the event. Figure 5.14 shows counts per GTU of the packet containing the same 8 GTU event plotted at the PDM and EC level. In both plots the signal starts with a stable background level, then there is a high peak at the triggered GTU which decays after 1 GTU. In the EC level plot we can appreciate that the EC containing the event

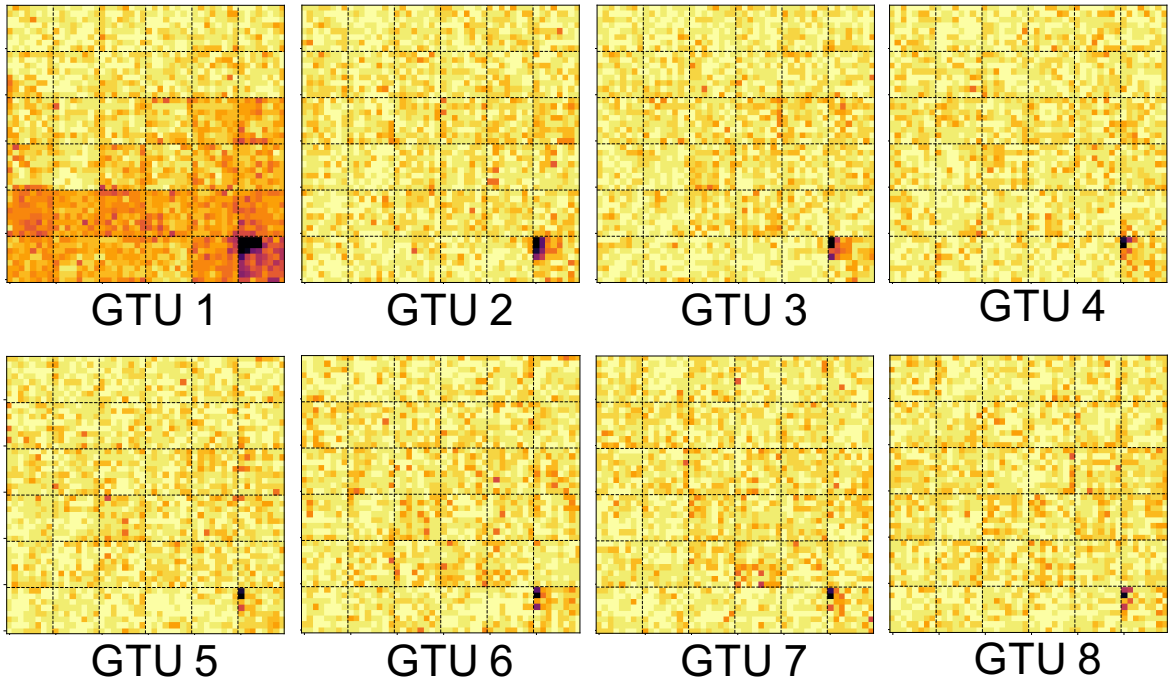

Figure 5.13: 8 GTU event found in the data. The first frame shows an event which starts as a big blob and decays into an edge effect

maintains a signal persistence which then decays after 7 GTU. Given that no EAS candidates were found in the analysis we therefore assume events extracted from the data are background (BG) events which impede our capability to observe EAS.

5.5.3 Population statistics of background events

The BG event population statistics are shown in figure 5.15. The chart shows that most of the detected events are small blobs with 51.8% of the total, edge effects follow closely with 38.1% and the rest of the events account for less than 4% each. An important aspect to notice is the number of pixels per event. Figure 5.16 shows the distribution of total pixels per event and it's cumulative distribution. The most common pixel quantity per event is five with about 20% of the total and about 80% of BG events have less than nine pixels, the expected PSF size. The small size and short duration of the majority of detections point at non-EAS related origin. First, because a point source of light would produce signal with a three pixel width and a length that depends on the fraction of FoV traversed in one GTU, but no less than three pixels (see fig. 4.1). Second, because the time profile of the BG events is characterized by a peak that decays after one or a few GTU, as shown in fig. 5.14. The signal of an EAS would show the growth, maximum and decay over a few GTU. Therefore understanding the underlying causes of the observed population of BG events is crucial for the improvement of future triggers.

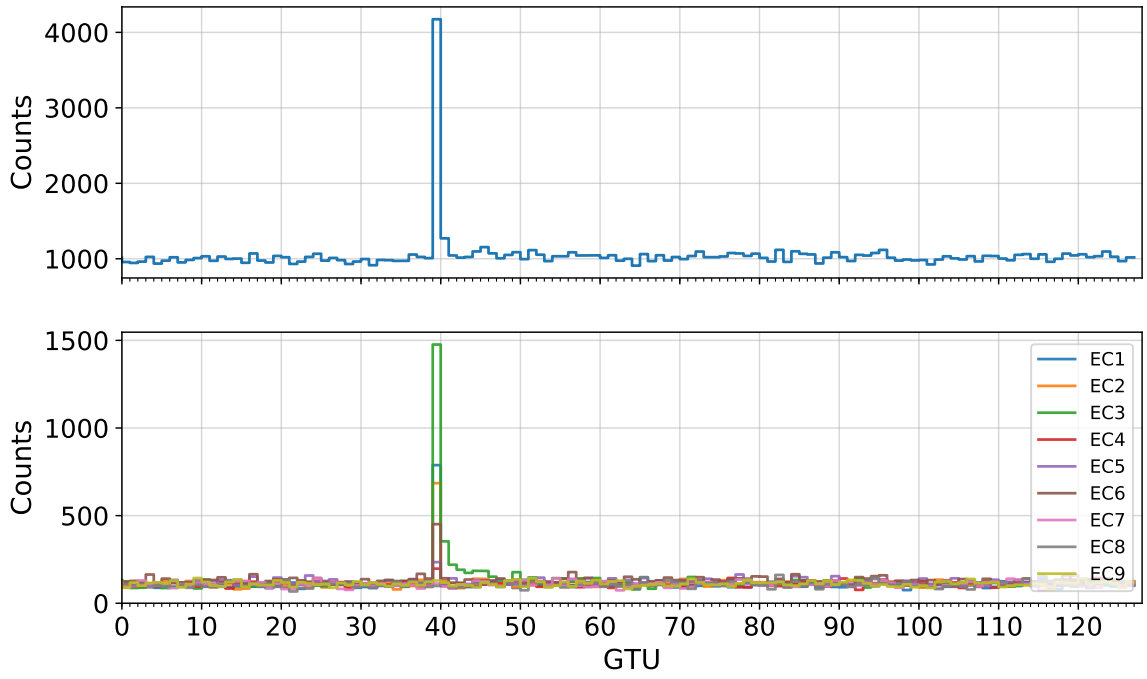

Figure 5.14: Photon count as a function of GTU of the 8 GTU event shown in figure 5.13. *Top:* Photon count at the PDM level, there is a single peak at GTU 40 which decays immediately. *Bottom:* Photon count at the EC level, it can be seen that there is the peak at GTU 40 for multiple ECs with EC3 being the highest one, the signal decays in all but EC3 which has a signal tail that lasts a few GTU.

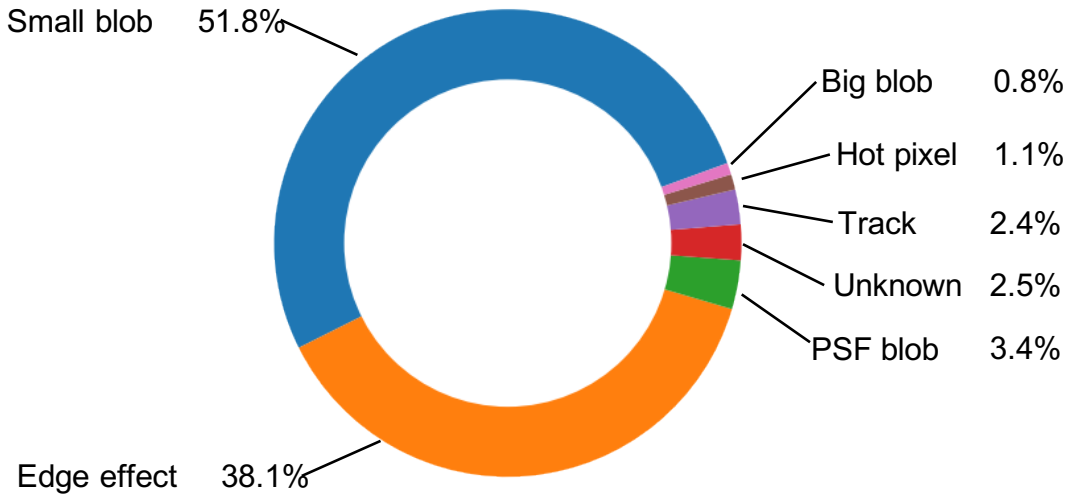

Figure 5.15: Population of event categories obtained from the analysis of EUSO-SPB1 data. The most common type of event is the small blob with 51.8% of all detected events

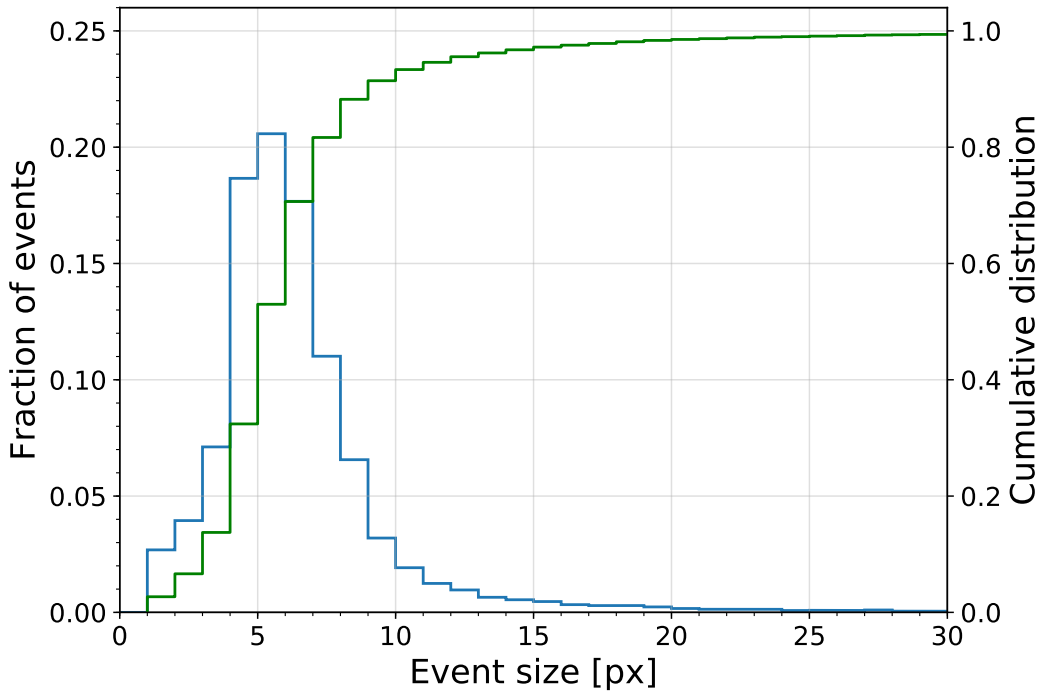

Figure 5.16: Pixel size distribution of events.

5.5.4 Discussion on the origin of events

5.5.4.1 Tracks, blobs and hot pixels

Tracks, blobs and hot pixels can be explained by direct cosmic ray hits in the detector, given the environment of the balloon-craft and the linear pattern of tracks. This is supported by observations reported on the data analysis results of the TUS observatory [76, 104]. Similar track events have been observed in TUS data and reconstructed using simulations performed with the GEANT4 simulation toolkit. The results reveal that protons with energies from 100 MeV to 10 GeV produce Cherenkov and Fluorescence photons when they hit the UV filters at a parallel or almost parallel angles with respect to detector plane (see figure 5.17a for a schematic depiction). In the case of TUS this interaction can induce a trigger on a PMT beginning with a proton energy $\geq$ 100 MeV. Higher energies trigger more PMTs along the proton's direction of propagation, up to 16 PMTs for a proton of 400 MeV.

If we extrapolate the track scenario to CR hits on the detector plane at oblique incidence angles. Then a more punctual interaction is produced, most likely from Cherenkov photons which are anisotropic compared to the isotropic fluorescence photons. However, given the nadir observation mode of EUSO-SPB1, the majority of CRs should arrive from the back part of the PMT, traverse it's body and interact in the glass screen and UV filter. This means that for a signal to be produced, the Cherenkov light produced in the interaction

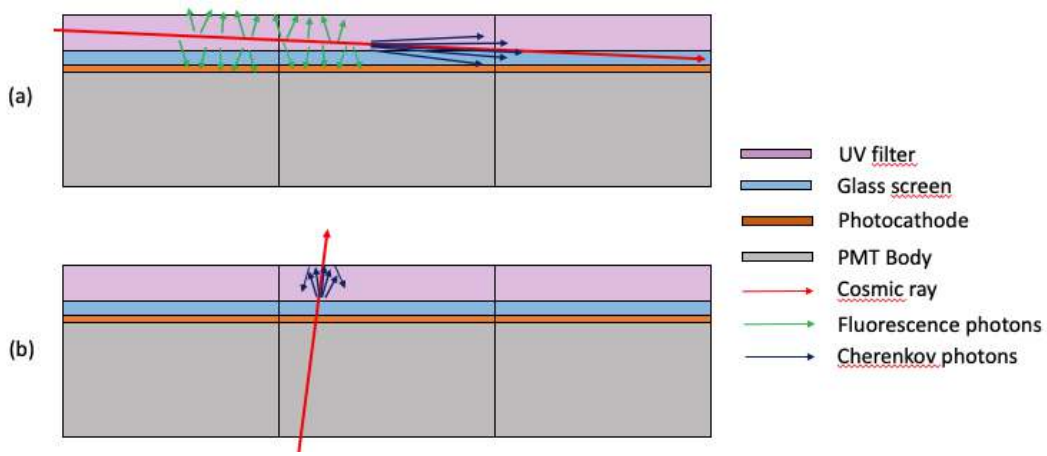

Figure 5.17: Cosmic ray hits on a PMT detector array

should be reflected back to the photocathode (see figure 5.17b). The previous hypothesis cannot be confirmed by TUS since blob events were not observed in the data. The reason is simple, one TUS pixel size is in the order of one EUSO-SPB1 EC. Therefore, the single pixel excesses or multi-pixel blobs in the EUSO-SPB1 PDM would be seen as a single pixel excess in the TUS detector.

An attempt was made to reproduce the blobs using the geometry of one MAPMT on the GEANT4 software but it remained inconclusive. Figure 5.18 shows one example simulation done by shooting a 1 GeV proton from the back of the PMT. In the short interaction about 120 Cherenkov photons are produced, the Cherenkov cone can be clearly observed but the majority of photons propagate out of the optical window. Only a few photons are back reflected towards the photocathode however their quantity is not comparable to the blobs. In reality the number of photons is further reduced if we consider the quantum efficiency of the photocathode (about 35%) and the double pulse resolution of the PDM (10 ns). Due to lack of expertise in the software it is unclear if the simulations were representative, i.e. included all the relevant physical processes necessary to approximate reality. Nevertheless, they show that indeed the atmospheric cosmic rays do produce secondary photons that can produce signals in the detector.

5.5.4.2 Edge effects

The repetitive and localized behavior of edge effects point to an instrumental effect as their most likely explanation. This is corroborated by calibration tests performed at the APC laboratory on new batches of MAPMTs intended for use in follow-up experiments of the collaboration (K-EUSO and Mini-EUSO). In these tests, each of the MAPMT pixels is tested two-fold: first by applying an uniform illumination on all pixels and then by individually illuminating each pixel.

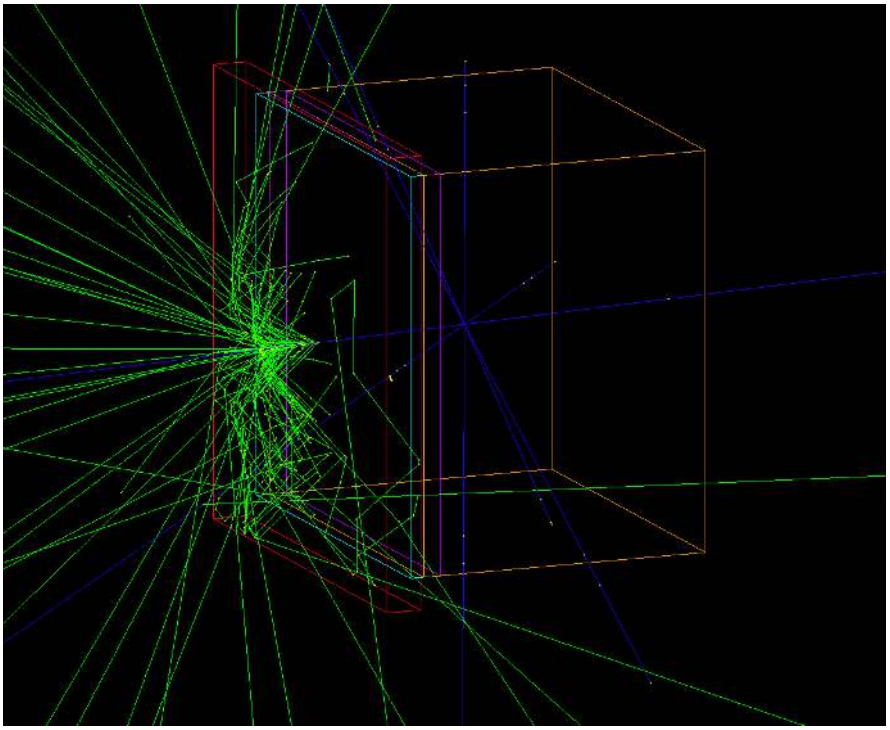

Figure 5.18: Geant4 simulation to test cosmic ray hits on the PDM of EUSO-SPB1. The cosmic ray is injected from the back of the PDM since this represents the trajectory of most cosmic rays hitting the nadir pointing detector.

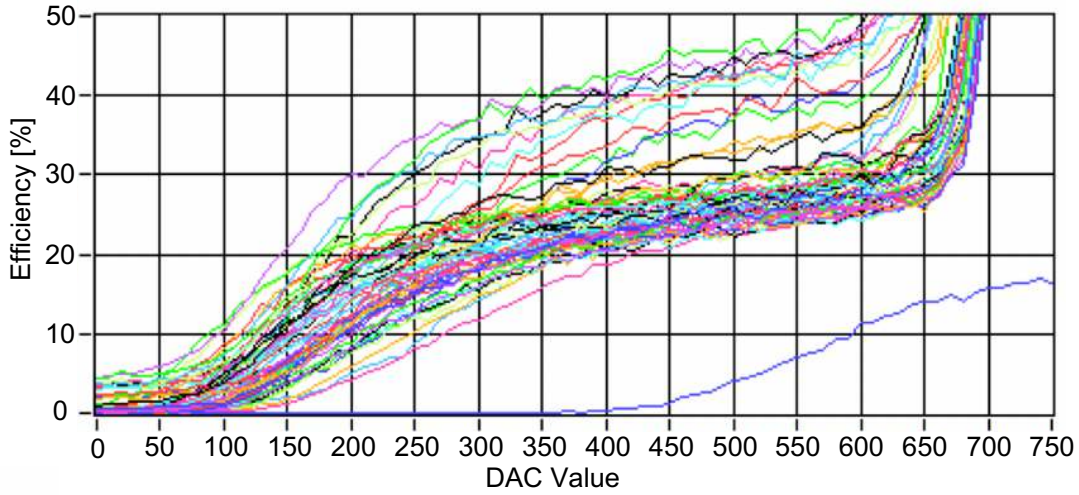

Figure 5.19: Efficiency of MAPMT pixels as a function of DAC value tested with uniform illumination across all pixels. It can be observed that a fraction of the pixels show a larger efficiency compared to the rest. Also there is one defective pixel.

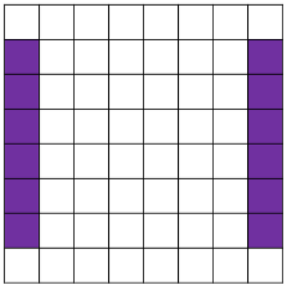

Figure 5.20: Location of the crazy pixels located in the MAPMTs

The results of a uniform illumination test are shown on figure 5.19. In the plot we can observe the efficiency (i.e. the ratio of photons received to photo-electrons recorded) of each of the 64 MAPMT pixels as a function of DAC value. If we look at a value of 500 DAC some of the pixels indicate a higher efficiency, from about 30 to 50% while the rest pixels have less than 30% efficiency. These high efficiency "crazy pixels"[3] are located on the edges of the MAPMTs as shown in figure 5.20. However, the number and location of the crazy pixels could vary on different MAPMTs. On the other hand when the MAPMTs pixels are illuminated individually the high efficiency of the crazy pixels is gone and all the pixels show a more uniform efficiency profile. This difference in efficiency depending on the type of test executed means that there is some crosstalk which becomes evident when all pixels are illuminated.

The results of the previous experiment were reported to the manufacturer of the MAPMTs (Hamamatsu) who was interested on figuring out the causes and implementing a solution. The company is secretive about their processes, so the information available is very limited, however what is known is the following: The possible cause for the effect seems to be due the generation of light produced by the excitation of residual heavy ions in the MAPMT, this process is known as ion feedback. This happens because some of the secondary electrons leak from the anode to the bottom of the PMT (both are biased to the same voltage), hit it and excite heavy ions. The ions then relax and produce light which can then travel through two slits present on two sides of the MAPMT and hit the photocathode. If these photons are converted to photoelectrons then a second photo-multiplication ensues giving the appearance of a higher gain. The process is depicted in figure 5.21, but the diagram is speculative since the internals of the MAPMT are not known.

The aforementioned electron leak on the MAPMTs can explain the presence of edge effects, specially if the ion feedback is repeated multiple times during one GTU. A single night-time UV photon or group of photons produced by a CR could be enough to start the ion feedback loop that gives rise to edge effects. Moreover, the signal persistence seen in some events and the tendency to decay towards the edges (as in figs. 5.14 and 5.13) can also be explained from the electron leak which concentrates the ion feedback loop on the edges. This proves that edge effects were indeed provoked by instrumental features beyond the control of the

[3]The nickname given by our colleagues to these "high efficiency" pixels to differentiate them from the rest.

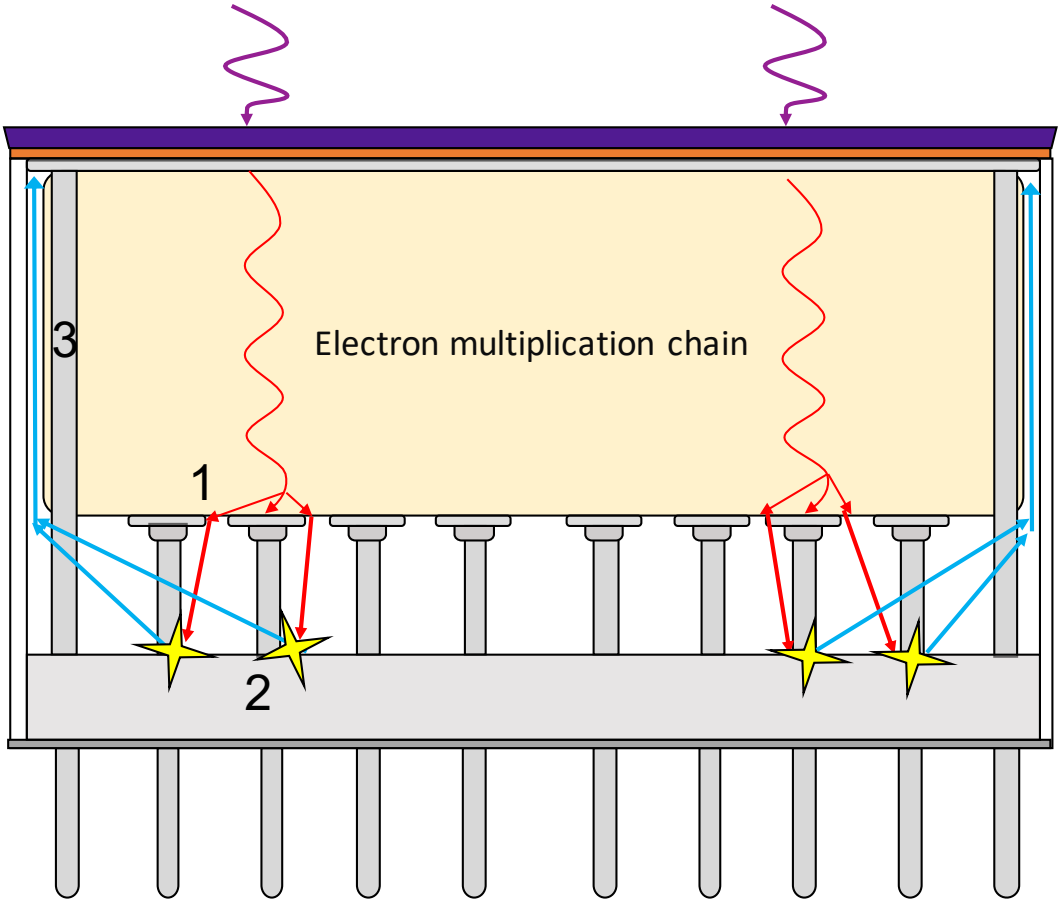

Figure 5.21: Possible cause for edge effects due to light generation by ionized residual ions. (1) Secondary electron multiplication. (2) At the anode some of the electrons leak to the bottom of the MAPMT, biased at the same voltage. The electrons excite heavy ions which then relax and produce light. (3) The light propagates through one of two gaps present only at the sides of the MAPMT and hit the photocathode. If the photons are converted to photo-electrons then a feedback loop ensues.

collaboration. Fortunately, the manufacturer implemented "countermeasures" to reduce the electron leakage. The correction details are not known but new MAPMTs were developed by the manufacturer and tested by our collaborators. These tests indicate that the problem seems to have been solved. It only remains to verify is edge effects are indeed mitigated during an experimental run for a new pathfinder.

5.5.5 Zoo classification method on simulated EAS events

Although the EUSO-SPB1 event zoo classification was developed based on the observation of flight data, it is interesting to know how the method reacts to simulated EAS events and if they can be detected and classified. The simulation of data for the EUSO telescopes is done with two software frameworks: ESAF (EUSO Simulation and Analysis Framework) [105] and

Offline [106]. For this test I used a dataset of simulations produced using ESAF. The data consists of packets of 128 GTU where the EAS event is injected after the 30^{th} GTU of the packet. I selected six events using as parameters two primary energies (5×10^{18} and 1×10^{19} eV) and three zenith angles (12, 52 and 81°) to understand the influence of the shower primary energy and inclination on the classification process.

Figure 5.23 shows the classification results of the six simulated showers as a function of GTU. In the low azimuth angle scenarios the classification oscillates mostly between small blobs and edge effects, whereas the higher azimuth angle scenarios tracks and edge effects are more common. The oscillation between categories occurs because as the shower develops, it traverses the FoV of border pixels and could be classified as an edge effect if the conditions are fulfilled. Also, the number of classified GTUs is on average higher in low azimuth simulations than high azimuth ones. This is logical, since the more vertical showers will traverse a smaller section of the FoV in 1 GTU, covering a few pixels per GTU. Whereas, the more vertical showers will traverse the FoV in less GTUs, covering more pixels per GTU. This can be observed in figure 5.22, it shows one GTU of the 1×10^{19} eV shower for each of the tested azimuth angles. We can observe that the pixel excesses elongate as the azimuth angle is increased. It should also be noted that the classification method is capable of rejecting pure background frames.

One might wonder, why the simulated events, specially at low zenith angles are classified as small blobs if the classification method assumes that point sources of light produce signals of about 3×3 pixels. This is because the simulations have a parametric implementation of the optics with a more optimistic performance. However, as we have discussed in chapter 3 the optics behavior deviates from the original expectation and also the zoo classification method is based on the observation of real data. Hence, differences between simulated and real data are expected. One area of improvement of the method was identified upon observing that one event was classified as "unknown" in one GTU of the shower with $E = 1 \times 10^{19}$ and $\theta = 52°$ (see the yellow dashed line of figure 5.23). This event is elongated enough to be considered a track but the ellipse that fits its pixels is just below the eccentricity threshold and thus as "unknown". Therefore the classification logic can be improved to include this event.

Overall, the event zoo classification method is capable of detecting the signals produced by simulated EAS as well as rejecting frames containing only background luminosity. The pixel excesses are classified as blobs or tracks, depending on the zenith angle of the shower with respect to the instrument and as edge effects if the signal excess is located in the MAPMT border pixels. The method however, is not capable of recognizing the detected events as EAS since it was developed to study and understand the background events. A visual inspection of the spatial and temporal structure of the events is necessary to determine if they are EAS candidates.

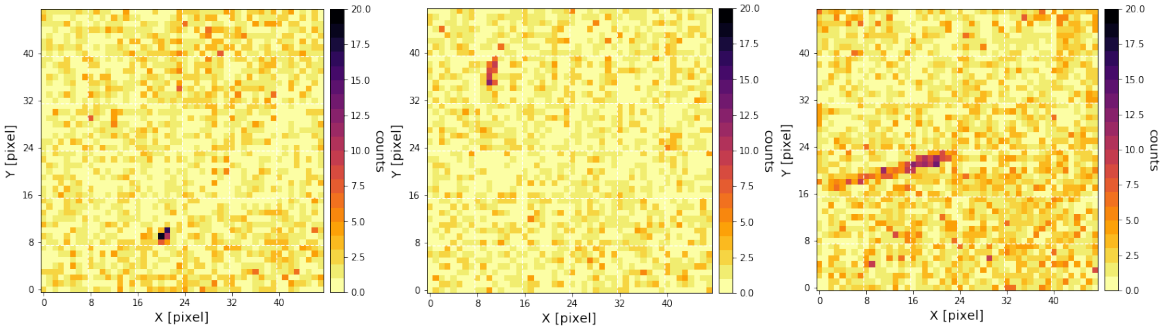

Figure 5.22: Simulated 10^{19} eV EAS events using the ESAF software at different zenith angles (θ). *Left:* $\theta = 12°$. *Center:* $\theta = 52°$. *Right:* $\theta = 81°$. The events are respectively classified as: small blob, track and track.

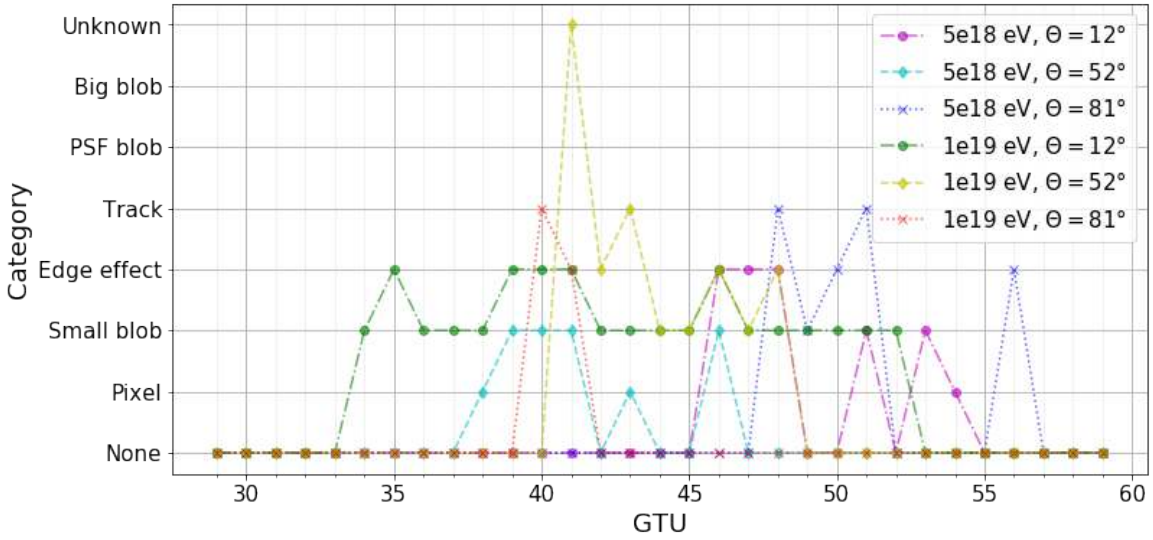

Figure 5.23: Classification of simulated EAS events as a function of GTU in a simulated EAS event using two primary energies (5×10^{18}eV and 10^{19}eV) and three zenith angles (12°, 52°and 81°)

Chapter 6

Conclusion (English)

6.1 The optics performance of the balloon pathfinders

Prior to the start of this work, the performance of the EUSO-Balloon optics was characterized during two experimental campaigns in 2014 and 2015. The characterization of the optics was essential for achieving the primary objectives of the mission and increasing the TRL of the instrument towards a UHECR space observatory. Although the mission was successful, there were several issues remaining regarding the characterization of the optics. First, starting from a design consisting of two refractive lenses and one diffractive lens, the latter had to be dropped to obtain a higher PSF efficiency. More importantly, the measured performance of the optics was in disagreement with numerical simulations and its behavior was not well understood. After the mission, the optics performance remained misunderstood and it became a key point of my work to investigate and explain the causes of this issue.

After EUSO-Balloon our team had the opportunity to work on the characterization campaign of the EUSO-SPB1 optics and to optimize the PSF efficiency for the flight. We tested a two and a three lens configuration. The measurements taken with the three lens configuration show that the diffractive lens partially corrects the chromatic aberration of the lenses. It produces a primary focus where all wavelengths converge but there is also a secondary focus with chromatic dispersion. The latter is produced because the diffractive lens does not completely modulate the 0^{th} diffraction order. Once again a two lens configuration was chosen for the flight because it produced a higher PSF efficiency and better trigger efficiency. The characterization results were also in disagreement with the numerical simulations and due to time constraints, the instrument was flown without properly understanding the optics.

To understand the measured optics performance, further analysis and testing was done on the Fresnel lenses of EUSO-Balloon. We tested each lens separately and we have shown that the they diffuse light due to residual fabrication features on the fabrication of the lenses. These features deviate from the desired surface profile on a nanometric scale and have a two periodic components of about 10 µm and 300 µm. In essence they act as a diffraction grating. Thus, we have unintended diffractive effects on our refractive lenses.

To explain the behavior of our Fresnel optics we have developed a model which combines a simple ray tracing code for refraction and reflection with a semi-empirical term for diffusion,

obtained experimentally. We have named this the "Diffusion-Ray-Tacing" model. The implementation of our Diffusion-Ray-Tracing model takes into account the scattered light effects and explains the measured optics performance. This model showed some slight discrepancies with certain data points, but its goal was not to accurately fit all the data but to explain in a satisfactory manner the general behavior of the optics. Its value lies in indicating the causes behind the misunderstood performance, pointing out certain quality aspects of the lenses that were overlooked and contributing to the knowledge database of the JEM-EUSO collaboration. Nevertheless, certain actions are necessary to improve the Fresnel optics of any future project.

To improve the quality of lenses we have proposed two main actions in their production and postproduction. First, the fabrication parameters of the diamond turning machine can be optimized to improve the material removal process and to reduce vibrations which deteriorate the surface quality. This would require an experimental study where different samples of PMMA material have to be cut with different machining parameters. Afterwards their surface quality should be analyzed. The second proposition is the use of the magnetorheological finishing technique. This polishing technique can achieve a surface roughness below 1 nm, however it's effectiveness is limited because of the noncontinuous profile of the Fresnel lenses. Thus, it can only be applied to the wider Fresnel zones where the tool geometry allows contact with the optical surface.

Overall, we believe that Fresnel lenses are still a viable option as the main optics for a UHECR space observatory. They still require significant research and development in order to achieve the desired surface quality, and consequently, a higher optical efficiency. Once this is accomplished, the shortcomings of the lenses can be overshadowed by their benefits.

6.2 Classification of the triggered events in EUSO-SPB1

EUSO-SPB1 was successful in acquiring data during 12 observation nights, however the data taking was heavily impacted by a leak on the super pressure balloon. This resulted in extreme altitude excursions of more than 15 km which severely reduced the atmospheric volume monitored. Eventually the balloon could not be kept afloat which led to the termination of the mission. About two thirds of the data were recovered before the instrument splashed down in the pacific ocean. This data was analyzed by various collaboration members focusing on various goals.

We have presented an analysis method aimed at understanding and classifying the triggered data of EUSO-SPB1. Starting from a visual inspection phase, we discovered recurring events with repetitive characteristics that did not resemble EAS events. A method was developed to extract these events from the entirety of the flight data and create a database of events. We inspected consecutive events in this database in order to search for EAS but no candidates were found using this method. Nevertheless, this database of events has proven

useful to understand the triggered data, to describe their population statistics and properties.

About 90% of all detected events are small blobs and edge effects. They are provoked respectively by direct cosmic ray hits on the PDM and light produced inside the MAPMTs due to the ionization of heavy ions. The latter effect was identified and corrected by the manufacturer so it's very likely that it will dissapear in future experiments using improved MAPMTs. On the other hand, quite ironically low energy cosmic rays in the atmosphere represent a huge source of noise that induce triggers in the PDM and impede the capabilities of the instrument to observe UHECR. Therefore, these inevitable effects need to be mitigated through the use of another technique. This could be done through a hardware based approach, such as the use of the anticoincidence method. Alternatively this could also be achieved through a software based approach, such as the development of more advanced triggers capable of rejecting background or instrumental effects. Therefore, the EUSO-SPB1 data will be an invaluable resource towards trigger improvement and achieving the JEM-EUSO vision of eventually UHECRs from space.

We have also shown that our method is capable of detecting the pixel excesses produced simulated EAS events, however it is not able to classify them as such. A visual inspection is required to determine if the event is in effect an EAS candidate. The method was developed based on the observation of background triggered events which are not necessarily EAS. The classification of the event is done on each frame and varies depending on the zenith angle of the simulated shower and the position within the detectors FoV. Low zenith angles produce punctual events whereas larger zenith angles produce elongated ones which are classified as small blobs and tracks respectively. If the event is contained mostly in the MAPMT pixel borders then it is classified as an edge effect. Overall a similar method could be developed and adapted to the different JEM-EUSO pathfinders, this would be useful to analyze more in detail the spatial characteristics of the triggered events.

Chapter 7

Conclusion (Français)

7.1 La performance optique des démonstrateurs ballon

Avant le debut de ce travail, la performance optique d'EUSO-Balloon a été characterisé pendant deux campagnes expérimentales en 2014 et 2015. La caractérisation de l'optique a été essentiel pour atteindre les objectifs primaires de la mission et augmenter le TRL vers un observatoire spatial de RCUHE. Malgré le succès de la mission, quelques problèmes concernant la caractérisation de l'optique ont resté irrésolus. En première, partant d'une conception initiale avec deux lentilles réfractives et une lentille diffractive, cette dernière a dû être abandonné afin d'obtenir une efficacité plus élevée dans la PSF. Plus important encore, la performance mesurée de l'optique mesurée était en désaccord avec les simulations numériques et avait comportement qui n'était pas bien compris. Après la mission la performance de l'optique a resté mal compris et donc la recherche et l'explication sur les causes de ce problème est devenu un élément clé de mon travail.

Au début de mon travail notre équipe a eu l'opportunité de travailler dans la caractérisation de la performance optique d'EUSO-SPB1 et d'optimiser l'efficacité de la PSF pour le vol. Nous avons testé une configuration à deux et trois lentilles. Les mesures pris avec la configuration à trois lentilles montrent que la lentille diffractive corrige partiellement l'aberration chromatique des lentilles. Elle produit une focale primaire où toutes les longueurs d'onde convergent au même point, mais aussi une deuxième focale avec une dispersion chromatique. Cette dernière est produite par un ordre 0 de diffraction qui n'est pas complètement modulé par la lentille diffractive. Encore une fois, la configuration à deux lentilles a été choisi pour le vol parce qu'elle produisait une efficacité plus élevée dans la PSF et une meilleure efficacité de « trigger ». Les résultats de la caractérisation étaient aussi en désaccord avec les simulations numériques et en raison de contraintes de temps l'instrument a volé sans vraiment comprendre l'optique.

Afin de mieux comprendre la performance optique mesurée, nous avons effectué une analyse plus approfondie sur les lentilles de Fresnel d'EUSO-Balloon. Nous avons testé chaque lentille séparément et nous avons montré qu'elles provoquent une diffusion de lumière à cause des défauts résiduelles de fabrication. Ces défauts s'écartent du profile de surface désirée au niveau nanométrique et ont des composants périodiques d'environs 10 µm et 300 µm. En principe ils agissent comme un réseau de diffraction. Donc, nous avons des effets diffractives

inattendus dans nos lentilles réfractives.

Pour expliquer le comportement de notre optique de Fresnel nous avons développé un modèle qui combine un code de tracée de rayons pour la réfraction et réfection avec un terme semi-empirique pour la diffusion, obtenu expérimentalement. Nous l'avons appelé le modèle « Diffusion-Ray-Tracing ». L'implémentation de notre modelé Difusion-Ray-Tracing prendre en compte la lumière diffusée et explique la performance mesurée de l'optique. Ce modelé diverge avec quelques points des données, néanmoins son but n'était pas s'ajuster exactement aux données mais d'expliquer d'une manière satisfaisant le comportement global de l'optique. Sa valeur réside en indiquer les causes derrière la performance mesurée, en signaler des aspects sur la qualité des lentilles qui ont été négligés pour les deux missions et en contribuer à la basse de connaissances de la collaboration JEM-EUSO. Cependant, quelques actions seront nécessaires pour améliorer l'optique de Fresnel des projets futurs.

Pour améliorer la qualité optique des lentilles, nous proposons deux actions principales dans leur production et post-production. En première, les paramètres de fabrication du tournage au diamant peuvent être optimisés pour améliorer le procès d'enlèvement de matière et pour réduire les vibrations qui dégradent la qualité de surface. Cela requerra une étude expérimentale avec des divers échantillons de PMMA qui devront être fraises avec des paramètres de tournage divers. Puis la qualité de surface devra être mesurée. La seconde proposition est l'utilisation de la technique de polissage magnétorhéologique. Cette technique peut atteindre une rugosité de surface de moins de 1 nm, cependant son efficacité est limitée à cause du profil discontinu des lentilles de Fresnel. Donc, elle ne peut être appliqué que dans les zones de Fresnel plus larges où la géométrie de l'outil de polissage permet le contact avec la surface optique.

Globalement, nous croyons que les lentilles de Fresnel restent toujours une option viable en tant que l'optique principale pour un observatoire spatial de RCUHE. Elles ont toujours besoin d'une recherche et développent significatif afin d'obtenir la qualité de surface désirée et, par conséquent, une efficacité optique plus élevée. Une fois cela accompli, les faiblesses des lentilles de Fresnel peuvent être éclipsés par ses bénéfices.

7.2 Classification des événements enregistrés dans EUSO-SPB1

Pendant 12 nuits d'observation EUSO-SPB1 a acquis des données avec succès, cependant cette acquisition a été fortement affecté par une fuite dans le ballon super pressurisé. Cela a causé des excursions d'altitude de plus de 15 km qui ont réduit le volume d'atmosphère surveillé. Éventuellement c'était plus possible de maintenir le vol du ballon et la mission a dû être terminé. Environ deux tiers des donnés ont été télécharges avant l'amerrissage de l'instrument dans l'océan pacifique. Les données ont été analyses par plusieurs membres de la collaboration avec des objectifs variés.

Nous avons présenté une méthode d'analyse visant à comprendre et classifier les évènements enregistrés par l'algorithme de trigger d'EUSO-SPB1. Partant d'une phase d'inspection visuelle, nous avons découvert des évènements avec des caractéristiques répétitives qui ne ressemblaient pas des gerbes atmosphériques. Une méthode a été développé pour extraire ces évènements de l'ensemble des données de vol et pour créer une basse de donnés de ces évènements. Nous avons inspecté tous les évènements consécutifs afin de trouver des gerbes atmosphériques mais pas de candidates ont été trouvées avec cette méthode. Néanmoins, cette base de données s'est révélée utile pour comprendre les données enregistres, pour décrire sa population statistique et ses propriétés.

Environ 90% des évènements détectés sont des « small blobs » et « edge effects ». Ils sont provoqués respectivement par l'interaction directe de rayons cosmiques avec le module photo-détecteur et par une lumière produite à l'intérieur des tubes photomultiplicateurs dû à l'ionisation des ions lourds. Ce dernier effet a été identifié et corrigé par le fabricant, par conséquent c'est très probable qu'il n'apparaitra plus dans les expériences futures. D'autre part, ironiquement les rayons cosmiques de basse énergie induisent le déclenchement du trigger et gênent la capabilité d'observer des RCUHE par l'instrument. Donc, ces effets inévitables doivent être réduits par l'utilisation d'une autre technique. Cela pourrait être fait au niveau du hardware, tel que la technique d'anti-coïncidence. Autrement, ça pourrait être fait au niveau du logiciel, par exemple avec le développement des algorithmes de trigger plus avancées et capables de rejeter des effets de bruit de fond ou instrumentaux. De ce fait, l'ensemble de données d'EUSO-SPB1 sont une ressource indispensable vers l'améliorèrent des triggers et l'accomplissement de la vision de JEM-EUSO.

Nous avons aussi montré que notre méthode est capable de détecter les signales produits par les gerbes atmosphériques simulées, cependant elle n'est pas capable de les classifier en tante que telles. Une inspection visuelle est toujours necessaire pour determiner si l'evenement est une candidate à gerbe atmospherique. La méthode a été développé en base à l'observation des évènements enregistrés qui ne correspond pas forcement aux gerbes atmosphériques. La classification des evenements est faite par GTU et diffère selon l'angle de zénith et la position de la gerbe dans le champ de vue du détecteur. Les angles de zénith bases produisent des évènements ponctuels, tandis que les angles plus larges produisent des évènements plus allongés. Ces évènements sont respectivement classifiés comme des « blobs » et « tracks ». D'autre part, si l'évènement est situé dans les pixels du bord des tubes photomultiplicateurs alors il est classifié comme « edge effect ». Globalement, une méthode similaire peut être développé et adapté aux différents démonstrateurs de JEM-EUSO, cela pourrait être outil pour analyser plus en détail les caractéristiques des évènements enregistrés par le trigger.

Bibliography

[1] Michael Walter. "From the Discovery of Radioactivity to the First Accelerator Experiments". In: *From Ultra Rays to Astroparticles: A Historical Introduction to Astroparticle Physics*. Ed. by Brigitte Falkenburg and Wolfgang Rhode. Dordrecht: Springer Netherlands, 2012, pp. 17–47. DOI: 10.1007/978-94-007-5422-5_2.

[2] Victor Hess. "On the Observations of the Penetrating Radiation during Seven Balloon Flights". In: *arXiv:1808.02927 [astro-ph, physics:physics]* (July 23, 2018). arXiv: 1808.02927.

[3] W. Bothe. "Zur Vereinfachung von Koinzidenzzählungen". In: *Zeitschrift für Physik* 59.1 (Jan. 1, 1930), pp. 1–5. DOI: 10.1007/BF01337830.

[4] H. Geiger and W. Müller. "Elektronenzählrohr zur Messung schwächster Aktivitäten". In: *Naturwissenschaften* 16.31 (Aug. 1, 1928), pp. 617–618. DOI: 10.1007/BF01494093.

[5] W. Bothe and W. Kolhörster. "Das Wesen der Höhenstrahlung". In: *Zeitschrift für Physik* 56.11 (Nov. 1, 1929), pp. 751–777. DOI: 10.1007/BF01340137.

[6] Arthur H. Compton. "A Geographic Study of Cosmic Rays". In: *Physical Review* 43.6 (Mar. 15, 1933), pp. 387–403. DOI: 10.1103/PhysRev.43.387.

[7] Charles Thomson Rees Wilson. "On a method of making visible the paths of ionising particles through a gas". In: *Proceedings of the Royal Society of London. Series A, Containing Papers of a Mathematical and Physical Character* 85.578 (June 9, 1911), pp. 285–288. DOI: 10.1098/rspa.1911.0041.

[8] Bruno Rossi. "Method of Registering Multiple Simultaneous Impulses of Several Geiger's Counters". In: *Nature* 125.3156 (Apr. 1930), pp. 636–636. DOI: 10.1038/125636a0.

[9] P. M. S. Blackett and G. Occhialini. "Photography of Penetrating Corpuscular Radiation". In: *Nature* 130.3279 (Sept. 1932), pp. 363–363. DOI: 10.1038/130363a0.

[10] Bruno Rossi. "Über die Eigenschaften der durchdringenden Korpuskularstrahlung im Meeresniveau". In: *Zeitschrift für Physik* 82.3 (Mar. 1, 1933), pp. 151–178. DOI: 10.1007/BF01341486.

[11] Erich Regener and Georg Pfotzer. "Vertical Intensity of Cosmic Rays by Threefold Coincidences in the Stratosphere". In: *Nature* 136.3444 (Nov. 1935), pp. 718–719. DOI: 10.1038/136718a0.

[12] Karl-Heinz Kampert and Alan A. Watson. "Development of Ultra High-Energy Cosmic Ray Research". In: *From Ultra Rays to Astroparticles: A Historical Introduction to Astroparticle Physics*. Ed. by Brigitte Falkenburg and Wolfgang Rhode. Dordrecht: Springer Netherlands, 2012, pp. 103–141. DOI: 10.1007/978-94-007-5422-5_5.

[13] P. Bassi, G. Clark, and B. Rossi. "Distribution of Arrival Times of Air Shower Particles". In: *Physical Review* 92.2 (Oct. 15, 1953), pp. 441–451. DOI: 10.1103/PhysRev.92.441.

[14] G. Clark et al. “An Experiment on Air Showers Produced by High-Energy Cosmic Rays”. In: *Nature* 180.4582 (Aug. 1957), pp. 353–356. DOI: 10.1038/180353a0.

[15] J. Linsley. “The cosmic ray spectrum above 10(19) EV at Volcano Ranch and Haverah Park”. In: *19th International Cosmic Ray Conference (ICRC19), Volume 9* 9 (Aug. 1985), p. 475.

[16] John Linsley. “Evidence for a Primary Cosmic-Ray Particle with Energy 10^{20} eV”. In: *Physical Review Letters* 10.4 (Feb. 15, 1963), pp. 146–148. DOI: 10.1103/PhysRevLett.10.146.

[17] Particle Data Group, M. Tanabashi, et al. “Review of Particle Physics”. In: *Physical Review D* 98.3 (Aug. 17, 2018), p. 030001. DOI: 10.1103/PhysRevD.98.030001.

[18] Thomas K. Gaisser, Ralph Engel, and Elisa Resconi. *Cosmic Rays and Particle Physics by Thomas K. Gaisser*. June 2016. DOI: 10.1017/CBO9781139192194.

[19] A. M. Hillas. “The Origin of Ultra-High-Energy Cosmic Rays”. In: *Annual Review of Astronomy and Astrophysics* 22 (1984), pp. 425–444. DOI: 10.1146/annurev.aa.22.090184.002233.

[20] Kumiko Kotera and Angela V. Olinto. “The Astrophysics of Ultrahigh Energy Cosmic Rays”. In: *Annual Review of Astronomy and Astrophysics* 49.1 (Sept. 22, 2011), pp. 119–153. DOI: 10.1146/annurev-astro-081710-102620. arXiv: 1101.4256.

[21] Kenneth Greisen. “End to the Cosmic-Ray Spectrum?” In: *Physical Review Letters* 16.17 (Apr. 25, 1966), pp. 748–750. DOI: 10.1103/PhysRevLett.16.748.

[22] G. T. Zatsepin and V. A. Kuz’min. “Upper Limit of the Spectrum of Cosmic Rays”. In: *Soviet Journal of Experimental and Theoretical Physics Letters* 4 (Aug. 1, 1966), p. 78.

[23] N. Globus, D. Allard, and E. Parizot. “Propagation of high-energy cosmic rays in extragalactic turbulent magnetic fields: resulting energy spectrum and composition”. In: *Astronomy and Astrophysics* 479 (Feb. 2008), p. 97. DOI: 10.1051/0004-6361:20078653.

[24] J. Matthews. “A Heitler model of extensive air showers”. In: *Astroparticle Physics* 22.5 (Jan. 1, 2005), pp. 387–397. DOI: 10.1016/j.astropartphys.2004.09.003.

[25] AMS Collaboration. *AMS-02 | The Alpha Magnetic Spectrometer Experiment*. AMS-02 | The Alpha Magnetic Spectrometer Experiment. URL: https://ams02.space/ (visited on 11/08/2019).

[26] T. Abu-Zayyad et al. “The surface detector array of the Telescope Array experiment”. In: *Nuclear Instruments and Methods in Physics Research Section A: Accelerators, Spectrometers, Detectors and Associated Equipment* 689 (Oct. 2012), pp. 87–97. DOI: 10.1016/j.nima.2012.05.079. arXiv: 1201.4964.

[27] J. Abraham et al. “Properties and performance of the prototype instrument for the Pierre Auger Observatory”. In: *Nuclear Instruments and Methods in Physics Research Section A: Accelerators, Spectrometers, Detectors and Associated Equipment* 523.1 (May 1, 2004), pp. 50–95. DOI: 10.1016/j.nima.2003.12.012.

[28] Peter K.F. Grieder. “Lateral Structure of Showers and Energy Flow”. In: *Extensive Air Showers: High Energy Phenomena and Astrophysical Aspects A Tutorial, Reference Manual and Data Book*. Ed. by Peter K.F. Grieder. Berlin, Heidelberg: Springer, 2010, pp. 359–397. DOI: 10.1007/978-3-540-76941-5_8.

[29] T Antoni et al. “The cosmic-ray experiment KASCADE”. In: *Nuclear Instruments and Methods in Physics Research Section A: Accelerators, Spectrometers, Detectors and Associated Equipment* 513.3 (Nov. 11, 2003), pp. 490–510. DOI: 10.1016/S0168-9002(03)02076-X.

[30] M. Ave et al. “Spectrally resolved pressure dependence measurements of air fluorescence emission with AIRFLY”. In: *Nuclear Instruments and Methods in Physics Research Section A: Accelerators, Spectrometers, Detectors and Associated Equipment*. Proceedings of the 5th Fluorescence Workshop 597.1 (Nov. 21, 2008), pp. 41–45. DOI: 10.1016/j.nima.2008.08.052.

[31] Peter K.F. Grieder. “Atmospheric Fluorescence”. In: *Extensive Air Showers: High Energy Phenomena and Astrophysical Aspects A Tutorial, Reference Manual and Data Book*. Ed. by Peter K.F. Grieder. Berlin, Heidelberg: Springer, 2010, pp. 879–912. DOI: 10.1007/978-3-540-76941-5_17.

[32] Alan Newton Bunner. “Cosmic Ray Detection by Atmospheric Fluorescence.” PhD thesis. Cornell University, 1967.

[33] R. M. Baltrusaitis et al. “The Utah Fly’s Eye detector”. In: *Nuclear Instruments and Methods in Physics Research Section A: Accelerators, Spectrometers, Detectors and Associated Equipment* 240.2 (Oct. 15, 1985), pp. 410–428. DOI: 10.1016/0168-9002(85)90658-8.

[34] Antje Kohnle. “HESS - The High Energy Stereoscopic System”. In: *26th International Cosmic Ray Conference (ICRC26), Volume 5* 5 (1999), p. 239.

[35] Peter K.F. Grieder. “Shower Detection Methods and Basic Event Reconstruction”. In: *Extensive Air Showers: High Energy Phenomena and Astrophysical Aspects A Tutorial, Reference Manual and Data Book*. Ed. by Peter K.F. Grieder. Berlin, Heidelberg: Springer, 2010, pp. 33–76. DOI: 10.1007/978-3-540-76941-5_2.

[36] J. V. JELLEY et al. “Radio Pulses from Extensive Cosmic-Ray Air Showers”. In: *Nature* 205.4969 (Jan. 1, 1965), pp. 327–328. DOI: 10.1038/205327a0.

[37] M. P. Van Haarlem et al. “LOFAR: The LOw-Frequency ARray”. In: *Astronomy & Astrophysics* 556 (Aug. 2013), A2. DOI: 10.1051/0004-6361/201220873. arXiv: 1305.3550.

[38] Matthew Joseph Mottram. *A Search for Ultra-High Energy Neutrinos and Cosmic-Rays with ANITA-2*. Springer Theses. Berlin Heidelberg: Springer-Verlag, 2012. DOI: 10.1007/978-3-642-30032-5.

[39] The Pierre Auger Collaboration, A. Aab, et al. "The Pierre Auger Observatory Upgrade - Preliminary Design Report". In: *arXiv:1604.03637 [astro-ph]* (Apr. 12, 2016). arXiv: 1604.03637.

[40] A. Aab et al. "Observation of a large-scale anisotropy in the arrival directions of cosmic rays above 8×10^{18} eV". In: *Science* 357.6357 (Sept. 22, 2017), pp. 1266–1270. DOI: 10.1126/science.aan4338.

[41] H. Tokuno et al. "New air fluorescence detectors employed in the Telescope Array experiment". In: *Nuclear Instruments and Methods in Physics Research Section A: Accelerators, Spectrometers, Detectors and Associated Equipment* 676 (June 1, 2012), pp. 54–65. DOI: 10.1016/j.nima.2012.02.044.

[42] R. U. Abbasi et al. "The Cosmic Ray Energy Spectrum between 2 PeV and 2 EeV Observed with the TALE Detector in Monocular Mode". In: *The Astrophysical Journal* 865.1 (Sept. 2018), p. 74. DOI: 10.3847/1538-4357/aada05.

[43] R. Benson and J. Linsley. "Satellite Observation of Cosmic-Ray Air Showers". In: *International Cosmic Ray Conference* 8 (1981), p. 145.

[44] Y. Takahashi. "Maximum-energy Auger Air Shower Satellite (MASS) for Observing Cosmic Rays in the Energy Region 10^{19-22} eV". In: *International Cosmic Ray Conference* 3 (1995), p. 595.

[45] The JEM-EUSO Collaboration, J. H. Adams, et al. "The JEM-EUSO mission: An introduction". In: *Experimental Astronomy* 40.1 (Nov. 2015), pp. 3–17. DOI: 10.1007/s10686-015-9482-x.

[46] The JEM-EUSO Collaboration, J. H. Adams, et al. "The JEM-EUSO instrument". In: *Experimental Astronomy* 40.1 (Nov. 1, 2015), pp. 19–44. DOI: 10.1007/s10686-014-9418-x.

[47] "An evaluation of the exposure in nadir observation of the JEM-EUSO mission". In: *Astroparticle Physics* 44 (Apr. 2013), pp. 76–90. DOI: 10.1016/j.astropartphys.2013.01.008. arXiv: 1305.2478.

[48] The JEM-EUSO Collaboration, J. H. Adams, et al. "The atmospheric monitoring system of the JEM-EUSO instrument". In: *Experimental Astronomy* 40.1 (Nov. 1, 2015), pp. 45–60. DOI: 10.1007/s10686-014-9378-1.

[49] Alessandro Zuccaro Marchi, Yoshiyuki Takizawa, and Yoshiyuki Takahashi. "The JEM-EUSO optics design". In: *International Cosmic Ray Conference* 3 (2011), p. 180. DOI: 10.7529/ICRC2011/V03/0852.

[50] M. Ambrosio et al. "The camera of the Pierre Auger Observatory Fluorescence Detector". In: *Nuclear Instruments and Methods in Physics Research Section A: Accelerators, Spectrometers, Detectors and Associated Equipment* 478.1 (2002), pp. 125–129. DOI: https://doi.org/10.1016/S0168-9002(01)01731-4.

[51] Zbigniew Plebaniak et al. “HVPS system for EUSO detectors”. In: *Proceedings of 35th International Cosmic Ray Conference - PoS(ICRC2017)*. Vol. 301. SISSA Medialab, Aug. 3, 2018, p. 378. DOI: 10.22323/1.301.0378.

[52] Salleh Ahmad et al. “SPACIROC: A Front-End Readout ASIC for JEM-EUSO Cosmic Ray Observatory”. In: *Physics Procedia*. Proceedings of the 2nd International Conference on Technology and Instrumentation in Particle Physics (TIPP 2011) 37 (Jan. 1, 2012), pp. 1600–1607. DOI: 10.1016/j.phpro.2012.02.482.

[53] S. Ahmad et al. “SPACIROC2: a front-end readout ASIC for the JEM-EUSO observatory”. In: *Journal of Instrumentation* 8.1 (Jan. 2013), pp. C01006–C01006. DOI: 10.1088/1748-0221/8/01/C01006.

[54] S. Blin et al. “SPACIROC3: 100 MHz photon counting ASIC for EUSO-SPB”. In: *Nuclear Instruments and Methods in Physics Research Section A: Accelerators, Spectrometers, Detectors and Associated Equipment* 912 (Dec. 2018), pp. 363–367. DOI: 10.1016/j.nima.2017.12.060.

[55] A. Jung. “Design and implementation of the Photo-Detector Module electronics for the EUSO-Balloon, prototype of the JEM-EUSO telescope”. In: *Journal of Instrumentation* 10.8 (Aug. 2015), pp. C08014–C08014. DOI: 10.1088/1748-0221/10/08/C08014.

[56] Giuseppe Osteria and Valentina Scotti. “The JEM-EUSO time synchronization system and EUSO BALLOON Data Processor”. In: *Journal of Physics: Conference Series* 409 (Feb. 2013), p. 012106. DOI: 10.1088/1742-6596/409/1/012106.

[57] Jörg Bayer et al. “The Cluster Control Board of the JEM-EUSO mission”. In: 3 (Aug. 11, 2011), p. 172. DOI: 10.7529/ICRC2011/V03/0836.

[58] M. Bertaina et al. “The First Level Trigger of JEM-EUSO: Concept and tests”. In: *Nuclear Instruments and Methods in Physics Research Section A: Accelerators, Spectrometers, Detectors and Associated Equipment*. Frontier Detectors for Frontier Physics: Proceedings of the 13th Pisa Meeting on Advanced Detectors 824 (July 11, 2016), pp. 253–255. DOI: 10.1016/j.nima.2015.10.044.

[59] The JEM-EUSO Collaboration, G. Abdellaoui, et al. “Cosmic ray oriented performance studies for the JEM-EUSO first level trigger”. In: *Nuclear Instruments and Methods in Physics Research Section A: Accelerators, Spectrometers, Detectors and Associated Equipment* 866 (Sept. 11, 2017), pp. 150–163. DOI: 10.1016/j.nima.2017.05.043.

[60] J. H. Adams et al. “The EUSO-Balloon pathfinder”. In: *Experimental Astronomy* 40.1 (Nov. 1, 2015), pp. 281–299. DOI: 10.1007/s10686-015-9467-9.

[61] G. Abdellaoui et al. “Ultra-violet imaging of the night-time earth by EUSO-Balloon towards space-based ultra-high energy cosmic ray observations”. In: *Astroparticle Physics* 111 (Sept. 1, 2019), pp. 54–71. DOI: 10.1016/j.astropartphys.2018.10.008.

[62] G. Abdellaoui et al. “First observations of speed of light tracks by a fluorescence detector looking down on the atmosphere”. In: *Journal of Instrumentation* 13.5 (May 2018), P05023–P05023. DOI: 10.1088/1748-0221/13/05/P05023.

[63] Gregorio Suino et al. “Tests of JEM–EUSO 1st level trigger using EUSO–Balloon data”. In: *Proceedings of The 34th International Cosmic Ray Conference - PoS(ICRC2015)*. The 34th International Cosmic Ray Conference. Vol. 236. SISSA Medialab, Aug. 18, 2016, p. 645. DOI: 10.22323/1.236.0645.

[64] Mario E. Bertaina et al. “The trigger logic of EUSO-SPB and its performance”. In: *Proceedings of 35th International Cosmic Ray Conference - PoS(ICRC2017)*. 35th International Cosmic Ray Conference. Vol. 301. SISSA Medialab, Aug. 3, 2018, p. 443. DOI: 10.22323/1.301.0443.

[65] M. Battisti et al. “Performance results of the trigger logic implemented in EUSO-SPB”. In: *Nuclear Instruments and Methods in Physics Research Section A: Accelerators, Spectrometers, Detectors and Associated Equipment*. Frontier Detectors for Frontier Physics: 14th Pisa Meeting on Advanced Detectors 936 (Aug. 21, 2019), pp. 349–350. DOI: 10.1016/j.nima.2018.11.002.

[66] Leo Allen et al. “UCIRC: Infrared Cloud Monitor for EUSO-SPB”. In: *Proceedings of 35th International Cosmic Ray Conference - PoS(ICRC2017)*. 35th International Cosmic Ray Conference. Vol. 301. SISSA Medialab, Aug. 3, 2018, p. 436. DOI: 10.22323/1.301.0436.

[67] Anna Anzalone et al. “Methods to Retrieve the Cloud-Top Height in the Frame of the JEM-EUSO Mission”. In: *IEEE Transactions on Geoscience and Remote Sensing* 57.1 (Jan. 2019), pp. 304–318. DOI: 10.1109/TGRS.2018.2854296.

[68] Andreas Haungs et al. “SiECA: Silicon Photomultiplier Prototype for Flight with EUSO-SPB”. In: *Proceedings of 35th International Cosmic Ray Conference - PoS(ICRC2017)*. 35th International Cosmic Ray Conference. Vol. 301. SISSA Medialab, Aug. 3, 2018, p. 442. DOI: 10.22323/1.301.0442.

[69] A. Aab et al. “Muon counting using silicon photomultipliers in the AMIGA detector of the Pierre Auger observatory”. In: *Journal of Instrumentation* 12.3 (Mar. 3, 2017), P03002. DOI: 10.1088/1748-0221/12/03/P03002.

[70] Tim Niggemann et al. “Status of the Silicon Photomultiplier Telescope FAMOUS for the Fluorescence Detection of UHECRs”. In: *arXiv:1502.00792 [astro-ph]* (Feb. 3, 2015). arXiv: 1502.00792.

[71] The IceCube-Gen2 Collaboration et al. “The IceTop Scintillator Upgrade”. In: *Proceedings of 35th International Cosmic Ray Conference - PoS(ICRC2017)*. Vol. 301. SISSA Medialab, Aug. 3, 2018, p. 401. DOI: 10.22323/1.301.0401.

[72] G. Abdellaoui et al. “EUSO-TA First results from a ground-based EUSO telescope”. In: *Astroparticle Physics* 102 (Nov. 1, 2018), pp. 98–111. DOI: 10.1016/j.astropartphys.2018.05.007.

[73] Francesca Capel et al. “Mini-EUSO: A high resolution detector for the study of terrestrial and cosmic UV emission from the International Space Station”. In: *Advances in Space Research*. Origins of Cosmic Rays 62.10 (Nov. 15, 2018), pp. 2954–2965. DOI: 10.1016/j.asr.2017.08.030.

[74] V. Scotti and G. Osteria. "The EUSO-SPB2 mission". In: *Nuclear Instruments and Methods in Physics Research Section A: Accelerators, Spectrometers, Detectors and Associated Equipment* (May 8, 2019). DOI: 10.1016/j.nima.2019.05.005.

[75] A. V. Olinto et al. "POEMMA (Probe of Extreme Multi-Messenger Astrophysics) design". In: *arXiv:1907.06217 [astro-ph, physics:hep-ex]* (July 14, 2019). arXiv: 1907.06217.

[76] B. A. Khrenov et al. "First results from the TUS orbital detector in the extensive air shower mode". In: *Journal of Cosmology and Astroparticle Physics* 2017.9 (Sept. 6, 2017), p. 006. DOI: 10.1088/1475-7516/2017/09/006.

[77] Pavel Klimov, Marco Casolino, and on behalf of the JEM-EUSO Collaboration. "Status of the KLYPVE-EUSO detector for EECR study on board the ISS". In: *Proceedings of 35th International Cosmic Ray Conference — PoS(ICRC2017)*. 35th International Cosmic Ray Conference. Vol. 301. SISSA Medialab, Aug. 3, 2018, p. 412. DOI: 10.22323/1.301.0412.

[78] G. K. Garipov et al. "An extensive-air-shower-like event registered with the TUS orbital detector". In: (July 13, 2019). arXiv: 1907.06028.

[79] Fumiyoshi Kajino. "K-EUSO: An improved optical system for KLYPVE ultra-high energy cosmic ray space telescope". In: *Proceedings of The 34th International Cosmic Ray Conference - PoS(ICRC2015)*. The 34th International Cosmic Ray Conference. Vol. 236. SISSA Medialab, Aug. 18, 2016, p. 634. DOI: 10.22323/1.236.0634.

[80] Marco Casolino et al. "KLYPVE-EUSO: Science and UHECR observational capabilities". In: *Proceedings of 35th International Cosmic Ray Conference - PoS(ICRC2017)*. 35th International Cosmic Ray Conference. Vol. 301. SISSA Medialab, Aug. 3, 2018, p. 368. DOI: 10.22323/1.301.0368.

[81] Camille Catalano. "Premières lumières du tèlescope EUSO-Ballon". PhD thesis. Université de Toulouse, Université Toulouse III - Paul Sabatier, 2015.

[82] D. Appleton and Company. *Appleton's Dictionary of Machines, Mechanics, Engine-work, and Engineering*. Appleton's Dictionary of Machines, Mechanics, Engine-work, and Engineering v. 1. D. Appleton, 1873.

[83] Yoshiyuki Takizawa, Alessandro Zuccaro Marchi, and Toshikazu Ebisuzaki. "The TA-EUSO and EUSO-Balloon Optics Designs". In: vol. 33. 2013, p. 627.

[84] Yousuke Hachisu et al. "Manufacturing of the TA-EUSO and the EUSO-Balloon lenses". In: vol. 33. 2013, p. 2294.

[85] Johannes Eser. "EUSO-SPB1 project and laser test beams for space-based optical cosmic ray detectors, The". PhD thesis. Colorado School of Mines. Arthur Lakes Library, 2018.

[86] David M. Aikens, Jessica E. DeGroote, and Richard N. Youngworth. “Specification and Control of Mid-Spatial Frequency Wavefront Errors in Optical Systems”. In: *Frontiers in Optics 2008/Laser Science XXIV/Plasmonics and Metamaterials/Optical Fabrication and Testing (2008), paper OTuA1*. Optical Fabrication and Testing. Optical Society of America, Oct. 21, 2008, OTuA1. DOI: 10.1364/OFT.2008.OTuA1.

[87] James E. Harvey and Anita Kotha Thompson. “Scattering effects from residual optical fabrication errors”. In: *International Conference on Optical Fabrication and Testing*. International Conference on Optical Fabrication and Testing. Vol. 2576. International Society for Optics and Photonics, Aug. 2, 1995, pp. 155–174. DOI: 10.1117/12.215588.

[88] *Welcome to pySerial's documentation - pySerial 3.0 documentation*. URL: https://pythonhosted.org/pyserial/# (visited on 11/13/2019).

[89] Feifei Jiao and Kai Cheng. “An experimental investigation on micro-milling of polymethyl methacrylate components with nanometric surface roughness:” in: *Proceedings of the Institution of Mechanical Engineers, Part B: Journal of Engineering Manufacture* (Nov. 1, 2013). DOI: 10.1177/0954405413507251.

[90] Daniel C. Harris. “History of magnetorheological finishing”. In: *Window and Dome Technologies and Materials XII*. Window and Dome Technologies and Materials XII. Vol. 8016. International Society for Optics and Photonics, May 20, 2011, 80160N. DOI: 10.1117/12.882557.

[91] QED Technologies Inc. *MRF: How it works*. How does MRF work? 2020. URL: https://qedmrf.com/en/mrfpolishing/mrf-technology/how-it-works (visited on 02/12/2020).

[92] Johannes Eser et al. “Preflight calibration and testing of EUSO-SPB in the lab and the desert”. In: *Proceedings of 35th International Cosmic Ray Conference - PoS(ICRC2017)*. 35th International Cosmic Ray Conference. Vol. 301. SISSA Medialab, Aug. 3, 2018, p. 1097. DOI: 10.22323/1.301.0457.

[93] Y. Takahashi et al. “Central Laser Facility Analysis at The Telescope Array Experiment”. In: *AIP Conference Proceedings* 1367.1 (Sept. 22, 2011), pp. 157–160. DOI: 10.1063/1.3628734.

[94] Lawrence Wiencke, Angela Olinto, and on behalf of the JEM-EUSO Collaboration. “EUSO-SPB1 Mission and Science”. In: *Proceedings of 35th International Cosmic Ray Conference - PoS(ICRC2017)*. Vol. 301. SISSA Medialab, Aug. 3, 2018, p. 1097. DOI: 10.22323/1.301.1097.

[95] Carolyn A. Kierans et al. “The 2016 Super Pressure Balloon flight of the Compton Spectrometer and Imager”. In: *arXiv:1701.05558 [astro-ph]* (Jan. 19, 2017). arXiv: 1701.05558.

[96] National Aeronautics Space Administration. *NASA Southern Hemisphere Ultra Long Duration Ballooning Operations Expansion IEE/EA*. June 2014, p. 170.

[97] Jeremy Eggers. *Alien crop circle? No, that's just NASA's newest balloon launch pad - Super Pressure Balloon.* Super Pressure Balloon blog. Mar. 18, 2017. URL: https://blogs.nasa.gov/superpressureballoon/2017/03/18/alien-crop-circle-no-thats-just-nasas-newest-balloon-launch-pad/ (visited on 09/26/2019).

[98] Michelle Johnson. *NASA - Columbia Scientific Balloon Facility.* Oct. 19, 2018. URL: https://www.csbf.nasa.gov/mission.html (visited on 09/25/2019).

[99] Henry M Cathey and David L Pierce. "Development of the NASA Ultra-Long Duration Balloon". In: NASA Science Technology Conference 2017. June 2017, p. 14.

[100] Rachel Gregg. *EUSO-SPB Blog.* EUSO-SPB Blog. Mar. 5, 2017. URL: http://astroserve.mines.edu/euso_spb/Blog.html (visited on 09/24/2019).

[101] I. Antcheva et al. "ROOT a A C++ framework for petabyte data storage, statistical analysis and visualization". In: *Computer Physics Communications* 182.6 (2011), pp. 1384–1385. DOI: https://doi.org/10.1016/j.cpc.2011.02.008.

[102] Don Groom. "Cosmic rays and other nonsense in astronomical CCD imagers". In: *Experimental Astronomy* 14.1 (Aug. 1, 2002), pp. 45–55. DOI: 10.1023/A:1026196806990.

[103] N. Otsu. "A Threshold Selection Method from Gray-Level Histograms". In: *IEEE Transactions on Systems, Man, and Cybernetics* 9.1 (Jan. 1979), pp. 62–66. DOI: 10.1109/TSMC.1979.4310076.

[104] P. A. Klimov et al. "Preliminary results from the TUS ultra-high energy cosmic ray orbital telescope: Registration of low-energy particles passing through the photodetector". In: *Bulletin of the Russian Academy of Sciences: Physics* 81.4 (Apr. 2017), pp. 407–409. DOI: 10.3103/S1062873817040256.

[105] C. Berat et al. "ESAF: Full Simulation of Space-Based Extensive Air Showers Detectors". In: *Astroparticle Physics* 33.4 (May 2010), pp. 221–247. DOI: 10.1016/j.astropartphys.2010.02.005. arXiv: 0907.5275.

[106] Thomas C. Paul. "A new design for simulation and reconstruction software for the JEM-EUSO mission". In: *Proceedings of The 34th International Cosmic Ray Conference - PoS(ICRC2015).* The 34th International Cosmic Ray Conference. Vol. 236. SISSA Medialab, Aug. 18, 2016, p. 578. DOI: 10.22323/1.236.0578.

Résumé — Les Rayons Cosmiques d'Ultra Haute Énergie (RCUHE) sont des particules chargées venant de l'espace avec des énergies $>10^{18}$ eV jusqu'à une énergie mesurée de 3×10^{20} eV. Ils sont les messagers cosmiques les plus énergétiques, cependant leur origine et les mécanismes permettant leur accélération restent inconnus. Leur observation est difficile à cause de leur très faible flux (1 particule par stéradian par km^2 par siècle) et nécessite des techniques de détection indirectes, utilisant l'atmosphère comme un calorimètre. Le projet JEM-EUSO a pour but le développement d'un télescope spatial capable d'observer les gerbes atmosphériques produites par les RCUHE par le biais de leur émission de fluorescence en UV (300 - 400 nm). Pour atteindre ces objectifs, deux projets ballons démonstrateurs ont été développés afin de tester la technologie et les méthodes requises: EUSO-Balloon et EUSO-SPB1, qui ont volé en 2014 et 2017 respectivement.

Une technologie clé de ces démonstrateurs est leur système d'optique réfractive composé de deux larges lentilles de Fresnel (≈ 1 m^2). EUSO-Balloon a volé pendant une nuit et son système optique a contribué à l'observation de traces de laser et la mesure du bruit de fond UV. Néanmoins, la performance des optiques est restée mal comprise, i.e. l'efficacité et sa fonction d'étalement du point (PSF). Ce travail explique la méthode utilisée pour caractériser la performance de l'optique et l'efficacité globale des lentilles de Fresnel. La performance mesurée peut être comprise par la combinaison d'un modèle de diffusion semi-empirique avec une simulation classique de tracé de rayon.

EUSO-SPB1 a collecté des données pendant 12 nuits. On présente l'analyse des événements enregistrés suite au déclenchement de l'algorithme de "trigger". On classifie ces événements en différentes catégories et on discute leurs caractéristiques. On montre que la majorité des événements enregistrés sont des rayons cosmiques qui interagissent directement avec le détecteur ainsi que des défauts instrumentaux sur les tubes photomultiplicateurs du détecteur. Aucune gerbe atmosphérique n'a été trouvé dans cette analyse.

Mots clés : Rayons Cosmiques D'Ultra Haute Energie, Gerbes Atmospheriques, Optique de Fresnel, Analyse des données

Institut de Recherche en Astrophysique et Planetologie, 9 Avenue du Colonel Roche
31400 Toulouse, France